

Open Research Online

The Open University's repository of research publications
and other research outputs

Scientific rationale for Uranus and Neptune *in situ* explorations

Journal Item

How to cite:

Mousis, O.; Atkinson, D.H.; Cavalié, T.; Fletcher, L.N.; Amato, M.J.; Aslam, S.; Ferri, F.; Renard, J.-B.; Spilker, T.; Venkatapathy, E.; Wurz, P.; Aplin, K.; Coustenis, A.; Deleuil, M.; Dobrijevic, M.; Fouchet, T.; Guillot, T.; Hartogh, P.; Hewagama, T.; Hofstadter, M.D.; Hue, V.; Hueso, R.; Lebreton, J.-P.; Lellouch, E.; Moses, J.; Orton, G.S.; Pearl, J.C.; Sánchez-Lavega, A.; Simon, A.; Venot, O.; Waite, J.H.; Achterberg, R.K.; Atreya, S.; Billebaud, F.; Blanc, M.; Borget, F.; Brugger, B.; Charnoz, S.; Chiavassa, T.; Cottini, V.; d'Hendecourt, L.; Danger, G.; Encrenaz, T.; Gorius, N.J.P.; Jorda, L.; Marty, B.; Moreno, R.; Morse, A.; Nixon, C.; Reh, K.; Ronnet, T.; Schmider, F.-X.; Sheridan, S.; Sotin, C.; Vernazza, P. and Villanueva, G.L. (2018). Scientific rationale for Uranus and Neptune *in situ* explorations. *Planetary and Space Science*, 155 pp. 12–40.

For guidance on citations see [FAQs](#).

© 2017 Elsevier Ltd.

Version: Accepted Manuscript

Link(s) to article on publisher's website:

<http://dx.doi.org/doi:10.1016/j.pss.2017.10.005>

Copyright and Moral Rights for the articles on this site are retained by the individual authors and/or other copyright owners. For more information on Open Research Online's data [policy](#) on reuse of materials please consult the policies page.

Accepted Manuscript



Scientific rationale for Uranus and Neptune *in situ* explorations

O. Mouis, D.H. Atkinson, T. Cavalié, L.N. Fletcher, M.J. Amato, S. Aslam, F. Ferri, J.-B. Renard, T. Spilker, E. Venkatapathy, P. Wurz, K. Aplin, A. Coustenis, M. Deleuil, M. Dobrijevic, T. Fouchet, T. Guillot, P. Hartogh, T. Hewagama, M.D. Hofstadter, V. Hue, R. Hueso, J.-P. Lebreton, E. Lellouch, J. Moses, G.S. Orton, J.C. Pearl, A. Sánchez-Lavega, A. Simon, O. Venot, J.H. Waite, R.K. Achterberg, S. Atreya, F. Billebaud, M. Blanc, F. Borget, B. Brugger, S. Charnoz, T. Chiavassa, V. Cottini, L. d'Hendecourt, G. Danger, T. Encrenaz, N.J.P. Gorius, L. Jorda, B. Marty, R. Moreno, A. Morse, C. Nixon, K. Reh, T. Ronnet, F.-X. Schmider, S. Sheridan, C. Sotin, P. Vernazza, G.L. Villanueva

PII: S0032-0633(17)30273-8

DOI: [10.1016/j.pss.2017.10.005](https://doi.org/10.1016/j.pss.2017.10.005)

Reference: PSS 4407

To appear in: *Planetary and Space Science*

Received Date: 27 July 2017

Revised Date: 4 October 2017

Accepted Date: 9 October 2017

Please cite this article as: Mouis, O., Atkinson, D.H., Cavalié, T., Fletcher, L.N., Amato, M.J., Aslam, S., Ferri, F., Renard, J.-B., Spilker, T., Venkatapathy, E., Wurz, P., Aplin, K., Coustenis, A., Deleuil, M., Dobrijevic, M., Fouchet, T., Guillot, T., Hartogh, P., Hewagama, T., Hofstadter, M.D., Hue, V., Hueso, R., Lebreton, J.-P., Lellouch, E., Moses, J., Orton, G.S., Pearl, J.C., Sánchez-Lavega, A., Simon, A., Venot, O., Waite, J.H., Achterberg, R.K., Atreya, S., Billebaud, F., Blanc, M., Borget, F., Brugger, B., Charnoz, S., Chiavassa, T., Cottini, V., L. d'Hendecourt, , Danger, G., Encrenaz, T., Gorius, N.J.P., Jorda, L., Marty, B., Moreno, R., Morse, A., Nixon, C., Reh, K., Ronnet, T., Schmider, F.-X., Sheridan, S., Sotin, C., Vernazza, P., Villanueva, G.L., Scientific rationale for Uranus and Neptune *in situ* explorations, *Planetary and Space Science* (2017), doi: 10.1016/j.pss.2017.10.005.

This is a PDF file of an unedited manuscript that has been accepted for publication. As a service to our customers we are providing this early version of the manuscript. The manuscript will undergo copyediting, typesetting, and review of the resulting proof before it is published in its final form. Please

note that during the production process errors may be discovered which could affect the content, and all legal disclaimers that apply to the journal pertain.

Scientific rationale for Uranus and Neptune *in situ* explorations

O. Mousis^a, D. H. Atkinson^b, T. Cavalié^c, L. N. Fletcher^d, M. J. Amato^e, S. Aslam^e, F. Ferri^f, J.-B. Renard^g, T. Spilker^h, E. Venkatapathyⁱ, P. Wurzi^j, K. Aplin^k, A. Coustenis^c, M. Deleuil^a, M. Dobrijevic^l, T. Fouchet^c, T. Guillot^m, P. Hartoghⁿ, T. Hewagama^o, M. D. Hofstadter^b, V. Hue^p, R. Hueso^q, J.-P. Lebreton^g, E. Lellouch^c, J. Moses^r, G. S. Orton^b, J. C. Pearl^e, A. Sánchez-Lavega^q, A. Simon^e, O. Venot^s, J. H. Waite^p, R. K. Achterberg^o, S. Atreya^t, F. Billebaud^l, M. Blanc^v, F. Borget^u, B. Brugger^a, S. Charnoz^w, T. Chiavassa^u, V. Cottini^o, L. d'Hendecourt^u, G. Danger^u, T. Encrenaz^c, N. J. P. Gorius^x, L. Jorda^a, B. Marty^y, R. Moreno^c, A. Morse^z, C. Nixon^e, K. Reh^b, T. Ronnet^a, F.-X. Schmider^m, S. Sheridan^z, C. Sotin^b, P. Vernazza^a, G. L. Villanueva^e

^aAix Marseille Université, CNRS, LAM (Laboratoire d'Astrophysique de Marseille) UMR 7326, 13388, Marseille, France

^bJet Propulsion Laboratory, California Institute of Technology, 4800 Oak Grove Dr., Pasadena, CA 91109, USA

^cLESIA, Observatoire de Paris, PSL Research University, CNRS, Sorbonne Universités, UPMC Univ. Paris 06, Univ. Paris Diderot, Sorbonne Paris Cité, 5 place Jules Janssen, 92195 Meudon, France

^dDepartment of Physics & Astronomy, University of Leicester, University Road, Leicester, LE1 7RH, UK

^eNASA Goddard Space flight Center, Greenbelt, MD 20771, USA

^fUniversità degli Studi di Padova, Centro di Ateneo di Studi e Attività Spaziali "Giuseppe Colombo" (CISAS), via Venezia 15, 35131 Padova, Italy

^gCNRS-Université d'Orléans, 3a Avenue de la Recherche Scientifique, 45071 Orléans Cedex 2, France

^hSolar System Science & Exploration, Monrovia, USA

ⁱNASA Ames Research Center, Moffett field, California, USA

^jSpace Science & Planetology, Physics Institute, University of Bern, Sidlerstrasse 5, 3012 Bern, Switzerland

^kDepartment of Physics, University of Oxford, Denys Wilkinson Building, Keble Road, Oxford OX1 3RH, UK

^lLaboratoire d'astrophysique de Bordeaux, University Bordeaux, CNRS, B18N, allée Geoffroy Saint-Hilaire, 33615 Pessac, France

^mObservatoire de la Côte d'Azur, Laboratoire Lagrange, BP 4229, 06304 Nice cedex 4, France

ⁿMax-Planck-Institut für Sonnensystemforschung, Justus von Liebig Weg 3, 37077 Göttingen, Germany

^oUniversity of Maryland, College Park, MD 20742, USA

^pSouthwest Research Institute, San Antonio, TX 78228, USA

^qDepartamento Física Aplicada I, Escuela des Ingeniería de Bilbao, UPV/EHU, 48013 Bilbao, Spain

^rSpace Science Institute, 4750 Walnut Street, Suite 205, Boulder, CO 80301, USA

^sLaboratoire Interuniversitaire des Systèmes Atmosphériques (LISA), UMR CNRS 7583, Université Paris Est Créteil et Université Paris Diderot, Institut Pierre Simon Laplace, 94000 Créteil, France

Email address: olivier.mousis@lam.fr (O. Mousis)

^t*Department of Atmospheric, Oceanic, and Space Sciences, University of Michigan, Ann Arbor, MI 48109-2143, USA*

^u*Aix-Marseille Université, PIIM UMR-CNRS 7345, F-13397 Marseille, France*

^v*Institut de Recherche en Astrophysique et Planétologie (IRAP), CNRS/Université Paul Sabatier, 31028 Toulouse, France*

^w*Institut de Physique du Globe, Sorbonne Paris Cité, Université Paris Diderot/CNRS, 1 rue Jussieu, 75005, Paris, France*

^x*The Catholic University of America, Washington, DC 20064, USA*

^y*CRPG-CNRS, Nancy-Université, 15 rue Notre Dame des Pauvres, 54501 Vandoeuvre-lès-Nancy, France*

^z*Department of Physical Sciences, The Open University, Walton Hall, Milton Keynes MK7 6AA, UK*

Abstract

The ice giants Uranus and Neptune are the least understood class of planets in our solar system but the most frequently observed type of exoplanets. Presumed to have a small rocky core, a deep interior comprising $\sim 70\%$ heavy elements surrounded by a more dilute outer envelope of H_2 and He, Uranus and Neptune are fundamentally different from the better-explored gas giants Jupiter and Saturn. Because of the lack of dedicated exploration missions, our knowledge of the composition and atmospheric processes of these distant worlds is primarily derived from remote sensing from Earth-based observatories and space telescopes. As a result, Uranus's and Neptune's physical and atmospheric properties remain poorly constrained and their roles in the evolution of the Solar System not well understood. Exploration of an ice giant system is therefore a high-priority science objective as these systems (including the magnetosphere, satellites, rings, atmosphere, and interior) challenge our understanding of planetary formation and evolution. Here we describe the main scientific goals to be addressed by a future *in situ* exploration of an ice giant. An atmospheric entry probe targeting the 10-bar level, about 5 scale heights beneath the tropopause, would yield insight into two broad themes: i) the formation history of the ice giants and, in a broader extent, that of the Solar System, and ii) the processes at play in planetary atmospheres. The probe would descend under parachute to measure composition, structure, and dynamics, with data returned to Earth using

a Carrier Relay Spacecraft as a relay station. In addition, possible mission concepts and partnerships are presented, and a strawman ice-giant probe payload is described. An ice-giant atmospheric probe could represent a significant ESA contribution to a future NASA ice-giant flagship mission.

Keywords: Entry probe, Uranus, Neptune, atmosphere, formation, evolution

1 1. Introduction

2 The ice giant planets Uranus and Neptune represent a largely unexplored
3 class of planetary objects, which fills the gap in size between the larger gas giants
4 and the smaller terrestrial worlds. Uranus and Neptune’s great distances have
5 made exploration challenging, being limited to flybys by the Voyager 2 mission
6 in 1986 and 1989, respectively (Lindal et al., 1987, Tyler et al., 1986, Smith et
7 al., 1986, 1989, Lindal, 1992, Stone and Miner, 1989). Therefore, much of our
8 knowledge of atmospheric processes on these distant worlds arises from remote
9 sensing from Earth-based observatories and space telescopes (see e.g. Encre-
10 naz et al. 2000, Karkoschka and Tomasko 2009, 2011, Feuchtgruber et al. 2013,
11 Fletcher et al. 2010, 2014a, Orton et al. 2014a,b, Sromovsky et al. 2014, Lel-
12 louch et al. 2015). Such remote observations cannot provide “ground-truth” of
13 direct, unambiguous measurements of the vertical atmospheric structure (tem-
14 peratures and winds), composition and cloud properties. With the exception
15 of methane, these observations have never been able to detect the key volatile
16 species (NH_3 , H_2S , H_2O) thought to comprise deep ice giant clouds, **and a host**
17 **of minor species remain undetected.** Because of the physical limitations
18 of these remote observations, and the deficiency of *in situ* or close-up measure-
19 ments, Uranus and Neptune’s physical and atmospheric properties are poorly
20 constrained and their roles in the evolution of the Solar System are not well
21 understood.

22 Uranus and Neptune are fundamentally different from the better-known gas
23 giants Jupiter and Saturn. Interior models generally predict a small rocky core,
24 a deep interior of $\sim 70\%$ of heavy elements surrounded by a more diluted outer

25 envelope with a transition at $\sim 70\%$ in radius for both planets (Hubbard et al.,
26 1995, Fortney and Nettelmann, 2010, Helled et al., 2011). Uranus and Neptune
27 also have similar 16 to 17-hour rotation periods that shape their global dynam-
28 ics. For all their similarities, the two worlds are also very different. Uranus
29 is closer to the Sun at ~ 19 AU versus Neptune's 30 AU and the two planets
30 receive solar fluxes of only 3.4 W/m^2 and 1.5 W/m^2 , respectively. However,
31 while Neptune has an inner heat source comparable to the heating received by
32 the Sun, Uranus lacks any detectable internal heat (Pearl et al., 1990), possibly
33 due to a more sluggish internal circulation and ice layers (Smith and Gierasch,
34 1995, Helled and Guillot, 2017). Additionally, the two planets experience very
35 different seasonal variations, as Uranus's 98° obliquity results in extreme sea-
36 sons, compared with Neptune's more moderate 28° obliquity. These extremes
37 of solar insolation have implications for the atmospheric temperatures, cloud
38 formation, photochemistry and general circulation patterns. Perhaps related to
39 these differences, Uranus shows less cloud activity than Neptune, with infre-
40 quent storms (Irwin, 2009), while Neptune's disk was dominated by the Great
41 Dark Spot at the time of the Voyager 2 flyby (Smith et al., 1989, Sromovsky et
42 al., 1993) and by bright cloud systems in more recent years (Hueso et al., 2017).

43 Exploration of an ice giant system is a high-priority science objective, as
44 these systems (including the magnetosphere, satellites, rings, atmosphere, and
45 interior) challenge our understanding of planetary formation and evolution. A
46 mission to Uranus and Neptune could help answer why the ice giants are located
47 at such large distances from the Sun, while several models predict their forma-
48 tion much closer (Levison and Stewart, 2001, Levison et al., 2008, 2011, Gomes
49 et al., 2005, Morbidelli et al., 2005, 2007, Nesvorný, 2011, Batygin and Brown,
50 2010, Batygin et al., 2012). Also, $\sim 35\%$ of the extrasolar planets discovered to
51 date have masses similar to those of Uranus and Neptune and are located at
52 very different orbital distances. Hence, the *in situ* investigation of these planets
53 could provide a useful context to the interpretation of exoplanet observations
54 and favor future development of ice giant formation and evolution theories in
55 general (Schneider et al., 2011). The importance of the ice giants is reflected in

56 NASA's 2011 Decadal Survey, comments from ESA's Senior Survey Committee
57 in response to L2/L3 and M3 mission proposals (Arridge et al., 2012, 2014, Tur-
58 rini et al., 2014) and results of the 2017 NASA/ESA Ice Giants study (Elliott
59 et al., 2017).

60 Since the Voyager encounters, atmospheric processes at play in Jupiter and
61 Saturn have been well characterized by the Galileo and Juno orbiters at Jupiter,
62 and the Cassini orbiter at Saturn. The Galileo probe provided a step-change
63 in our understanding of Jupiter's origins (Owen et al., 1999, Gautier et al.,
64 2001), and similar atmospheric probes for Saturn have been proposed to build
65 on the discoveries of the Cassini mission (Spilker et al., 2011, 2012, Atkinson
66 et al., 2012, 2013, 2014, 2016, Venkatapathy et al., 2012, Mousis et al., 2014a,
67 2016). The cold, distant ice giants are very different worlds from Jupiter and
68 Saturn, and remote studies are considerably more challenging and less mature.
69 An ice-giant probe would bring insights into two broad themes: i) the forma-
70 tion history of Uranus and Neptune and in a broader extent that of the Solar
71 System, and ii) the processes at play in planetary atmospheres. The primary
72 science objectives for an ice-giant probe would be to measure the bulk compo-
73 sition, and the thermal and dynamic structure of the atmosphere. The Uranus
74 and Neptune atmospheres are primarily hydrogen and helium, with significant
75 abundances of noble gases and isotopes that can only be measured by an *in*
76 *situ* probe. Although the noble gases and many isotopes are expected to be
77 well-mixed and therefore measurements in the upper atmosphere will suffice,
78 there are also a number of condensable species that form cloud layers at depths
79 that depend on abundance of the condensibles and the atmospheric thermal
80 structure. Additionally, disequilibrium species upwelling from the deeper, hot-
81 ter levels of Uranus and Neptune provide evidence of abundances and chemistry
82 in deeper regions unreachable by the probe. Noble gas abundances are diag-
83 nostics of the formation conditions under which the ice and gas giants formed.
84 The condensable species forming different cloud layers are indications of the
85 protosolar nebula (PSN) at the location of planetary formation, and the deliv-
86 ery mechanism of additional heavy elements to the planets. The locations of

87 the cloud decks also affect the thermal and dynamical structure of Uranus's and
88 Neptune's atmospheres. The abundances of disequilibrium species are expected
89 to change with altitude, and reflect deep atmospheric chemistries as well as the
90 magnitude of convection and vertical mixing.

91 This paper describes the main scientific goals to be addressed by the future
92 *in situ* exploration of an ice giant. These goals will become the primary objec-
93 tives listed in a future Uranus or Neptune probe proposal, possibly as a major
94 European contribution to a future NASA ice giant flagship mission. Many of
95 these objectives are within the reach of a shallow probe reaching the 10-bar
96 level. Section 2 is devoted to a comparison between known elemental and iso-
97 topic compositions of Uranus, Neptune, Saturn and Jupiter. We present the
98 different giant planets formation scenarios and the key measurements at Uranus
99 and Neptune that allow disentangling between them. In Section 3, after having
100 reviewed the current knowledge of the atmospheric dynamic and meteorology
101 of the two ice giants, we provide the key observables accessible to an atmo-
102 spheric probe to address the different scientific issues. Section 4 is dedicated
103 to a short description of the mission concepts and partnerships that can be
104 envisaged. In Section 5, we provide a description of a possible ice-giant probe
105 model payload. Conclusions are given in Section 6.

106 **2. Insights on Uranus and Neptune's Formation from their Elemental** 107 **and Isotopic Compositions**

108 In the following sections, we discuss the constraints that can be supplied by
109 atmospheric probe measurements to the current formation and interior models
110 of Uranus and Neptune. We first discuss the current interior models and the
111 existing elemental and isotopic measurements made in the two giants. We then
112 address the question of the measurement of the key disequilibrium species to
113 assess the oxygen abundance in the two planets, a key element to understand
114 their formation. Finally, we outline the measurement goals and requirements
115 of an atmospheric probe in either of these planets, and how such a mission can

116 improve our understanding of the formation conditions and evolution of these
117 enigmatic worlds.

118 *2.1. Interior Models*

119 The presence of Uranus and Neptune in our solar system raises the question
120 of how they formed in the framework of the standard theories of planetary
121 formation. Both existing formation models, namely the *core accretion* and the
122 *disk instability* models, are challenged to explain the physical properties of the
123 two planets.

124 In the *core accretion* model, the formation of a giant planet starts with the
125 coagulation of planetesimals followed by core growth, concurrent accretion of
126 solids and gas onto the core, and finally by the rapid accretion of a massive
127 gaseous envelope (Mizuno, 1980, Hubickyj et al., 2005, Pollack et al., 1996). If
128 Uranus and Neptune formed at their current orbits, the lower surface density
129 of solids and long orbital periods require that the coagulation of planetesimals
130 proceeds much slower than in the gas giant planet region. Under those circum-
131 stances, the ice giants would require formation timescales exceeding the lifetime
132 of the PSN if they accreted *in situ* (Pollack et al., 1996). In realistic simula-
133 tions of growth from planetesimals, giant planets cores clear gaps which prevent
134 growth to critical mass before the disk dissipates on \sim Myr timescales (Levison
135 et al., 2010). Planetary migration has then been suggested to overcome this
136 issue and might solve the problem (Trilling et al., 1998, Alibert et al., 2004,
137 Edgar, 2007, Alexander and Armitage, 2009, Helled and Bodenheimer, 2014).
138 Some help may come from the existence of an outer reservoir of solids in the pro-
139 tosolar disk in the form of pebbles (Lambrechts and Johansen, 2012). Levison et
140 al. (2015) show that this may explain the formation of the giant planets in our
141 Solar System. Note also that Uranus and Neptune probably formed closer to
142 Jupiter and Saturn **prior their outwards migration** (Tsiganis et al., 2005).

143 In the *disk instability* model, giant planets directly form from gas as a re-
144 sult of gravitational instabilities in a cold disk with a mass comparable to that
145 adopted in the *core accretion* model (Boss, 1997, Mayer et al., 2002). In this

146 case, the growth of disk perturbations leads to the formation of density enhance-
 147 ments in disk regions where self-gravity becomes as important as, or exceeds the
 148 stabilizing effects of pressure and shear. To account for their physical proper-
 149 ties, it has been proposed that ice giants could consist of remnants of gas giants
 150 that formed from disk instability, and whose cores would have formed from the
 151 settling of dust grains in the envelopes prior to their photoevaporation by a
 152 nearby OB star (Boss et al., 2002).

153 Furthermore, the interiors of Uranus and Neptune are poorly constrained. A
 154 recent study by Nettelmann et al. (2013) based on improved gravity field data
 155 derived from long-term observations of the planets' satellite motions suggests
 156 however that Uranus and Neptune could present different distributions of heavy
 157 elements. These authors estimate that the bulk masses of heavy elements are
 158 $\sim 12.5 M_{\oplus}$ for Uranus and $\sim 14\text{--}14.5 M_{\oplus}$ for Neptune. They also find that
 159 Uranus would have an outer envelope with a few times the solar metallicity
 160 which transitions to a heavily enriched ($\sim 90\%$ of the mass in heavy elements)
 161 inner envelope at 0.9 planet's radius. In the case of Neptune, this transition
 162 is found to occur deeper inside at 0.6 planet's radius and accompanied with a
 163 more moderate increase in metallicity.

164 2.2. Uranus and Neptune's Composition

165 The composition of giant planets is diagnostic of their formation and evolu-
 166 tion history. Measuring their heavy element, noble gas, and isotope abundances
 167 reveals the physico-chemical conditions and processes that led to formation of
 168 the planetesimals that eventually fed the forming planets (e.g. Owen et al. 1999,
 169 Gautier et al. 2001, Hersant et al. 2001).

170 Heavy element abundances can be derived through a variety of remote tech-
 171 niques (e.g., radio occultation, spectroscopy). However, the most significant
 172 step forward regarding our knowledge of giant planet internal composition was
 173 achieved with the *in situ* descent of the Galileo probe into the atmosphere of
 174 Jupiter (Young, 1998, Folkner et al., 1998, Ragent et al., 1998, Atkinson et al.,
 175 1998, Sromovsky et al., 1998, Niemann et al., 1998, von Zahn et al., 1998).

176 The various experiments enabled the determination of the He/H₂ ratio with
177 a relative accuracy of 2% (von Zahn et al., 1998), of several heavy element
178 abundances and of noble gases abundances (Niemann et al., 1998, Atreya et
179 al., 1999, Wong et al., 2004). These measurements have paved the way to a
180 better understanding of Jupiter’s formation. The uniform enrichment observed
181 in the data (see Figure 1) indeed tends to favor a *core accretion* scenario for this
182 planet (e.g. (Alibert et al., 2005b, Guillot, 2005), even if the gravitational cap-
183 ture of planetesimals by the proto-Jupiter formed via *disk instability* may also
184 explain the observed enrichments (Helled et al., 2006). On the other hand, the
185 condensation processes that formed the protoplanetary ices remain uncertain,
186 because the Galileo probe probably failed at measuring the deep abundance of
187 oxygen by diving into a dry area of Jupiter (Atreya et al., 2003). Achieving
188 this measurement by means of remote radio observations is one of the key and
189 most challenging goals of the Juno mission (Matousek, 2007, Helled and Lunine,
190 2014), currently in orbit around Jupiter.

191 At Saturn, the data on composition are scarcer (see Figure 1) and have
192 mostly resulted from Voyager 2 measurements and intense observation cam-
193 paigns with the Cassini orbiter. The Helium abundance is highly uncertain
194 (Conrath et al., 1984, Conrath and Gautier, 2000, Achterberg et al., 2016), and
195 only the abundances of N, C, and P, have been quantified (Courtin et al., 1984,
196 Davis et al., 1996, Fletcher et al., 2007, 2009a,b). This rarity is the reason why
197 the opportunity of sending an atmospheric probe to Saturn has been studied
198 (Mousis et al., 2014a), and now proposed to ESA and NASA in the M5 and NF4
199 (respectively) mission frameworks (Mousis et al., 2016, Atkinson et al., 2016).

200 Uranus and Neptune are the most distant planets in our Solar System. Their
201 apparent size in the sky is roughly a factor of 10 smaller than Jupiter and Saturn,
202 which makes observations much more challenging in terms of detectability. This
203 distance factor is probably also the reason why space agencies have not yet sent
204 any new flyby or orbiter mission to either of these planets since Voyager 2. As
205 a consequence, the knowledge of their bulk composition is dramatically low (see
206 Figure 1), resulting in a poor understanding of their formation and evolution. To

207 improve this situation significantly enough, we need ground-truth measurements
 208 that can only be carried out in these distant planets by an atmospheric probe,
 209 similarly to the Galileo probe at Jupiter. In the following paragraphs, we present
 210 the current knowledge on the internal composition of the two ice giants (see
 211 Tables 1 and 2), which is mainly inferred from observations of the main reservoirs
 212 of the various heavy elements.

213 2.2.1. Helium

214 The He abundance was first measured by Voyager 2 in both planets during
 215 the respective flybys. Conrath et al. (1987, 1991) report He mass ratios of
 216 $Y=0.262\pm 0.048$ and 0.32 ± 0.05 for Uranus and Neptune, respectively, for an
 217 H_2 -He mixture. Lodders et al. (2009) give a protosolar He mass ratio of 0.278
 218 when considering H_2 and He only, leading to the puzzling situation where He
 219 was nominally almost protosolar in Uranus and super-protosolar in Neptune.
 220 Considering small amounts of N_2 in the mixture (with an extreme upper limit
 221 of 0.6% in volume), Conrath et al. (1993) revised the Neptune value down
 222 to $Y = 0.26 \pm 0.04$, in agreement with the protosolar value. More recently,
 223 Burgdorf et al. (2003) have confirmed the value of Conrath et al. (1993), by
 224 constraining the He mass ratio to $0.264^{+0.026}_{-0.035}$ from far infrared spectroscopy.

225 All these Y values assume only H_2 and He in the gas mixture, as they were
 226 derived from measurements all sensitive to atmospheric levels where CH_4 was
 227 condensed. Below the CH_4 cloud base, the CH_4 mole fraction is in the range of
 228 1–5% in both planets (see 2.2.2). At those levels, the nominal values of the He
 229 mass ratios in Uranus and Neptune then scale to 0.193–0.247 and 0.193–0.247,
 230 respectively, when accounting for CH_4 (5% and 1%, respectively).

231 In any case, the rather high uncertainty levels on the He abundance makes it
 232 difficult to properly constrain interior and evolution models (Guillot, 2005), as
 233 the error bars still encompass sub- to super-protosolar values. An accurate *in*
 234 *situ* measurement of the He/ H_2 ratio is thus required to clarify the situation. We
 235 note that different datasets and/or different analysis methods never converged
 236 to a consensus value for He/H in Jupiter or Saturn from remote sensing only

237 (e.g. [Conrath et al. 1984](#), [Conrath and Gautier 2000](#), and [Achterberg et al. 2016](#)
238 for Saturn). So basically, He/H is achievable from *in situ* only.

239 2.2.2. Carbon

240 Among heavy element bearing species, only methane, carbon monoxide and
241 hydrogen cyanide have been measured so far in the tropospheres of Uranus
242 and Neptune ([Marten et al., 1993](#), [Encrenaz et al., 2004](#), [Lellouch et al., 2005](#)).
243 Methane is the main reservoir of carbon at observable levels. However, its
244 deep value remains uncertain because the measurements are inherently more
245 complicated than in the well-mixed atmospheres of Jupiter and Saturn. Methane
246 indeed condenses at the tropopauses of Uranus and Neptune and the observation
247 of its deep abundance cannot be extrapolated from observations probing the
248 stratosphere or the upper troposphere (e.g. [Lellouch et al. 2015](#)). The first
249 measurements obtained from Voyager-2 radio occultations ([Lindal et al., 1987](#),
250 [Lindal, 1992](#)) and ground-based spectroscopy ([Baines et al., 1995](#)) indicate a
251 mole fraction of 2% in both tropospheres. Coincidentally, these observations
252 all pointed to high latitudes, either because of the ingress/egress latitude of the
253 radio occultation experiments or of the latitudes available from the ground at the
254 time the observations were performed. Interestingly, more recent disk-resolved
255 Hubble Space Telescope observations tend to reveal a more complex situation.
256 [Karkoschka and Tomasko \(2009, 2011\)](#) and [Sromovsky et al. \(2011, 2014\)](#) show
257 that the abundance of methane at the equator is twice higher ($4\pm 1\%$), and that
258 the high latitude depletion in methane may be caused by meridional circulation
259 and condensation.

260 2.2.3. Nitrogen and sulfur

261 N and S are supposedly enriched in the interiors of the ice giants (e.g. [Owen](#)
262 [and Encrenaz 2003](#), [Hersant et al. 2004](#), [Mousis et al. 2014b](#)) and they are car-
263 ried by ammonia (NH_3) and hydrogen sulfide (H_2S) in giant planet upper tro-
264 pospheres. **They form a cloud of solid NH_4SH deep in the troposphere,**
265 **at altitudes corresponding to 30–40 bars,** given the low tropospheric tem-

266 peratures of ice giants. Therefore, the most abundant of the two species will not
267 be entirely consumed by the formation of the NH_4SH cloud, and the remaining
268 excess can then be transported up to the **condensation levels of either of**
269 **NH_3 or H_2S to form clouds between 5 and 10 bars**, as illustrated in
270 [DeBoer and Steffes \(1994\)](#).

271 NH_3 has been observed in both gas giants and H_2S in Jupiter. In Saturn,
272 there are observational hints at the presence of H_2S ([Briggs and Sackett, 1989](#)).
273 On the other hand, neither of these species has been unambiguously detected
274 in ice giants. Radio-wave observations ([de Pater et al., 1989, 1991](#), [Greve et al.,](#)
275 [1994](#), [Weiland et al., 2011](#)) reveal an absorption plateau around 1 cm wavelength
276 in the brightness temperature spectrum of both planets. NH_3 and H_2S both
277 have spectral lines in this wavelength range that could result in this broad
278 absorption feature. In Neptune for instance, if it is NH_3 that produces the
279 absorption, then its mole fraction is $\sim 10^{-6}$ between the NH_4SH and NH_3 cloud
280 base levels ([de Pater et al., 1991](#)). However, this value is not representative of
281 the deep nitrogen abundance. Similarly, if the centimetric absorption is caused
282 by upper tropospheric H_2S , then its mole fraction in the upper troposphere is
283 $\sim 10^{-4}$ ([DeBoer and Steffes, 1994, 1996](#)), but is also not representative of the
284 deep sulfur value. To reach such upper tropospheric value, the most recent
285 model requires S to be 10–50 times solar and N \sim solar ([Luszcz-Cook et al.,](#)
286 [2013](#)). In both hypotheses, the S/N ratio is found to be super-solar ([DeBoer](#)
287 [and Steffes, 1996](#)).

288 Thus, the presumed NH_4SH cloud makes measurements of NH_3 and/or H_2S
289 above the cloud insufficient to constrain the deep N/H or S/H elemental abun-
290 dances. Uranus and Neptune must be probed at least below the 30 and 50 bar
291 levels, respectively. However, and following Juno results on NH_3 profile re-
292 trievals presented in [Bolton et al. \(2017\)](#), measuring the bulk N and S abun-
293 dances in Uranus and Neptune may require probing much deeper than the antici-
294 pated condensation level of those species. **In any case, these determinations**
295 **are out of reach of a shallow probe reaching the 10-bar level.**

296 *2.2.4. Oxygen*

297 Oxygen is one of the key elements in the formation process of giant planets,
298 as H₂O ice was presumably one of the most abundant species in planetesimals
299 beyond the H₂O snowline at the time of planet formation. Measuring its pre-
300 cise abundance in the interior of giant planets bears implications on the location
301 where planet formed. The C/O ratio is an important probe in this respect (e.g.
302 [Ali-Dib et al. 2014](#), [Mousis et al. 2012, 2014b](#), [Öberg et al. 2011](#), [Öberg and](#)
303 [Bergin 2016](#)). The deep O abundance can further help us understand what
304 was the main process that led to the condensation of protoplanetary ices and
305 trapping of other heavy elements. Adsorption on amorphous ice ([Bar-Nun et](#)
306 [al., 1988](#), [Owen et al., 1999](#), [Owen and Encrenaz, 2003, 2006](#)) and clathration
307 ([Lunine and Stevenson, 1985](#), [Gautier et al., 2001](#), [Gautier and Hersant, 2005](#),
308 [Alibert et al., 2005a](#), [Mousis et al., 2006](#)) are the main scenarios described in
309 the literature. They predict large O enrichments, but different in magnitude.
310 The amorphous ice scenario predicts similar enrichments for oxygen and car-
311 bon ([Owen and Encrenaz, 2003](#)). On the other hand, the clathration scenario
312 predicts an oxygen abundance ~ 4 times the carbon abundance ([Mousis et al.,](#)
313 [2014b](#)).

314 The temperature profile of Uranus and Neptune has been measured by Voy-
315 ager 2 radio occultations down to the 2-bar pressure level ([Lindal et al., 1987,](#)
316 [1990](#)). Dry or wet adiabatic extrapolation to lower levels shows us that H₂O
317 condensation level resides at very high pressure levels of 200–300 bars ([Luszcz-](#)
318 [Cook et al., 2013](#), [Cavalié et al., 2017](#)). An atmospheric probe would thus need
319 to reach such depths to measure directly O in Uranus and Neptune. Similar to
320 attempts with Juno at Jupiter, radio waves around 13.5 cm can, in principle,
321 probe down to such depths to characterize the broad absorption from H₂O ([Ma-](#)
322 [tousek, 2007](#)). However, the lack of knowledge of the deep thermal lapse rate,
323 especially in the H₂O condensation zone, makes it very challenging to disentangle
324 temperature from opacity effects on the radio spectrum of each planet. A
325 third possibility for deriving the deep O abundance consists in measuring the

326 upper tropospheric abundance of a disequilibrium O-bearing species that traces
327 the O abundance at deep levels. Thermochemical modeling then enables deriv-
328 ing the deep O abundance that is responsible for the observed abundance. This
329 indirect approach is presented in more detail in section 2.3. So far, it has led to
330 the prediction that the interior of Neptune is extraordinarily enriched in O with
331 respect to the solar value, by a factor of 400 to 600, and that Uranus could be
332 enriched in O by up to a factor of 260 (Lodders and Fegley, 1994, Luszcz-Cook
333 et al., 2013, Cavalié et al., 2017).

334 2.2.5. Phosphorus

335 Contrary to the gas giant case, ice giant spectra have not yet yielded a
336 detectable levels of PH_3 and an upper limit of 0.1 times the solar value was
337 derived by Moreno et al. (2009) in the upper troposphere in the saturation
338 region of PH_3 . Thus, it is not an upper limit on the deep P/H. The lack
339 of evidence for PH_3 in ice giants may be caused by a large deep O/H ratio.
340 Visscher and Fegley (2005) have shown that PH_3 is converted into P_4O_6 at
341 levels where thermochemical equilibrium prevails. A large O abundance may be
342 the cause of the PH_3 depletion **in the upper tropospheres of Uranus and**
343 **Neptune.**

344 2.3. Indirect Determination of Uranus and Neptune's Deep O Abundance

345 Observations of disequilibrium species is one of the methods that can help us
346 complete the determination of the deep elemental composition of giant planets
347 like Uranus and Neptune. Assuming both planets are convective and that their
348 interiors **have been fully mixed once in their history**, we can apply ther-
349 mochemical modeling in their tropospheres to link upper stratospheric measure-
350 ments of disequilibrium species to their deep heavy element abundances. The
351 abundances of disequilibrium species are indeed fixed at the level where the
352 timescale of vertical mixing caused by convection becomes shorter than their
353 thermochemical destruction timescale. Using disequilibrium species to estimate
354 the abundance of a deep species is particularly useful in the case of species for

355 which it is very difficult to reach the levels where they are well-mixed. The
356 typical example is O, which is primarily carried by H₂O in giant planet deep
357 tropospheres. Observation in the upper troposphere of CO, a disequilibrium
358 species chemically linked to H₂O via the net thermochemical reaction $\text{CO} +$
359 $3\text{H}_2 = \text{H}_2\text{O} + \text{CH}_4$, can thus help us indirectly estimate the deep O abundance
360 by applying thermochemistry and diffusion models.

361 More or less comprehensive, thermochemical quenching and/or kinetics and
362 diffusion models have been applied to the giant-planet tropospheres in the past
363 decades (Prinn and Barshay, 1977, Fegley and Prinn, 1985, 1988, Lodders and
364 Fegley, 1994, Bézard et al., 2002, Visscher and Fegley, 2005, Luszcz-Cook et al.,
365 2013, Cavalié et al., 2014, Wang et al., 2016, Cavalié et al., 2017). These
366 models estimate vertical mixing, extrapolate the measured upper tropospheric
367 temperatures to the deep troposphere, and describe the thermochemical reac-
368 tions at work. Theoretical work describes tropospheric mixing in giant planets
369 (Wang et al., 2015) and provides us with estimates. While Neptune with its ex-
370 traordinarily high tropospheric CO (Marten et al., 1993, 2005, Guilloteau et al.,
371 1993, Lellouch et al., 2005, 2010, Fletcher et al., 2010) and very strong internal
372 heat flux (Pearl and Conrath, 1991) is probably fully convective and well-mixed,
373 the very low (or absent) internal heat of Uranus (Pearl et al., 1990) seems to
374 indicate that Uranus is either not fully convective or that it has lost most of
375 its internal heat early in its history (e.g. early giant impact theory, Benz et al.
376 1989). Chemical networks have significantly improved over the last few years
377 (Moses et al., 2011, Venot et al., 2012), but there is still space for improvement
378 in the understanding of oxygen chemistry, as shown by Moses (2014) and Wang
379 et al. (2016). Moreover, the deep tropospheric temperature profile remains quite
380 uncertain. Until very recently, dry or wet adiabatic extrapolations were used
381 (e.g. Lodders and Fegley 1994, Luszcz-Cook et al. 2013, Cavalié et al. 2014)
382 in giant planet tropospheres. Guillot (1995), Leconte and Chabrier (2012) and
383 Leconte et al. (2017) have shown that the situation might be more complex in
384 water-rich interiors, as the temperature profile may significantly depart from
385 adiabatic behavior with the presence of a thin super-adiabatic layer at the H₂O

386 condensation level. The influence of such thermal profiles has been explored by
387 [Cavalié et al. \(2017\)](#) in Uranus and Neptune. For a given chemical scheme, they
388 show that applying the new thermal profiles result in much lower O abundances
389 compared to cases where dry/wet adiabats are used. Their nominal models
390 (chemistry, mixing, temperature profile, etc.) show that O is <160 times the
391 solar value in Uranus and 540 times solar in Neptune. However, the limitations
392 detailed above remain to be waived for thermochemical and diffusion model
393 results to be more solid.

394 CO is not the sole disequilibrium species that can be used to constrain the
395 deep oxygen abundance of giant planets. [Visscher and Fegley \(2005\)](#) have shown
396 that PH₃ is destroyed by H₂O in the deep troposphere (in the 1000-bar region
397 ; [Fegley and Prinn 1985](#)), following the net thermochemical reaction $4\text{PH}_3 +$
398 $6\text{H}_2\text{O} = \text{P}_4\text{O}_6 + 12\text{H}_2$. Measuring the upper tropospheric abundance of PH₃
399 (i.e. below its condensation level) can provide us with a complementary deter-
400 mination of the deep oxygen abundance. To be able to apply this principle to
401 Uranus and Neptune, thermochemical models need to be extended to P species.
402 In this sense, the chemical network proposed by [Twarowski \(1995\)](#) for phos-
403 phorus and oxygen species is certainly one starting point, although one would
404 need to validate such a scheme. One would now need to validate such a scheme
405 to the pressure-temperature conditions relevant for Uranus and Neptune deep
406 tropospheres, in the same manner the H-C-O-N network of [Venot et al. \(2012\)](#)
407 was.

408 Sending an atmospheric probe to either or both ice giants to measure the
409 upper tropospheric CO and PH₃ (below its condensation level) by means of a
410 neutral mass spectrometer, with the aim of constraining the deep O abundance,
411 would undoubtedly boost theoretical and laboratory work to improve current
412 thermochemical models.

413 *2.4. Isotopic Measurements at Uranus and Neptune*

414 Table 3 represents the isotopic ratio measurements realized in the atmo-
415 spheres of the four giant planets of our solar system. It shows that the only

416 isotopic ratio currently available for Uranus and Neptune is the D/H ratio,
417 which was measured by Herschel-PACS (Feuchtgruber et al., 2013). The case
418 of D/H deserves further *in situ* measurements because Herschel observations
419 sampled the pressure in the 0.001–1.5 bar range and deeper sounding could put
420 important constraints on the interiors of Uranus and/or Neptune. The deu-
421 terium enrichment as measured by Feuchtgruber et al. (2013) in both planets
422 has been found very close from one another, and its super-solar value suggests
423 that significant mixing occurred between the protosolar H₂ and the H₂O ice
424 accreted by the planets. Assuming that the D/H ratio in H₂O ice accreted
425 by Uranus and Neptune is cometary ($1.5\text{--}3 \times 10^{-4}$), Feuchtgruber et al. (2013)
426 found that 68–86% of the heavy component consists of rock and 14–32% is made
427 of ice, values suggesting that both planets are more rocky than icy, assuming
428 that the planets have been fully mixed. Alternatively, based on these obser-
429 vations, Ali-Dib et al. (2014) suggested that, if Uranus and Neptune formed
430 at the carbon monoxide line in the PSN, then the heavy elements accreted by
431 the two planets would mostly consists of a mixture of CO and H₂O ices, with
432 CO being by far the dominant species. This scenario assumes that the accreted
433 H₂O ice presents a cometary D/H and allows the two planets to remain ice-rich
434 and O-rich while providing D/H ratios consistent with the observations. Deeper
435 sounding with an atmospheric probe should allow investigating the possibility
436 of isotopic fractionation with depth.

437 The measurement of the D/H ratio in Uranus and/or Neptune should be
438 complemented by a precise determination of ³He/⁴He in their atmospheres to
439 provide further constraints on the protosolar D/H ratio, which remains rela-
440 tively uncertain. The protosolar D/H ratio is derived from ³He/⁴He measure-
441 ments in the solar wind corrected for changes that occurred in the solar corona
442 and chromosphere consequently to the Sun’s evolution, and to which the pri-
443 mordial ³He/⁴He is subtracted (Geiss and Gloeckler, 1998). This latter value
444 is currently derived from the ratio observed in meteorites or in Jupiter’s atmo-
445 sphere. The measurement of ³He/⁴He in Uranus and/or Neptune atmospheres
446 would therefore complement the Jupiter value and the scientific impact of the

447 protosolar D/H derivation.

448 The $^{14}\text{N}/^{15}\text{N}$ ratio presents large variations in the different planetary bodies
449 in which it has been measured and, consequently, remains difficult to inter-
450 pret. The analysis of Genesis solar wind samples (Marty et al., 2011) suggests
451 a $^{14}\text{N}/^{15}\text{N}$ ratio of 441 ± 5 , which agrees with the remote sensing (Fouchet
452 et al., 2000) and *in situ* (Wong et al., 2004) measurements made in Jupiter's
453 atmospheric ammonia, and the lower limit derived from ground-based mid-
454 infrared observations of Saturn's ammonia absorption features (Fletcher et al.,
455 2014b). **The two $^{14}\text{N}/^{15}\text{N}$ measurements made in Jupiter and Sat-
456 urn suggest that primordial N_2 was probably the main reservoir of
457 the NH_3 present in their atmospheres (see Owen et al. 2001, Mousis
458 et al. 2014a,b for details).** On the other hand, Uranus and Neptune are
459 mostly made of solids (rocks and ices) (Guillot, 2005) that may share the same
460 composition as comets. N_2/CO has been found strongly depleted in comet
461 67P/Churyumov-Gerasimenko (Rubin et al., 2015), i.e. by a factor of ~ 25.4
462 compared to the value derived from protosolar N and C abundances. This con-
463 firms the fact that N_2 is a minor nitrogen reservoir compared to NH_3 and HCN in
464 this body (Le Roy et al., 2015), and probably in other comets (Bockelée-Morvan
465 et al., 2004). In addition, $^{14}\text{N}/^{15}\text{N}$ has been measured to be 127 ± 32 and 148
466 ± 6 in cometary NH_3 and HCN respectively (Rousselot et al., 2014, Manfroid
467 et al., 2009). Assuming that Uranus and Neptune have been accreted from the
468 same building blocks as those of comets, then one may expect a $^{14}\text{N}/^{15}\text{N}$ ratio
469 in these two planets close to cometary values, and thus quite different from the
470 Jupiter and Saturn values. Measuring $^{14}\text{N}/^{15}\text{N}$ in the atmospheres of Uranus
471 and Neptune would provide insights about the origin of primordial nitrogen
472 reservoir in these planets. Moreover, measuring this ratio in different species
473 would enable us to constrain the relative importance of the chemistry induced
474 by galactic cosmic rays and magnetospheric electrons (see Dobrijevic and Loison
475 2017 for an example in Titan).

476 The isotopic measurements of carbon, oxygen and noble gas (Ne, Ar, Kr,
477 and Xe) isotopic ratios should be representative of their primordial values. For

478 instance, only little variations are observed for the $^{12}\text{C}/^{13}\text{C}$ ratio in the solar
 479 system irrespective of the body and molecule in which it has been measured.
 480 Table 3 shows that both ratios measured in the atmospheres of Jupiter and
 481 Saturn are consistent with the terrestrial value of 89. A new *in situ* measurement
 482 of this ratio in Uranus and/or Neptune should be useful to confirm the fact that
 483 their carbon isotopic ratio is also telluric.

484 The oxygen isotopic ratios also constitute interesting measurements to be
 485 made in Uranus and Neptune’s atmospheres. The terrestrial $^{16}\text{O}/^{18}\text{O}$ and
 486 $^{16}\text{O}/^{17}\text{O}$ isotopic ratios are 499 and 2632, respectively (Asplund et al., 2009). At
 487 the high accuracy levels achievable with meteorite analysis, these ratios present
 488 some small variations (expressed in δ units, which are deviations in part per
 489 thousand). Measurements performed in comets Bockelée-Morvan et al. (2012),
 490 far less accurate, match the terrestrial $^{16}\text{O}/^{18}\text{O}$ value. The $^{16}\text{O}/^{18}\text{O}$ ratio has
 491 been found to be ~ 380 in Titan’s atmosphere from Herschel SPIRE observa-
 492 tions but this value may be due to some fractionation process (Courtin et al.,
 493 2011, Loison et al., 2017). On the other hand, Serigano et al. (2016) found val-
 494 ues consistent with the terrestrial ratios in CO with ALMA. The only $^{16}\text{O}/^{18}\text{O}$
 495 measurement made so far in a giant planet was obtained from ground-based
 496 infrared observations in Jupiter’s atmosphere and had a too large uncertainty
 497 to be interpreted (1–3 times the terrestrial value; Noll et al. (1995)).

498 2.5. Volatile Enrichments at Uranus and Neptune

499 The direct or indirect measurements of the volatile abundances in the at-
 500 mospheres of Uranus and Neptune are key **for deciphering** their formation
 501 conditions in the PSN. In what follows, we present the various models and their
 502 predictions regarding enrichments in the two ice giants. All predictions are
 503 summarized in Figure 2.

504 2.5.1. Disk Instability Model

505 The formation scenario of these planets proposed via the *disk instability*
 506 *model*, associated with the photoevaporation of their envelopes by a nearby OB

507 star and settling of dust grains prior to mass loss (Boss et al., 2002), implies
508 that O, C, N, S, Ar, Kr and Xe elements should all be enriched by a similar
509 factor relative to their protosolar abundances in their respective envelopes, as-
510 suming that mixing is efficient. Despite the fact that interior models predict
511 that a metallicity gradient may increase the volatile enrichments at growing
512 depth in the planet envelopes (Nettelmann et al., 2013), there is no identified
513 process that may affect their relative abundances in the ice giant envelopes, if
514 the sampling is made at depths below the condensation layers of the concerned
515 volatiles and if thermochemical equilibrium effects are properly taken into ac-
516 count. The assumption of homogeneous enrichments for O, C, N, S, Ar, Kr and
517 Xe, relative to their protosolar abundances, then remains the natural outcome
518 of the formation scenario proposed by Boss et al. (2002).

519 2.5.2. Core Accretion and Amorphous Ice

520 In the case of the *core accretion* model, because the trapping efficiencies of
521 C, N, S, Ar, Kr and Xe volatiles are similar at low temperature in amorphous
522 ice (Owen et al., 1999, Bar-Nun et al., 2007), the delivery of such solids to the
523 growing Uranus and Neptune is also consistent with the prediction of homo-
524 geneous enrichments in volatiles relative to their protosolar abundances in the
525 envelopes, still under the assumption that there is no process leading to some
526 relative fractionation between the different volatiles.

527 2.5.3. Core Accretion and Clathrates

528 In the *core accretion* model, if the volatiles were incorporated in clathrate
529 structures in the PSN, then their propensities for trapping strongly vary from a
530 species to another. For instance, Xe, CH₄ and CO₂ are easier clathrate formers
531 than Ar or N₂ because their trapping temperatures are higher at PSN conditions,
532 assuming protosolar abundances for all elements (Mousis et al., 2010). This
533 competition for trapping is crucial when the budget of available crystalline water
534 is limited and does not allow the full clathration of the volatiles present in
535 the PSN (Gautier et al., 2001, Mousis et al., 2012, 2014b). However, if the O

536 abundance is 2.6 times protosolar or higher at the formation locations of Uranus
 537 and Neptune’s building blocks and their formation temperature does not exceed
 538 $\sim 45\text{K}$, then the abundance of crystalline water should be high enough to fully
 539 trap all the main C, N, S and P-bearing molecules, as well as Ar, Kr and Xe
 540 (Mousis et al., 2014b). In this case, all elements should present enrichments
 541 comparable to the C measurement, except for O and Ar, based on calculations
 542 of planetesimals compositions performed under those conditions (Mousis et al.,
 543 2014b). The O enrichment should be at least ~ 4 times higher than the one
 544 measured for C in the envelopes of the ice giants due to its overabundance
 545 in the PSN. In contrast, the Ar enrichment is decreased by a factor of ~ 4.5
 546 compared to C, due to its very poor trapping at 45 K in the PSN (see Figure
 547 2). We refer the reader to Mousis et al. (2014b) for further details about the
 548 calculations of these relative abundances.

549 2.5.4. Photoevaporation Model

550 An alternative scenario is built upon the ideas that (i) Ar, Kr and Xe were
 551 homogeneously adsorbed at very low temperatures ($\sim 20\text{--}30\text{ K}$) at the surface
 552 of amorphous icy grains settling in the cold outer part of the PSN midplane
 553 (Guillot and Hueso, 2006) and that (ii) the disk experienced some chemical
 554 evolution in the giant planets formation region (loss of H_2 and He), due to
 555 photoevaporation. In this scenario, **these icy grains migrated toward the**
 556 **formation region of the giant planets** in which they subsequently released
 557 their trapped noble gases, due to increasing temperature. Because of the disk’s
 558 photoevaporation inducing fractionation between H_2 , He and the other heavier
 559 species, these noble gases would have been supplied in supersolar proportions
 560 with the PSN gas to the forming Uranus and Neptune. The other species, whose
 561 trapping/condensation temperatures are higher, would have been delivered to
 562 the envelopes of Uranus and Neptune in the form of amorphous ice or clathrates.
 563 Guillot and Hueso (2006) predict that, while supersolar, the noble gas enrich-
 564 ments should be more moderate than those resulting from the accretion of solids
 565 containing O, C, N, S by the two giants.

566 *2.5.5. CO Snowline Model*

567 Another scenario, proposed by [Ali-Dib et al. \(2014\)](#), suggests that Uranus
 568 and Neptune were both formed at the location of the CO snowline in a stationary
 569 disk. Due to the diffusive redistribution of vapors (the so-called *cold finger*
 570 *effect*; [Stevenson and Lunine 1988](#), [Cyr et al. 1998](#)), this location of the PSN
 571 intrinsically had enough surface density to form both planets from carbon-
 572 and oxygen-rich solids but nitrogen-depleted gas. The analysis has not been
 573 extended to the other volatiles but this scenario predicts that species whose
 574 snowlines are beyond that of CO remain in the gas phase and are significantly
 575 depleted in the envelope compared to carbon. Under those circumstances, one
 576 should expect that Ar presents the same depletion pattern as for N in the
 577 atmospheres of Uranus and Neptune. In contrast, Kr, Xe, S and P should be
 578 found supersolar in the envelopes of the two ice giants, but to a lower extent
 579 compared to the C and O abundances, which are similarly very high ([Ali-Dib](#)
 580 [et al., 2014](#)).

581 *2.6. Summary of Key Measurements*

582 In what follows, we list the key measurements to be performed by an at-
 583 mospheric entry probe at Uranus and Neptune, in order to better constrain
 584 formation and evolution of these planets:

- 585 • Temperature–pressure profile from the stratosphere down to at least 10
 586 bars, because it would help to constrain the opacity properties of clouds
 587 laying at or above these levels (CH₄ and NH₃ or H₂S clouds). Around
 588 2 bars, where CH₄ condenses, convection may be inhibited by the mean
 589 molecular weight gradient ([Guillot, 1995](#)) and it is thus important to mea-
 590 sure the temperature gradient in this region.
- 591 • Tropospheric abundances of C, N, S, and P, down to the 40-bar level at
 592 least (especially for N and S existing in the form of NH₄SH clouds), with
 593 accuracies of $\pm 10\%$ (of the order of the protosolar abundance accuracies).
 594 However, these determinations are out of reach of a shallow probe reaching

595 the 10-bar level. Alternatively, N and S could be measured remotely at
 596 microwave wavelengths by a Juno-like orbiter.

- 597 • Tropospheric abundances of noble gases He, Ne, Xe, Kr, Ar, and their
 598 isotopes to trace materials in the subreservoirs of the PSN. The accuracy
 599 on He should be at least as good as the one obtained by Galileo at Jupiter
 600 ($\pm 2\%$), and the accuracy on isotopic ratios should be $\pm 1\%$ to enable direct
 601 comparison with other known Solar System values.
- 602 • Isotopic ratios in hydrogen (D/H) and nitrogen ($^{15}\text{N}/^{14}\text{N}$), with accuracies
 603 of $\pm 5\%$, and in oxygen ($^{17}\text{O}/^{16}\text{O}$ and $^{18}\text{O}/^{16}\text{O}$) and carbon ($^{13}\text{C}/^{12}\text{C}$) with
 604 accuracies of $\pm 1\%$. This will enable us to determine the main reservoirs
 605 of these species in the PSN.
- 606 • Tropospheric abundances of CO and PH_3 . Having both values puts oppo-
 607 site constraints on the deep H_2O (Visscher and Fegley, 2005). CO alone
 608 may not be sufficient to enable the evaluation of the deep H_2O because of
 609 the uncertainties on the deep thermal profile (convection inhibition possi-
 610 ble at the H_2O condensation level) as shown in Cavalié et al. (2017).

611 3. In situ studies of Ice Giant Atmospheric Phenomena

612 In the following sections, we review the atmospheric dynamics and meteorol-
 613 ogy of Uranus and Neptune. We explore the scientific potential for a probe in-
 614 vestigating atmospheric dynamics and meteorology, clouds and hazes and chem-
 615 istry. We also provide the key observables accessible to an atmospheric probe
 616 to address these different scientific issues.

617 3.1. Ice Giant Dynamics and Meteorology

618 3.1.1. Ice Giant Global Winds

619 Uranus and Neptune have zonal winds characterised by a broad retrograde
 620 equatorial jet and nearly symmetric prograde jets at high latitudes. Both have
 621 very intense winds with Neptune possessing the strongest winds within the

622 Solar System, with its retrograde equatorial jet reaching velocities of -400 m/s
623 and prograde winds at high latitudes reaching velocities of 270 m/s (Figure 3).
624 These wind systems are very different to the multi-jet circulations of Jupiter
625 and Saturn with westward equatorial jets.

626 Winds have been measured on both planets from observations of discrete
627 cloud features gathered by Voyager 2 (Smith et al., 1986, 1989, Limaye and
628 Sromovsky, 1991, Karkoschka, 2015), Hubble Space Telescope (Sromovsky et al.,
629 1995, 2001, Karkoschka, 1998, Hammel et al., 2001) and Keck (Sromovsky, 2005,
630 Hammel et al., 2005, Sromovsky et al., 2009, Martin et al., 2012) over multiple
631 decades. The intensity of the winds has appeared to be relatively consistent
632 over time, although there is a large degree of dispersion in the measurements,
633 and it is not clear that the features are genuinely tracking the underlying wind
634 fields (see Sánchez-Lavega, 2017, for a recent review).

635 Multi-spectral imaging allows sensing of different cloud altitudes from levels
636 at around 60 mbar to 2 bar (Irwin et al., 2016a,b). Most of the wind analysis
637 show large dispersions with the majority of the observations being sensitive to
638 the upper troposphere (100-200 mbar). It is generally considered that the zonal
639 winds could vary up to 10% as a consequence of vertical wind shear and tracers
640 at different altitudes. However, the clouds used to track zonal winds may or
641 may not move in the underlying wind fields and large variability is seen. Long-
642 duration, short-cadence monitoring of light curves of Neptune by Spitzer and
643 Kepler show that the clouds vary on very short time scales (Simon et al., 2016,
644 Stauffer et al., 2016). Similar rapid evolution is seen on the small clouds of
645 Uranus (Irwin et al., 2017).

646 *In situ* measurements of the deep winds below the observable cloud levels,
647 which are thought to be located at the 2–3 bar level, are key to understanding
648 the nature of the jets on the ice giants. Theoretical models of the origin of
649 atmospheric jets in giant planets are divided in two families: jets could be
650 driven by solar heat flux and shallow atmospheric processes including a crucial
651 role of moist convection in the troposphere (Lian and Showman, 2010, and
652 references therein); or they could extend deep into the planetary interiors (Suomi

653 [et al., 1991](#), [Aurnou et al., 2007](#)). By monitoring the descent trajectory of an
654 atmospheric probe, in conjunction with measuring the aerosols comprising the
655 visible clouds, we will gain insights into the vertical structure of the ice giant
656 winds for the first time.

657 *3.1.2. Global Banding, Meridional and Vertical Circulation*

658 Visible and near-infrared imaging of the ice giants reveal that clouds con-
659 sist of three types – zonal banding, discrete bright spots, and dark ovals (see
660 Section 3.1.3). The zonal bands have low albedo contrast and their meridional
661 extent (5° - 20° in latitude) is unrelated to the zonal winds and atmospheric
662 temperature structure. In the case of Uranus, since the equinox occurred in
663 December 2007, both hemispheres have been observed at high spatial resolution
664 following the Voyager-2 flyby. The banding distribution was observed in the
665 northern hemisphere in the visible range on Voyager-2 highly processed images
666 ([Karkoschka, 2015](#)), and in the southern hemisphere in the red and near-infrared
667 wavelengths ([Sromovsky et al., 2015](#)). Uranus' south polar region extends up to
668 mid latitudes about 45 - 50° S and appears to be bright and featureless. However,
669 the North Pole showed a large number of small-scale bright spots in the near
670 infrared images ([Sromovsky et al., 2015](#)), suggestive of convective motions. The
671 bright spots strongly resemble the cloud pattern seen in the polar regions of
672 Saturn ([Del Genio et al., 2009](#)).

673 Latitudinally-resolved thermal and compositional data of Uranus and Nep-
674 tune provide hints of the overall meridional and vertical atmospheric circulation
675 associated with this banded structure. On Neptune, infrared observations from
676 Voyager were interpreted by [Conrath et al. \(1991\)](#) and [Bézard et al. \(1991\)](#) in
677 terms of a global circulation system with rising cold air at mid latitudes and
678 overall descent at the Equator and the polar latitudes. Neptune's summertime
679 pole exhibits a warm vortex in the troposphere and stratosphere that appears
680 bright in the mid-infrared as a consequence of the polar subsidence ([Orton et al.,](#)
681 [2007](#), [Fletcher et al., 2014a](#)). The same atmospheric circulation could explain
682 the overall cloud structure in the planet with enhanced storm activity at mid-

683 latitudes, and is consistent with modern infrared and radio-wave observations
684 (Fletcher et al., 2014a, Luszcz-Cook et al., 2013, de Pater et al., 2014). Uranus
685 exhibits a similar pattern, with cool mid-latitudes and a warm equatorial band
686 in the upper troposphere (Flasar et al., 1987, Orton et al., 2015). However,
687 the circulation on both worlds may be much more complex, **with suggestions**
688 **of higher molecular abundances at the equator**. The observation that
689 tropospheric methane is enhanced at the equators of both planets compared
690 to the poles (Sromovsky et al., 2011, Karkoschka and Tomasko, 2011) suggests
691 a different circulation pattern with equatorial upwelling rather than equatorial
692 subsidence. Ammonia may be similarly enhanced at Uranus' equator (de Pater
693 et al., 1991, Hofstadter and Butler, 2003). The nature of ice giant circulation
694 patterns is therefore the subject of considerable debate.

695 Intriguingly, the relationship between temperatures, winds and the banded
696 appearance of a giant planet is less clear-cut on Uranus and Neptune than it
697 is on their gas giant cousins. An atmospheric probe, simultaneously measuring
698 temperatures, winds and aerosol properties, could help to resolve this problem,
699 and to provide insights into the sense of the ice giant circulation patterns. On
700 both Uranus and Neptune, the temperatures in the upper atmosphere are low
701 enough for the equilibration between the ortho- (parallel) and para-hydrogen
702 (anti-parallel) states to play a role in vertical atmospheric dynamics, making
703 measurements of the distribution of the hydrogen ortho-to-para fraction an es-
704 sential indicator of the global circulation in these planets (e.g., Conrath et al.,
705 1998). The ortho-to-para ratio is dependent on temperature and has a long
706 equilibration time. The ortho-to-para ratio affects the overall atmospheric lapse
707 rate and can explain the low heat flux of Uranus (Smith and Gierasch, 1995)
708 since Voyager data showed that Uranus' lapse rate and ortho-to-para fraction
709 are not consistent (Gierasch and Conrath, 1987). This may indicate thin strat-
710 ified layers, with fast vertical displacements, such that para-H₂ does not get
711 redistributed (de Pater and Massie, 1985, Gierasch and Conrath, 1987). In
712 Uranus the ortho to para-H₂ ratio varies significantly with both altitude and
713 latitude (Conrath et al., 1998, Fouchet et al., 2003, Orton et al., 2015) with

714 a north-south hemispheric asymmetry consistent with the spin-axis tilt of the
715 planet. For Neptune, recent ortho-to-para measurements (Fletcher et al., 2014a)
716 suggest that para-H₂ disequilibrium is symmetric about the equator, with super-
717 equilibrium conditions at the equator and tropics and at high southern latitudes,
718 and sub-equilibrium conditions at mid-latitudes in both hemispheres. This dis-
719 equilibrium is consistent with a meridional circulation with cold air rising at
720 mid-latitudes and subsiding at both the poles and the equator, in agreement
721 with other inferences of the global circulation.

722 Despite these findings, there exists a degeneracy between measurements of
723 tropospheric temperature, the abundance of helium and the ortho-to-para ra-
724 tio. This degeneracy cannot be resolved via remote observations alone, and
725 implies that the vertical para-H₂ fraction and its impact on the atmospheric
726 lapse rate is highly uncertain. An atmospheric probe able to measure each of
727 these parameters simultaneously (as well as determining the helium abundance
728 – see Sec. 2.2.1) would be vital to understand the different sources of energy
729 driving ice giant atmospheric circulations. Additionally an atmospheric probe
730 would also help resolve uncertainties in remote retrieval of temperatures that
731 assume collision-induced H₂ absorption, which depends on the ortho-to-para
732 ratio.

733 3.1.3. Meteorology of Uranus and Neptune and Convection

734 The results from an ice giant atmospheric probe would have to be inter-
735 preted in light of the different meteorological features that have been observed
736 in Uranus and Neptune. Figure 4 shows the visual aspect of both planets at
737 a variety of wavelengths from the visible to the near infrared. Both planets
738 show a recursive but random atmospheric activity at cloud level that can be
739 observed in the methane absorption bands as bright spots (Sromovsky et al.,
740 1995). Typically, sizes of these features range from 1,000 to 5,000 km. Discrete
741 bright spots are regularly captured at red wavelengths (0.6 - 2.2 μm) in both
742 planets (but more frequently on Neptune than Uranus). They appear as bright
743 in the methane absorption bands because of their high cloud tops. In Uranus,

744 most of the discrete cloud features are located at the altitude of the methane ice
745 cloud or at deeper levels. The brightest features on Uranus are detected at 2.2
746 μm and reach an altitude level of 300–600 mbar, while part of these features are
747 much deeper, being in the lower cloud at 2–3 bars. Uranus’s storm activity is
748 more scarce than Neptune’s, but can reach a high degree of intensity as occurred
749 in 2014–15 in the latitudes 30°–40°N (de Pater et al., 2015, Irwin et al., 2016a,
750 2017). Because of the large obliquity of Uranus, seasonal changes in the cloud
751 and hazes structure are observed, and this requires a long-term survey to de-
752 termine the altitude where they occur and understand the mechanisms behind
753 their formation under the extremely variable solar insolation conditions.

754 Neptune displays both types of discrete cloud activity: episodic and continu-
755 ous (Baines and Hammel, 1994, Sromovsky et al., 1995). Recently, images taken
756 by the amateur community using improved observing and processing techniques,
757 have been able to capture such features on this planet (Hueso et al., 2017). On
758 the other hand, the images taken in an ample range of wavelengths from about
759 400 nm to 2.2 μm indicate that the clouds are located at higher altitude levels
760 than in Uranus, with cloud tops at around 20–60 mbar whereas other storms are
761 at the ~ 2 bar level (Irwin et al., 2016a,b).

762 This discrete cloud activity could be the result of convective motions, al-
763 though the sources of energy (ortho-para- H_2 conversion, or latent heat release
764 from condensing volatiles) are highly uncertain. Early models of moist convec-
765 tion on Neptune were examined by Stoker and Toon (1989), but moist convective
766 storms do not appear to be particularly active on this planet. On Uranus, be-
767 sides the large long-lived storm system known as the Berg (de Pater et al., 2011,
768 Sromovsky et al., 2015), only a few clouds have been considered as signatures of
769 moist convection in the south polar latitudes (de Pater et al., 2014). However,
770 the relatively low number of high-resolution observations of both planets result
771 in an inability to determine the frequency of moist convective storms in both
772 Uranus and Neptune.

773 Another way to study moist convective processes is via detections of atmo-
774 spheric electricity. Lightning on both Uranus (Zarka and Pedersen, 1986) and

775 Neptune was detected by Voyager 2, but Neptunian lightning seems weaker, or
776 has a much slower rise time, than Uranian lightning (Gurnett et al., 1990, Kaiser
777 et al., 1991). This is unexpected, as Neptune’s internal heat source should lead
778 to more convective activity than Uranus. The mechanism for lightning genera-
779 tion is not known, but since both Neptune and Uranus contain clouds of polar-
780 izable mixed-phase material such as water and ammonia, then a terrestrial-like
781 mechanism seems possible. Detection of lightning by an atmospheric probe
782 would allow characterisation of the relative strengths and frequencies of light-
783 ning, and would enable a deeper understanding of convective and cloud processes
784 at the ice giant planets.

785 Beyond lightning, atmospheric electrical processes may also contribute to
786 cloud formation at Neptune through ion-induced nucleation producing cloud
787 condensation nuclei, a mechanism first suggested by Moses et al. (1992). Ioni-
788 sation from cosmic rays was closely associated with Neptune’s long-term albedo
789 fluctuations by Aplin and Harrison (2016).

790 Besides the zonal banding and the small-scale bright clouds associated with
791 convective activity, the third most prominent cloud type are larger systems,
792 such as the dark ovals. Dark oval spots are notable in Neptune where they
793 become conspicuous at blue-green wavelengths. The archetype was the Great
794 Dark Spot (GDS) captured in detail at visible wavelengths in images obtained
795 during the Voyager 2 flyby in 1989 (Smith et al., 1989, Baines and Hammel,
796 1994, LeBeau and Dowling, 1998). The GDS was first observed at latitude
797 20°S, but after drifting towards the equator it disappeared in about one year.
798 The GDS had a size of 15,500 km (East-West) \times 6,000 km (North-South) and
799 according to the ambient wind profile was an anticyclonic vortex. At least four
800 additional smaller dark vortices have been reported from latitudes 32°N to 55°S
801 following the Voyager-2 flyby. Bright clouds accompanying the dark ovals are
802 observed at red and near infrared wavelengths and are thought to be the result
803 of air forced upward by the vortex, known as orographic clouds (Stratman et
804 al., 2001). Other dark spots in Neptune have been observed with similar bright
805 cloud companions, which are thought to develop similarly to orographic clouds

806 by the interaction of the zonal winds with the dark anticyclone. There is only
807 one report of a dark spot in Uranus similar to Neptune’s GDS that was observed
808 in visible wavelengths in 2006 at 28°N. It had a size of 1,300 km (North-South)
809 \times 2,700 km (East-West) (Hammel et al., 2009).

810 Unlike in Jupiter and Saturn, these large-scale systems can drift meridion-
811 ally and disappear after a few years moving in the direction of the equator.
812 Some features in Uranus may survive several years like the large Berg feature
813 (Sromovsky et al., 2015). A South Polar Feature in Neptune has been observed
814 since the Voyager observations (Karkoschka, 2011) and seems to have a convec-
815 tive origin.

816 3.1.4. *Temperature Structure of Uranus and Neptune*

817 The vertical temperature structure is important as a fundamental constraint
818 on dynamics and chemistry in planetary atmospheres. Voyager-2 radio-occultation
819 results for Uranus (Lindal et al., 1987) and Neptune (Lindal, 1992) have pro-
820 vided a sample of the temperature profiles in these atmospheres with a high
821 vertical resolution for a distinct region of each atmosphere. However, as noted
822 above, these results cannot be interpreted in the absence of knowledge of the
823 mean molecular weight, which has been solved simultaneously with simultane-
824 ous sensing of infrared radiance in the sampled regions to constrain the bulk
825 composition. This, in turn, relies to some extent on knowledge of the ortho vs.
826 para H₂ ratio. Thus it is important to establish all of these for at least one point
827 in the atmosphere to serve as a reference standard for thermal-infrared remote-
828 sensing instruments on a carrier or orbiter, or for more distant remote-sensing
829 observations. Differences have been noted between the radio occultation results
830 and models for the globally-averaged temperature profile for Uranus (see Orton
831 et al., 2014a, and references therein) and Neptune (see Fletcher et al., 2014a,
832 and references therein). Thus, remote-sensing observations of the atmospheric
833 probe entry site will be extremely useful to establish the context of the local at-
834 mospheric conditions. This was vital to the interpretation of the Galileo probe
835 entry site, which turned out not to be representative of global particulate and

836 condensate distributions (Orton et al., 1998).

837 **To understand the mechanism for heating the upper atmospheric**
 838 **layers, and to distinguish between solar heating and wave heating**
 839 **(e.g., via gravity waves emanating from the deeper atmosphere), it**
 840 **will be important to measure the temperature structure through the**
 841 **upper stratosphere and thermosphere.** These levels are well above the re-
 842 gion to which the radio-occultation measurements are sensitive. Temperatures
 843 are currently characterised only broadly in altitude by a mixture of solar and
 844 stellar occultations measured by the Voyager-2 Ultraviolet Spectrometer and
 845 ground-based visible observations with large uncertainties and internal incon-
 846 sistencies (Herbert et al., 1987, Bishop et al., 1992, French et al., 1998, Young et
 847 al., 2001, Uckert et al., 2014). Measurements by a probe accelerometer will pro-
 848 vide substantial information on both upper-atmospheric temperatures, as well
 849 as detailed characterisation of gravity waves that contribute to the maintenance
 850 of temperatures, as was the case for the Galileo probe (Young et al., 1997).

851 3.1.5. Key Observables of Atmospheric Dynamics

852 Here, we list the key measurements to be made by an atmospheric entry
 853 probe at Uranus and Neptune to assess their atmospheric dynamics:

- 854 • Probe descent temperature/density profile. Continuous measurements of
 855 atmospheric temperature and pressure throughout the descent **in the 0–**
 856 **10 bar region** would allow the determination of (i) stability regimes
 857 as a function of depth through transition zones (e.g., radiative-convective
 858 boundary); and (ii) the influence of wave perturbations which could also
 859 be used to infer the degree of convection at the probe descent location.
- 860 • **Ortho-to-para ratio.** Measurements of this ratio as a function of
 861 altitude would constrain the degree of vertical convection and
 862 the equilibration times of these disequilibrium states.
- 863 • Probe descent accelerometer measurements. Continuous monitoring of
 864 the descent deceleration will provide a detailed measurement of the at-

865 atmospheric density from which the temperature profile can be derived in a
866 region above that of the direct temperature and pressure measurements.

867 • Probe descent winds. Measurements of the vertical profile of the zonal
868 winds from Doppler tracking of an atmospheric probe would provide an
869 insight into the nature of the winds in an ice giant with a small or negligible
870 deep heat source. Doppler wind measurements provide the wind profile in
871 the lower troposphere, well below the tropopause near the region where
872 most of the cloud tracking wind measurements are obtained. Static and
873 dynamic pressures measured from the Atmospheric Structure Instrument
874 (see Section 5.3) would provide an estimation of the vertical winds, waves,
875 and convection.

876 • Conductivity profile. Measurement of the conductivity profile would indi-
877 cate what type of clouds support sufficient charge separation to generate
878 lightning. Conductivity measurements combined with meteorological and
879 chemical data (particularly measurements of the physical properties of
880 the aerosols themselves) would also permit extraction of the charge dis-
881 tribution on aerosol particles, and improve understanding of the role of
882 electrical processes in cloud formation, lightning generation, and aerosol
883 microphysics.

884 Additionally, further measurements during the approach phase would com-
885 plement the scientific return of the probe:

886 • Cloud-tracking observations from a visible to near IR camera or spectral
887 imager on approach could provide a global two-dimensional view of atmo-
888 spheric dynamics over several weeks at different altitude levels from 2 bar
889 to 60 mbar. This would allow us to understand the probe descent in the
890 context of nearby meteorological features or changes to the zonal banding.

891 • **Mid-infrared measurements from the carrier spacecraft (and con-**
892 **temporaneous ground-based measurements) of the thermal struc-**
893 **ture, ortho-to-para-H₂ distribution and atmospheric composi-**

894 **tion at the probe entry site would provide essential contextual**
895 **information about the dynamics, circulation and chemistry at**
896 **the entry location.**

- 897 • Gravity measurements and deep structure. Measurements obtained by the
898 Voyager 2 flybys imply that the dynamics are confined to a weather layer
899 no deeper than 1,000 km deep in Uranus and Neptune ($\sim 2,000$ bar in
900 Uranus and 4,000 bar in Neptune) (Kaspi et al., 2013). This confinement
901 could be much shallower and information about the deep troposphere be-
902 low the levels accessible to a probe could be attained by measurements of
903 the gravity field of Uranus and Neptune from the trajectory of a carrier
904 or orbiter.
- 905 • Radio wave detection of lightning from the carrier spacecraft, in addi-
906 tion to optical lighting detections from a camera (dominant emissions are
907 expected to be at 656 nm for Uranus and Neptune), would support the
908 investigation of the conductivity probe.

909 *3.2. Ice-Giant Clouds*

910 Our current knowledge of the clouds and hazes on the ice giant planets comes
911 from two main sources: (1) photochemical models of haze and aerosol formation
912 in the upper atmosphere, and thermochemical models based on cloud formation
913 by condensation; (2) analysis of the visible and infrared spectrum by means of
914 radiative-transfer modeling. In the high atmosphere of Uranus and Neptune,
915 methane is photolysed into hydrocarbons (see Section 3.3) that diffuse down
916 and condense to form haze layers in the cold stratospheres (altitude range 0.1
917 to 30 mbar) as the temperature decreases down to ~ 60 K in the tropopause.
918 The photochemical models suggest the formation of hazes made of H_2O , C_6H_6 ,
919 C_4H_2 , C_4H_{10} , CO_2 , C_3H_8 , C_2H_2 , and C_2H_6 from top to bottom (Romani and
920 Atreya, 1988, Romani et al., 1993, West et al., 1990, Baines and Hammel, 1994,
921 Baines et al., 1995, Moses et al., 1995, 2005, Dobrijevic et al., 2010, Moses and

922 [Poppe, 2017](#)), where the oxygen species derive from external sources such as
923 interplanetary dust or comets (Figure 5).

924 Thermochemical equilibrium cloud condensation (ECC) models are based on
925 the vertical temperature and composition distributions. They give the altitude
926 of the formation of the cloud bases and the vertical distribution of the den-
927 sity in the cloud according to the different species that condense and following
928 the saturation vapor pressure curves based on the Clausius-Clapeyron equation
929 ([Sánchez-Lavega et al., 2004](#), [Atreya and Wong, 2005](#)) (Figure 5). Depending
930 on the abundances of the condensables, at least five cloud layers are predicted
931 to form. For deep abundances relative to the solar value of $O/H = 100$, $N/H =$
932 1 , $S/H = 10$ and $C/H = 30-40$, four cloud layers of ice particles of CH_4 , H_2S ,
933 NH_4SH , H_2O form between pressure levels 0.1 bar and 50 bar (representing
934 a vertical distance of about 500 km, Figure 5). The lower water-ice cloud is
935 at the top of a massive aqueous water cloud that could extend down to 1,000
936 bars or more. It should be noted, however, that the existence of a H_2S cloud
937 depends upon sulphur being more abundant than nitrogen on the ice giants.
938 Although this depletion of nitrogen has been suggested by microwave observa-
939 tions, it remains extremely uncertain, and there is a possibility that an NH_3 ice
940 cloud could form if N is more abundant than S, as on Jupiter and Saturn. An
941 atmospheric probe penetrating down to 50–100 bar should sense and measure
942 the properties of all these cloud layers, whereas a shallow probe to 10 bar would
943 reach the H_2S cloud.

944 Visible and near-infrared images of Uranus and Neptune, combined with
945 their reflectance spectra analysed via radiative-transfer models show that, to
946 first order, the structure and properties of the accessible clouds in both Uranus
947 and Neptune are similar. They consist of an extended haze with top at 50-100
948 mbar located above a thin methane cloud of ice condensates with its base at 1.3
949 bar. This cloud is above another cloud of H_2S ice that is thin in thickness but
950 optically thick that is located between 2 and 4 bar or pressure, presumed to be
951 formed by H_2S condensates ([Hammel et al., 1989](#), [Irwin, 2009](#), and references
952 therein). This model, consisting of two cloud layers and an extended haze, has

953 been proposed based on many independent studies, the more recent ones by
954 Tice et al. (2013), de Kleer et al. (2015), Irwin et al. (2016a,b). The effective
955 radius for the stratospheric haze particles is 0.1-0.2 μm and of 1-1.5 μm for the
956 methane tropospheric cloud (West et al., 1990, Baines and Hammel, 1994, Irwin
957 et al., 2017). It should be noted, however, that these inferences from radiative
958 transfer modelling are degenerate, with multiple possible solutions for the op-
959 tical properties (e.g., aerosol composition and refractive indices) and vertical
960 structure. Furthermore, they are being updated all the time as new sources of
961 laboratory data for the cloud and methane absorptions become available. An
962 atmospheric probe would directly test the results of these remote observations,
963 measuring the properties of the aerosols as a function of depth to provide a
964 ground-truth to remote sensing observations, and accessing clouds much deeper
965 than possible from remote platforms.

966 3.2.1. Key Observables of Ice Giant Clouds

967 The clouds of an ice giant are the filter through which remote observations
968 attempt to determine their bulk composition. An atmospheric probe would
969 allow us to constrain the vertical structure and physical properties of the aerosols
970 responsible for the planet's appearance in reflected sunlight, as well as revealing
971 the relationship between the atmospheric lapse rate, gaseous composition, and
972 the resulting aerosols. Key measurements from the atmospheric probe include:

- 973 • Determinations of the properties of the clouds and hazes along the descent
974 path, measuring the scattering properties at a range of phase angles, the
975 number density as a function of depth, the aerosol shape and opacity
976 properties. Each of these measurements would help constrain the aerosol
977 composition.
- 978 • Determine the influence of cloud condensation or photochemical haze for-
979 mation on the temperature lapse rate, and deduce the amount of energy
980 relinquished by this phase change.

- 981 • Determine the effect of cloud formation on the vertical profiles of key
982 condensable species (CH_4 , NH_3 , H_2S).

983 *3.3. Ice-Giant Chemistry*

984 Section 2 provided an overview of the bulk chemical composition and ther-
985 mochemistry of Uranus and Neptune, revealing that of the primary elements
986 heavier than hydrogen and helium (namely carbon, nitrogen, oxygen, sulphur
987 and phosphorus), only carbon has been definitively detected in remote sensing
988 observations in the form of methane and CO. The key cloud-forming volatiles
989 – NH_3 , H_2S and H_2O – remain largely inaccessible to remote sensing, and we
990 have only upper limits on disequilibrium species such as PH_3 . The chemistry
991 of the upper tropospheres and stratospheres of the ice giants is a product of
992 the source material available, as we describe in the following sections. An at-
993 mospheric probe must be able to measure the vertical distributions of gaseous
994 species and aerosols to determine the chemical processes at work on the ice
995 giants, allowing us to contrast (i) the implications of different photochemical
996 mixing efficiencies between Uranus and Neptune; and (ii) the different physical
997 and chemical processes at work on the gas and ice giants. Compositional dif-
998 ferences between these hydrogen-dominated atmospheres can result from many
999 factors, including (Moses et al., 2005): differences in photolytic rates due to
1000 different heliocentric distances; different reaction rates and condensation due to
1001 different atmospheric temperatures; different strengths of atmospheric mixing;
1002 differences in auroral energy and potential ion-neutral chemistry; and different
1003 influxes of material of exogenic origins. Understanding the importance of these
1004 different influences requires a robust, direct measurement of ice giant chemistry.

1005 *3.3.1. Methane Photochemistry*

1006 Despite containing significantly more tropospheric methane than the gas
1007 giants (up to $\sim 4\%$ in mole fraction at low latitudes, Sromovsky et al., 2014,
1008 Karkoschka and Tomasko, 2011), the cold temperatures of the ice giant tropopause
1009 forces methane to condense, acting as an effective cold-trap. However, some

1010 methane gas is able to escape into the stratosphere, either via convective over-
1011 shooting or slow diffusion through warmer regions (e.g., [Orton et al., 2007](#)),
1012 where it helps to heat the stratosphere via solar absorption in the near-infrared,
1013 yielding the stratospheric inversions on Uranus and Neptune. Once in the strato-
1014 sphere, ultraviolet photolysis of methane initiates a chain of photochemical re-
1015 actions to generate heavier hydrocarbons ([Atreya and Ponthieu, 1983](#), [Summers](#)
1016 [and Strobel, 1989](#), [Romani and Atreya, 1989](#), [Bishop et al., 1992](#), [Moses et al.,](#)
1017 [2005](#), [Dobrijevic et al., 2010](#)) which dominate the mid-infrared emission spec-
1018 tra observed from Earth-based and space-based facilities (e.g., ISO, AKARI
1019 and Spitzer; [Encrenaz et al., 1998](#), [Burgdorf et al., 2006](#), [Meadows et al., 2008](#),
1020 [Fletcher et al., 2010](#), [Orton et al., 2014b](#)), and produce absorptions in UV oc-
1021 culation observations from Voyager (e.g., [Herbert et al., 1987](#), [Bishop et al.,](#)
1022 [1990](#)).

1023 Species detected on both planets so far (Figure 6) include ethane (C_2H_6),
1024 acetylene (C_2H_2), methylacetylene (C_3H_4) and diacetylene (C_4H_2) (e.g., [Burgdorf](#)
1025 [et al., 2006](#), [Orton et al., 2014b](#), [Meadows et al., 2008](#), [Fletcher et al., 2010](#)),
1026 whereas ethylene (C_2H_4) and methyl (CH_3) have only been detected on Nep-
1027 tune ([Bézard et al., 1999](#), [Schulz et al., 1999](#)). Some species, such as propane
1028 (C_3H_8) and benzene (C_6H_6) remain undetected due to the difficulties of separat-
1029 ing their emissions from bright nearby features. The brightness of a particular
1030 emission feature is determined by both the stratospheric temperature profile and
1031 the vertical gaseous distribution, the latter of which is shaped by the strength
1032 of vertical mixing (e.g., upward diffusion and slow settling), the net chemical
1033 production rate profile, the altitude of the photolysis region, and the possibility
1034 of condensation of the hydrocarbons to form haze layers. Measuring temper-
1035 ature and composition remotely is a degenerate problem, and for the species
1036 listed above we rarely have any confidence in the measured vertical profiles.
1037 Furthermore, these profiles are likely to vary with latitude if methane is more
1038 elevated at the equator due to enhanced vertical mixing, or at the poles if CH_4
1039 leaks through warm polar vortices ([Yelle et al., 1989](#), [Greathouse et al., 2011](#),
1040 [Fletcher et al., 2014a](#)), and some species are observed to vary with time (e.g.,

1041 Neptunian ethane, Hammel et al., 2006, Fletcher et al., 2014a). Indeed, hy-
1042 drocarbon production rates depend on solar insolation and will be seasonally
1043 variable, with maximum abundances expected in the summer hemisphere in the
1044 absence of circulation.

1045 Atmospheric circulation, either via large-scale inter-hemispheric transport
1046 as part of some global circulation pattern, or via general diffusive mixing, is
1047 expected to generate observable differences in the methane photochemistry be-
1048 tween Uranus and Neptune (Figure 6). Uranian mixing appears more sluggish,
1049 meaning that CH₄ will not reach such high stratospheric altitudes as on Nep-
1050 tune (i.e., a low methane homopause, Herbert et al., 1987, Bishop et al., 1990),
1051 therefore ensuring that photochemistry on Uranus occurs in a different physical
1052 regime (higher pressures) than on any other giant planet, suppressing photo-
1053 chemical networks (Atreya et al., 1991). This difference can be readily seen in
1054 the ratio of ethane to acetylene, which is much larger than unity on Jupiter,
1055 Saturn and Neptune, but smaller than unity on Uranus. Orton et al. (2014b)
1056 use Spitzer mid-infrared observations of Uranus to demonstrate that the slow
1057 vertical mixing implies that the hydrocarbons are confined to altitudes below
1058 the 0.1-mbar pressure level. Furthermore, they suggest that there is no evi-
1059 dence for an increase in mixing (and therefore hydrocarbon abundances) near
1060 Uranus' 2007 equinox, despite suggestions of an increase in dynamical activity
1061 in the troposphere at this time (see Section 3.1). An atmospheric probe, able to
1062 distinguish the vertical profiles of stratospheric temperature and hydrocarbon
1063 composition (and to potentially detect previously-undetected species), would
1064 allow the first robust tests of stratospheric chemistry models (e.g., Moses et
1065 al., 2005, Orton et al., 2014b) balancing the competing influences of seasonal
1066 photochemistry, vertical mixing and aerosol condensation at work within an ice
1067 giant stratosphere.

1068 3.3.2. Exogenic Species

1069 Section 2.3 described the potential internal source of CO as a disequilibrium
1070 species on Uranus and Neptune and bulk H₂O as a volatile species hidden deep

1071 below the reaches of remote sensing. But H_2O , CO and CO_2 are also present
1072 in ice giant stratospheres from external sources (Figure 6), such as cometary
1073 impacts, satellite debris or ablation of interplanetary dust grains and microm-
1074 eteoroids (e.g., Feuchtgruber et al., 1997, Lellouch et al., 2005, Poppe, 2016,
1075 Moses and Poppe, 2017). Stratospheric water was detected by ISO (Feuchtgru-
1076 ber et al., 1997); CO from the fluorescent emission in the infrared (Encrenaz
1077 et al., 2004, Fletcher et al., 2010) and sub-millimeter emission (Lellouch et al.,
1078 2005, Hesman et al., 2007, Lellouch et al., 2010, Cavalié et al., 2014); Uranus'
1079 CO_2 from Spitzer (Burgdorf et al., 2006, Orton et al., 2014b) and Neptune's
1080 CO_2 from ISO (Feuchtgruber et al., 1997). These oxygenated species can there-
1081 fore play a part in the photochemical reaction pathways along with the methane
1082 photolysis described above. The relative abundances of these three species can
1083 provide clues to their origins (Cavalié et al., 2014, Orton et al., 2014b, Moses
1084 and Poppe, 2017).

1085 The vertical distribution of H_2O and CO_2 is not expected to differ sig-
1086 nificantly between the two planets. However, the oxygen-related chemistry on
1087 Uranus is anomalous because the methane homopause is so low that there is not
1088 a very large interaction region between the hydrocarbons and oxygen species **at**
1089 **altitudes above which the H_2O condenses**, in comparison to Neptune, so
1090 there should be less coupled oxygen-hydrocarbon photochemistry (e.g., Moses
1091 and Poppe, 2017). Neptune is anomalous because CO is significantly enriched
1092 in the upper stratosphere, which likely comes from a large cometary impact
1093 (Lellouch et al., 2005, Hesman et al., 2007, Luszcz-Cook and de Pater, 2013,
1094 Moses and Poppe, 2017). Oxygenated species play other roles in shaping the
1095 stratospheric structure: CO and CO_2 would be photolysed and play a role in
1096 the photochemistry at high altitude, potentially leading to a secondary peak
1097 of hydrocarbon production above the methane homopause level, and therefore
1098 influencing the thermal structure (via excess heating/cooling). Water may con-
1099 dense to form high-altitude haze layers. Finally, stratospheric HCN and CS can
1100 become involved in the chemistry of the stratosphere, potentially originating
1101 from large cometary impacts (Lellouch et al., 2005). HCN can also originate

1102 from galactic-cosmic-ray-induced chemistry of intrinsic N_2 from the interior, or
1103 photochemistry of nitrogen flowing in from Triton (e.g., [Lellouch et al., 1994](#)).
1104 A direct measurement of the vertical distribution of these upper stratospheric
1105 compounds would shed light on their origins and importance in shaping the
1106 conditions in the upper stratospheres of the ice giants.

1107 *3.3.3. Tropospheric Photochemistry*

1108 Disequilibrium species are those that are detectable in a giant-planet upper
1109 troposphere as a result of vigorous vertical mixing. At some pressure deep in
1110 the troposphere (the quench level), the rate of vertical mixing becomes faster
1111 than the rate of thermochemical destruction and the abundance becomes frozen
1112 in at a value representing the quenched equilibrium composition ([Fegley and
1113 Prinn, 1985](#)). On the gas giants Jupiter and Saturn, this provides detectable
1114 amounts of phosphine (PH_3), CO, arsine (AsH_3) and germane (GeH_4) in their
1115 upper tropospheres (e.g., [Taylor et al., 2004](#), [Fletcher et al., 2015](#)). As described
1116 in Section 2.3, only CO has been observed on the ice giants, with no detections
1117 of the other potential disequilibrium species.

1118 However, on Jupiter and Saturn the primary condensable (NH_3) and dise-
1119 quilibrium molecule (PH_3) have vertical profiles that are significantly altered
1120 by the coupled tropospheric photochemistry (e.g., [Atreya et al., 1984](#)). The
1121 same could also be true of H_2S , AsH_3 and GeH_4 ([Fegley and Prinn, 1985](#)). Un-
1122 fortunately, little is known about the reaction pathways for these tropospheric
1123 constituents, but the works of [Kaye and Strobel \(1984\)](#) and [Visscher et al. \(2009\)](#)
1124 suggest that a variety of photo-produced species could exist, including diphos-
1125 phine (P_2H_4), hydrazine (N_2H_4), and gas-phase N_2 . Diphosphine and hydrazine
1126 may condense to form a part of the hazes observed on Jupiter and Saturn, and
1127 photo-processing of these species may contribute to the arrays of observable
1128 colours. These hazes have a feedback effect on the chemistry, sometimes shield-
1129 ing the UV photolysis of deeper gas molecules, and implying that the vertical
1130 distribution of gases above the clouds are sensitive to the strength of transport,
1131 condensation, and the efficiency of the photochemistry. If these species (primar-

1132 ily NH_3 , H_2S and PH_3) can be definitively identified by an atmospheric probe,
1133 then their vertical profiles would reveal much about the competing transport
1134 and chemistry processes at work. This is essential before their deep abundances
1135 can be used to constrain the bulk composition of these planets in Section 2.3.

1136 3.3.4. Key Observables for Atmospheric Chemistry

1137 Section 3.3 has described the rich array of molecular species and aerosols that
1138 could be present on the ice giants as a result of photochemistry of the source
1139 material. The vertical distribution of the source materials (methane, oxygen and
1140 nitrogen compounds, or disequilibrium species) depend on the nature of their
1141 delivery, from vertical mixing, large-scale circulation or external influx. Some of
1142 these source materials and their products are challenging to observe remotely.
1143 Even if their spectral features are identifiable, there remains a fundamental
1144 degeneracy between the vertical temperature and composition that prevents
1145 a comprehensive understanding of the processes involved. Key measurements
1146 providing a ground-truth for these remote sensing measurements include:

- 1147 • Vertical profiles of atmospheric temperature and lapse rates from the
1148 stratosphere into the troposphere.
- 1149 • Multiple direct measurements of atmospheric composition as a function of
1150 altitude to determine photochemical source regions, homopause altitudes,
1151 condensed phases and the influence of the cold trap.
- 1152 • First detections of precursor molecules (e.g., PH_3 , NH_3 , H_2S), their pho-
1153 tochemical products, and constraints on their vertical profiles.
- 1154 • Vertical distribution of aerosols produced via condensation of photolytic
1155 products.

1156 A key challenge for an atmospheric probe to study atmospheric chemistry
1157 is the need to track the thermal structure and chemical composition from high
1158 altitudes, down through the tropopause and into the cloud-forming region.

1159 3.4. Atmospheric Phenomena Summary

1160 A single entry probe descending into the atmosphere of an ice giant would
1161 provide significant new insights into the physical and chemical forces shaping
1162 their observable atmospheres. In addition to providing ground-truth for the
1163 parameters that can be crudely measured remotely – the thermal structure, the
1164 gaseous abundances above the clouds, the windspeeds at the cloud-top, and the
1165 vertical aerosol structures – the probe would provide a wealth of insights into
1166 properties that are inaccessible. These include measuring gaseous species that
1167 are hidden deep below the cloud layers; determining the roles of cloud conden-
1168 sation, vertical mixing and photochemistry in shaping the vertical distributions
1169 of trace species; and measuring temperatures and winds deep below the clouds.
1170 The ice-giant probe measurements will allow the first direct and unambiguous
1171 comparison with the Galileo probe results at Jupiter, to see how the thermal
1172 structure, composition, clouds and chemistry differ between the gas and ice
1173 giants of our solar system.

1174 4. Proposed mission Configuration and Profile

1175 4.1. Probe Mission Concept

1176 4.1.1. Science Mission Profile

1177 To measure the atmospheric composition, thermal and energy structure,
1178 clouds and dynamics requires *in situ* measurements by a probe carrying a mass
1179 spectrometer (atmospheric and cloud compositions), atmospheric structure in-
1180 strument (thermal structure and atmospheric stability), nephelometer (cloud
1181 locations and aerosol properties), net flux radiometer (energy structure), and
1182 Doppler-wind experiment (dynamics). The atmospheric probe descent targets
1183 the 10-bar level located about 5 scale heights beneath the tropopause. The
1184 speed of probe descent will be affected by requirements imposed by the needed
1185 sampling periods of the instruments, particularly the mass spectrometer, as well
1186 as the effect speed has on the measurements. This is potentially an issue for
1187 composition instruments, and will affect the altitude resolution of the Doppler

1188 wind measurement. Although it is expected that the probe batteries, struc-
1189 ture, thermal control, and telecom will allow operations to levels well below 10
1190 bars, a delicate balance must be found between the total science data volume
1191 requirements to achieve the high-priority mission goals, the capability of the
1192 telecom system to transmit the entire science, engineering, and housekeeping
1193 data set (including entry accelerometry and pre-entry/entry calibration, which
1194 must be transmitted interleaved with descent data) within the descent tele-
1195 com/operational time window, and the probe descent architecture which allows
1196 the probe to reach 10 bars.

1197 *4.1.2. Probe Mission Profile to Achieve Science Goals*

1198 A probe to Uranus or Neptune will be carried as one element of a dedicated
1199 ice-giant exploration, likely a NASA flagship mission (Elliott et al., 2017). The
1200 probe is designed for atmospheric descent under parachute to make measure-
1201 ments of composition, structure, and dynamics, with data returned to Earth
1202 using the Carrier Relay Spacecraft (CRSC) as a relay station that will re-
1203 ceive, store, and re-transmit the probe science and engineering data. While
1204 recording the probe descent science and engineering data, the CRSC will make
1205 radio-science measurements of both the probe relay link signal strength from
1206 which abundances of key microwave absorbers in Uranus’s atmosphere can be
1207 retrieved, and probe relay link frequency from which Doppler tracking of the
1208 probe can be performed to retrieve the atmospheric dynamics.

1209 Upon arrival in the vicinity of the ice giant system, the atmospheric probe
1210 will be configured for release, an extended coast, entry, and the atmospheric de-
1211 scent mission. For proper probe delivery to the entry interface point, the CRSC
1212 with probe attached is placed on a planetary-entry trajectory, and is reoriented
1213 for probe release. The probe coast timer and pre-programmed probe descent
1214 science sequence are loaded prior to release from the CRSC, and following a
1215 spin-up period, the probe is released for a ballistic coast to the entry point. It is
1216 beneficial to Doppler track the CRSC prior to, during, and subsequent to the re-
1217 lease event, so that the observed change in CRSC speed can help reconstruct the

1218 probe release dynamics and reduce the uncertainty in the probe arrival location.
1219 If feasible, it is also beneficial to image the probe from the CRSC shortly after
1220 probe release. Optical navigation of the probe relative to background stars can
1221 help reduce the uncertainty in the probe release dynamics, departure trajectory,
1222 and arrival location. Following probe release, a deflect maneuver is performed to
1223 place the CRSC on the proper overflight trajectory for the probe descent relay
1224 communications. An important consideration during probe coast is to ensure
1225 that probe internal temperatures remain within survival range by careful ther-
1226 mal design and management, and, as needed, by batteries. It is important to
1227 recognize an important trade exists between a probe release closer to the planet
1228 (deeper within the planet's gravity well) resulting in a shorter coast period with
1229 less impact on probe thermal control requirements, power, and required battery
1230 complement, as well as a smaller uncertainty in probe entry interface location
1231 but at a cost of a higher ΔV (and therefore more fuel) for the CRSC, vs. an
1232 earlier release requiring a smaller CRSC deflection ΔV and less fuel, but re-
1233 quiring a longer coast, a larger uncertainty in probe-interface arrival location,
1234 and a more significant impact on probe thermal and power. During the coast
1235 period the probe will periodically transmit beacons to the CRSC to provide
1236 probe coast survival and overall health status. However, once released from the
1237 CRSC there is no opportunity to send commands to the probe.

1238 Prior to arrival, the probe coast timer awakens the probe for sequential
1239 power-on, warm-up, and health checks of subsystems and instruments, and to
1240 perform preliminary instrument calibrations. One of the first systems to be pow-
1241 ered on is the ultrastable oscillator that requires an extended warmup period
1242 to achieve operational stability needed to support the Doppler Wind Experi-
1243 ment. Although all instruments are powered on for warmup and calibration,
1244 the only instrumentation collecting data during entry will be the accelerometers
1245 located at the probe center of mass to measure the entry accelerations required
1246 to reconstruct the probe entry trajectory and to retrieve the density profile of
1247 the upper atmosphere. The accelerometers provide a g-switch trigger to initi-
1248 ate parachute deployment and configure the atmospheric probe for its descent

1249 science mission. The parachute sequence is initiated above the tropopause by
1250 firing a mortar through a breakout panel in the aft cover and deploying a pilot
1251 parachute. The pilot parachute pulls off the probe aft cover while extracting the
1252 main descent parachute. After a short period of time, the probe heatshield will
1253 be released and the probe will establish a communication link with the CRSC
1254 and commence descent operations. The need for probe rotation during descent
1255 is not yet well defined, but spin vanes to control minimum and maximum spin
1256 rates and sense will be carefully studied.

1257 Under the parachute, any required mode changes in descent science oper-
1258 ations with altitude can be guided by data from the Atmospheric Structure
1259 Instrument pressure and temperature sensors, thereby providing the opportu-
1260 nity to optimize the data collection for changing science objectives at different
1261 atmospheric depths. To satisfy mission success criteria the probe science data
1262 collection and relay transmission strategy will be designed to ensure the entire
1263 probe science data set is successfully transmitted to the CSRC before the de-
1264 scent probe reaches the targeted depth. Data collected beyond the target depth
1265 will be returned as long as the relay link survives.

1266 The actual descent sequence and timing, main parachute size and descent
1267 speeds, and time to reach the required depth (nominally 10 bars) will depend
1268 upon considerations of instrument science data generation and total data volume
1269 to be returned. During descent, the probe science payload will make measure-
1270 ments in real time, with data buffered for later return. The probe pre-entry and
1271 entry instrument calibration, probe housekeeping, and entry accelerometry data
1272 must also be returned, and is interleaved with the probe descent science and re-
1273 quired engineering/housekeeping data. The probe telecom system will comprise
1274 two cross-polarized channels separated slightly in frequency, with each channel
1275 nominally transmitting identical data sets for redundancy. If extra bandwidth
1276 is required, it is possible to transmit high-priority science and engineering data
1277 on both channels, and to separate lower priority data between the two chan-
1278 nels. To reduce the possibility of data loss during brief relay link dropouts,
1279 the option exists to provide a slight time offset of the two channels. The probe

1280 descent mission will likely end when the telecom geometry becomes so poor that
1281 the link can no longer be maintained, when the probe reaches a depth that the
1282 overlying atmospheric opacity is so large that the link cannot be supported,
1283 or when battery depletion or increasing thermal and/or pressure effects cause
1284 systems in the vented probe to fail. **The concept of operation would be**
1285 **close to the one developed for the Galileo probe entry (see Fig. 9 of**
1286 **Mouis et al. (2016)).**

1287 The CRSC receives the probe data, storing multiple copies in redundant
1288 on-board memory. **At the completion of the probe descent mission and**
1289 **once the post-descent context observations have been performed,** the
1290 CRSC reorients to point the High-Gain Antenna towards Earth and the multiple
1291 copies of the probe science and engineering data are downlinked.

1292 *4.2. Probe Delivery*

1293 *4.2.1. Interplanetary Trajectory*

1294 Four characteristics of interplanetary transfers from Earth to Uranus or Nep-
1295 tune are of primary importance: the launch energy, the duration of the transfer,
1296 the V_∞ of approach (VAP) to the destination planet, and the declination of the
1297 approach asymptote (DAP). The higher the launch energy, the smaller the mass
1298 a given launch vehicle can deliver to that energy. The duration of the transfer is
1299 of particular interest for Uranus and Neptune because their remote locations in
1300 the far outer solar system require transfer times that are a challenge to space-
1301 craft reliability engineering and to radioisotope power systems whose output
1302 power decay with time. The VAP strongly influences the ΔV necessary for or-
1303 bit insertion and the entry speed of an atmospheric entry probe delivered from
1304 approach: a higher VAP requires a higher orbit insertion ΔV and thus more
1305 of the spacecraft's mass devoted to propellant, and increases the entry speed of
1306 the entry probe, requiring a more massive heat shield. The DAP influences the
1307 locations available to an entry probe, and influences the probe's atmosphere-
1308 relative entry speed because it limits the alignment of the entry velocity vector
1309 with the local planetary rotation velocity. Uranus represents an extreme case

1310 (in our solar system). Its 97.7° obliquity can, over 1/4 of a Uranian orbit (~ 21
1311 years), change the average DAP from equator-on to nearly pole-on. These four
1312 characteristics are not entirely independent. Trajectories with short transfer
1313 durations almost invariably have high VAPs. Trajectories with low VAPs can
1314 have high DAPs, especially at Uranus. Mission designers must examine all the
1315 options, assessing the interplay of these characteristics and their implications
1316 for mission risk, cost, and performance.

1317 **Thousands of possible transfer trajectories from Earth to Uranus**
1318 **have been identified, and hundreds to Neptune (Elliott et al., 2017).**
1319 **Depending on transfer design and mass, trajectories to Uranus and**
1320 **Neptune are generally 10–12 years and ~ 13 years, respectively. Sev-**
1321 **eral trajectories have particularly advantageous combinations of char-**
1322 **acteristics and are identified as the best options within that study’s**
1323 **assumed launch window. Similar, and in some cases better options**
1324 **would be available outside of that study’s launch window. For in-**
1325 **stance, when Jupiter and Saturn align to provide gravity assists from**
1326 **both, trajectories with short transfer durations are possible. Thus,**
1327 **if programmatic considerations dictate a particular launch window,**
1328 **there are useful trajectories available for transfers to either Uranus**
1329 **or Neptune.**

1330 *4.2.2. Probe Delivery and Options for Probe Entry Location*

1331 Given a transfer trajectory with its particular VAP and DAP, a remaining
1332 degree of freedom, the “ b ” parameter (the offset of the b -plane aim point from
1333 the planet’s center), determines both the available entry site locations, and the
1334 atmosphere-relative entry speed for each of those locations, and the entry flight
1335 path angle (EFPA). If the probe is delivered and supported by a flyby spacecraft,
1336 designing a trajectory to give data relay window durations of an hour or more is
1337 not difficult. But if the CRSC is an orbiter delivering the probe from hyperbolic
1338 approach, the probe mission must compete with the orbit insertion maneuver
1339 for performance. Orbit insertion maneuvers are most efficiently done near the

1340 planet, saving propellant mass. But such trajectories, coupled with a moderately
1341 shallow probe EFPA that keeps entry heating rates and inertial loads relatively
1342 low, yield impractically short data relay durations. For this type of trajectory,
1343 the orbiter rapidly passes through the probe's data relay antenna beam and the
1344 telecommunications time is much shorter. Steepening the entry (decreasing b)
1345 can increase the window duration and requires the CRSC to be on a trajectory
1346 with a somewhat more distant closest approach, resulting in a slower overflight
1347 and correspondingly increased telecom window, but at the cost of significantly
1348 increased entry heating rates and inertial loads. A different approach to this
1349 problem, described in the NASA Ice Giants Missions study report, but not
1350 analyzed in depth, avoids this situation by delivering the probe to a b-plane
1351 aim point $\sim 180^\circ$ away from the orbiter's aim point. Although this requires a
1352 minor increase in the orbiter's total ΔV for targeting and divert, it allows a
1353 moderate EFPA for the probe while allowing a data relay window of up to two
1354 hours duration.

1355 *4.2.3. Ice Giant Entry Challenges*

1356 The probe aeroshell, provided by NASA and NASA Ames Research Center
1357 will comprise both a heatshield (forward aeroshell) and an aft cover (backshell).
1358 The aeroshell has five primary functions:

- 1359 • To provide an aerodynamically stable configuration during hypersonic and
1360 supersonic entry and descent into the H_2 -He ice-giant atmosphere while
1361 spin-stabilized along the probe's symmetry (rotation) axis;
- 1362 • To protect the descent vehicle from the extreme heating and thermo-
1363 mechanical loads of entry.
- 1364 • To accommodate the large deceleration loads from the descent vehicle
1365 during hypersonic entry.
- 1366 • To provide a safe, stable transition from hypersonic/supersonic to subsonic
1367 flight.

- 1368 • To safely separate the heatshield and backshell from the descent vehicle
1369 based on g -switch with timer backup, and transition the descent vehicle
1370 to descent science mode beneath the main parachute.

1371 One of the **primary challenges** for an ice-giant probe aeroshell is the heat-
1372 shield material and system that can withstand the extreme entry environment.
1373 Heritage carbon-phenolic thermal protection system used successfully for the
1374 Galileo and Pioneer-Venus entry aeroshell heatshields is no longer feasible due
1375 to raw material availability and also processing and manufacturing atrophy. An-
1376 other challenge is the limitations of ground test facilities needed to requalify a
1377 variant of the heritage carbon-phenolic or to develop and certify new material
1378 that will ensure survival and function as designed under the extreme entry con-
1379 ditions encountered at the ice giants. Currently, few facilities exist with the
1380 necessary capabilities to test thermal performance to the conditions likely to
1381 be encountered by an ice-giant probe, including stagnation heat-fluxes between
1382 (2.0 kW/cm^2 – 4.0 kW/cm^2) and stagnation pressure of 9–12 bars. At Uranus,
1383 relative entry velocities are $\sim 22 \text{ km/s}$, and the entry flight path angle deter-
1384 mines both the total heat-load and the mechanical (deceleration) load. Steeper
1385 entries result in lower total heat-load due to shorter time of flight to reach sub-
1386 sonic velocities but at a significantly higher deceleration (higher g -loading), and
1387 stagnation heat-flux and pressure. Shallower entries provide lower the g -loads
1388 and stagnation conditions, but increase the total heat-load. In addition, as
1389 mentioned previously – CRSC trajectories that provide shallower entry flight
1390 path angles typically result in the CRSC being much closer to the planet and
1391 therefore limit the time available for the probe telecom since the CRSC will pass
1392 through the probe antenna beam much more rapidly. All of these constraints,
1393 considerations, and trades need to be considered in the probe entry architecture
1394 design, and in selecting the **Thermal Protection System (TPS)** materials
1395 that can ensure a safe entry.

1396 *4.2.4. Enabling Technologies*

1397 The need for heat-shield to withstand the extreme entry conditions encoun-
1398 tered at the gas giant planet Saturn and the ice giant planets Uranus and Nep-
1399 tune is critical and currently being addressed by NASA. NASA is investing
1400 in the development of a new heat-shield material and system technology called
1401 Heat-shield for Extreme Entry Environment Technology (HEEET). HEEET will
1402 reach **Technology Readiness Level (TRL) 6** by 2018 (Milos et al., 2017).
1403 NASA has incentivized and offered HEEET to New Frontiers-4 entry probe
1404 mission proposals that are currently under competitive selection considerations.
1405 HEEET, an ablative TPS system that uses 3-D weaving to achieve both ro-
1406 bustness and mass efficiency at extreme entry conditions, has been tested at
1407 conditions that are relevant for Saturn and Uranus entry probe missions, as
1408 well as for missions to Venus and very high-speed sample return missions. Un-
1409 like other ablative TPS materials, HEEET is designed to withstand not only
1410 extreme entry with a pure carbon recession layer, but is also designed to mini-
1411 mize the heat transferred to the aeroshell structure by having an insulative layer
1412 that is much lower density and made of composite material to lower thermal
1413 conductivity. These distinct insulative and low thermal conductivity **are woven**
1414 **together integrally**, providing both robustness and efficiency. Compared to
1415 heritage carbon-phenolic system, HEEET is nearly 50% mass efficient (Ellerby
1416 et al., 2016).

1417 The probe aeroshell will need to be provided by NASA as it is developing
1418 and delivering an ablative TPS system to meet the mission needs for extreme
1419 entry environments. This allows shallower entry to be considered for entry into
1420 an ice giant, Saturn, or Venus.

1421 There are a number of flight-qualified materials available for backshell TPS.
1422 For example, in the backshell the conditions will be typically 2–5% of the peak
1423 stagnation condition on the heat-shield and hence PICA, another NASA devel-
1424 oped technology that has been flown at conditions ranging from (100 W/cm²
1425 to 1000 W/cm²) can be used. The aeroshell design including the 45° sphere-

1426 cone shape and size proposed for HERA (Mousis et al., 2016) will serve as the
1427 Uranus aeroshell and the shape is aerodynamically proven at Venus as well as
1428 at Jupiter, and will therefore meet the requirements at Uranus. The primary
1429 technology challenge for ice giant entry probe missions is the heatshield system
1430 and by using HEEET developed by NASA and using NASA expertise, minimal
1431 technology development is required.

1432 *4.3. Atmospheric Entry Probe System Design*

1433 *4.3.1. Overview*

1434 The probe comprises two major sub-elements: 1) the descent vehicle includ-
1435 ing parachutes will carry all the science instruments and support subsystems
1436 including telecommunications, power, control, and thermal into the atmosphere,
1437 and 2) the aeroshell that protects the descent **vehicle** during cruise, coast, and
1438 entry. The probe (Descent Vehicle + Aeroshell) is released from the CRSC, and
1439 arrives at the entry interface point following a long coast period. The Descent
1440 Vehicle (including the parachute system) carries the science payload into the
1441 deeper atmosphere. It is important to note that although the probe is released
1442 from the CRSC and is the vehicle that reaches the entry interface point, and
1443 the descent vehicle including parachutes descend into the ice-giant atmosphere,
1444 elements of the probe system including the probe release and separation mech-
1445 anism remain with the CRSC.

1446 Prior to entry, the probe coast timer (loaded prior to probe release) provides
1447 a wakeup call to initiate the entry power-on sequence for initial warmup, checks
1448 on instrument and subsystem health and status, and pre-entry calibrations.
1449 An ice-giant probe can arrive at the entry interface point with an-atmosphere
1450 relative velocity in the range of 22–26 km/s. Depending on an entry flight
1451 path angle, a probe at Uranus may experience peak heating of 2.5–3.5 kW/cm²,
1452 a peak entry deceleration pulse of 165–220 g’s, and a stagnation pressure of
1453 9–12 bars. At Neptune, the entry is even more severe with peak heating of
1454 4.3–10 kW/cm², peak deceleration of 125–455 g’s, and stagnation pressures
1455 of 7–25 bars (Elliott et al., 2017). The peak heating, total heat soak, and

1456 deceleration pulse will depend on the selected mission design including entry
1457 location (latitude/longitude), inertial heading, and flight path angle. The probe
1458 thermal protection system provides protection for the probe against the intense
1459 heating and thermal loads of entry, and an aft cover will protect the back of the
1460 probe from somewhat more benign radiative heating environment.

1461 During descent, the descent **vehicle** provides a thermally protected envi-
1462 ronment for the science instruments and probe subsystems, including power,
1463 operational command, timing, and control, and reliable telecommunications for
1464 returning probe science and engineering data. The probe avionics will collect,
1465 buffer, format, process (as necessary), and prepare all science and engineering
1466 data to be transmitted to the CRSC. The probe descent subsystem controls
1467 the probe descent rate and rotation necessary to achieve the mission science
1468 objectives.

1469 Although the atmospheres of the ice giants have been modeled, the ac-
1470 tual thermal, compositional, and dynamical structure beneath the cloud tops is
1471 largely unknown. Possible differences in composition and temperature/pressure
1472 structure between the atmosphere models and the measured atmosphere have
1473 the potential to adversely affect the performance of the probe relay telecom and
1474 must be accounted for in selection of communication link frequency. In particu-
1475 lar, the microwave opacity of the atmosphere is dependent on the abundances of
1476 trace species such as NH_3 , H_2S , and PH_3 , all microwave absorbers. In general,
1477 the opacity of these absorbers increases as the square of the frequency, and this
1478 drives the choice of telecom frequency to the lowest frequency reasonable, likely
1479 UHF. The final decision on frequency consequently affects the probe transmit
1480 antenna design, including structure, size, gain, and beam pattern/beamwidth.
1481 Decisions on antenna type and properties also depend on the probe descent sci-
1482 ence requirements, the time required to reach the target depth, and the CRSC
1483 overflight trajectory, including range, range rate, and angle. Throughout de-
1484 scent, the rotation of the planet and the CRSC overflight trajectory, along with
1485 atmospheric winds, waves, convection, and turbulence, aerodynamic buffeting,
1486 and descent vehicle spin and pendulum motion beneath the parachute will add

1487 Doppler contributions to the transmitted frequency that must be tracked by the
1488 CRSC receivers.

1489 The ice giants are significantly cooler than the gas giants. At 20 bars, the
1490 atmospheres of Jupiter and Saturn **reach** about 415 and 355 K, respectively,
1491 whereas at Uranus the 10-bar/20-bar temperatures are only about 180/225 K.
1492 However, at an altitude of 56 km above 1 bar, the tropopause is an extremely
1493 cold: 53 K as compared to the tropopause temperatures on Jupiter and Saturn
1494 of 110 and 85 K, respectively. Survival at the low tropospheric temperatures
1495 of the ice giants will require careful consideration be given to probe thermal-
1496 control design, and may dictate a sealed probe. At Uranus, the 10-bar level is
1497 located approximately 160 km beneath tropopause. If the Uranus science goal
1498 is to descend to 10 bars within one hour, an average descent speed of 45 m/s
1499 is required. With a scale height of about 33 km, a 160 km descent from the
1500 tropopause to 10-bars will pass through approximately 5 Uranian scale heights.

1501 *4.3.2. Entry Probe Power and Thermal Control*

1502 Following the release of the Descent Vehicle from the CRSC, the descent
1503 **vehicle** has four main functions:

- 1504 • To initiate the “wake up” sequence at the proper time prior to arrival at
1505 the entry interface point.
- 1506 • To safely house/protect, provide command and control authority for, pro-
1507 vide power for, and maintain a safe thermal environment for all the sub-
1508 systems and science instruments.
- 1509 • To collect, buffer as needed, and relay to the CRSC all required pre-entry,
1510 entry, and descent housekeeping, engineering, calibration, and science en-
1511 gineering data.
- 1512 • To control the descent speed and spin rate profile of the descent **vehicle**
1513 to satisfy science objectives and operational requirements.

1514 An ice giant mission will possibly include one or several Venus flybys at 0.7
1515 AU prior to a long cruise to the outer solar system at 20–30 AU. To provide
1516 a safe, stable thermal environment for probe subsystems and instruments over
1517 this range of heliocentric distances is not a trivial issue, and will require careful
1518 thermal design with care given to accounting for and understanding possible
1519 heat loss pathways. High-TRL insulating materials, models, and analysis and
1520 thermal management techniques will be used in the design program.

1521 Prior to arrival, the descent **vehicle** is released from the CRSC for a long
1522 coast to the entry interface point. During this coast period, the descent **vehicle**
1523 must maintain safe internal temperatures while providing power for the coast
1524 timer and the coast transmitter system needed to provide periodic health checks
1525 to the CRSC. While autonomous thermal control can be provided by batteries,
1526 an option for replacing the batteries is to add NASA or European Radioiso-
1527 tope Heater Units (RHUs). Since an ice giant flagship mission would almost
1528 certainly be nuclear powered, issues related to additional cost and launch ap-
1529 proval will have already been addressed. Use of RHUs would significantly reduce
1530 the battery complement with significant mass savings likely. Future technology
1531 developments with the potential to loosen some of the probe temperature re-
1532 quirements include the development of very low temperature (cryo) electronics.

1533 Once released from the CRSC, the probe will necessarily be entirely self-
1534 sufficient for mission operations, thermal control, and power management. As
1535 discussed, during coast, safe internal temperatures could be maintained with
1536 either RHUs or by way of primary batteries that provide electric power for
1537 small heaters as needed. Additional power is needed during coast for the coast
1538 timer as well as periodic health and status transmissions to the CRSC. During
1539 pre-entry and entry, the batteries support the probe wake-up, turn-on, sys-
1540 tem health checks and calibration, and entry acceleration measurements and
1541 data collection. Under the parachute, the batteries support all probe opera-
1542 tions including dual channel data transmission with an RF out of approximately
1543 10 watts/channel. Future technology developments may realize batteries with
1544 higher specific energies resulting in potential mass savings.

1545 *4.3.3. Data Relay*

1546 The probe telecommunication system comprises two redundant channels
1547 that, to improve isolation, will transmit orthogonal polarizations at slightly
1548 offset frequencies, and will operate in transmit mode only. Once released from
1549 the CRSC, the probe can no longer receive any commands. The telecom system
1550 is designed to ensure safe and reliable data return from the atmosphere as the
1551 probe descends under parachute. Driven by an ultrastable oscillator to ensure
1552 a stable link frequency for radio science measurements of atmospheric dynam-
1553 ics, the frequency of the probe to CRSC relay link is chosen primarily based
1554 on the microwave absorption properties of the atmosphere. The properties of
1555 the Jupiter system that drove the Galileo probe relay link frequency to higher
1556 frequencies (L-band) included the intense, pervasive synchrotron radiation from
1557 Jupiter’s powerful magnetosphere. This is not a significant issue at the ice gi-
1558 ants, and due to the increase in microwave opacity with higher frequencies, the
1559 relay link operates at UHF frequencies where atmospheric opacity is minimal
1560 **(T. Spilker, personal communication).**

1561 The probe data relay includes the transmission of pre-entry and entry engi-
1562 neering and instrument calibration data, measurements of entry accelerations,
1563 and all probe descent science acquired by the probe instrument payload. As
1564 compared to the single data rate systems utilized by the Galileo (Bright, 1984)
1565 and Huygens (Clausen et al., 2002) probes, an ice-giant probe may implement
1566 a variable data rate strategy to optimize the data return for the rate at which
1567 science data is collected and reflecting the probe descent profile and changing
1568 probe-CRSC geometry. The descent sequence and relay link strategy are se-
1569 lected to ensure that all collected science data be successfully transmitted prior
1570 to the probe reaching its target depth, nominally 10 bars.

1571 The probe low-gain antenna will be mounted on back of the probe to nomi-
1572 nally transmit in the $-z$ direction, opposite to the probe descent velocity vector,
1573 and will have a beamwidth large enough to support probe pendulum motion
1574 beneath the parachute while allowing for a large range of CRSC zenith angles

1575 throughout the probe descent. At UHF frequencies, a microwave patch antenna
1576 provides good performance with a peak gain of about 5–6 dB. The probe-relay
1577 signal will be received on the CRSC either through a dedicated probe relay
1578 antenna, or through the CRSC high gain antenna. Within the CRSC Relay
1579 Receiver, radio science data – frequency and signal strength - is recorded. Since
1580 the probe descent science, engineering, and housekeeping data volume is quite
1581 small, likely no more than several tens of Mbit, the CRSC is able to store multi-
1582 ple copies of each channel of probe data, with the option available for open loop
1583 recording of the probe signal. Following the end of the probe descent mission,
1584 the CRSC will return to Earth-point and downlink multiple copies of the stored
1585 probe data.

1586 *4.3.4. Carrier Relay Spacecraft*

1587 During the long cruise to the outer solar system, the CRSC provides struc-
1588 tural and thermal support, provides power for the probe, and supports periodic
1589 health checks, communications for probe science instrument software or calibra-
1590 tion changes, and other post-launch software configuration changes and mission
1591 sequence loading as might be required from launch to encounter. Upon final
1592 approach to Uranus, the CRSC supports a final probe health and configuration
1593 check, rotates to the probe release orientation, cuts cables and releases the probe
1594 for the probe cruise to the entry interface point. Following probe release, the
1595 CRSC may be tracked for a period of time, preferably several days, to character-
1596 ize the probe release dynamics and improve reconstructions of the probe coast
1597 trajectory and entry interface location. An important release sequence option
1598 would be to image the probe following release for optical navigation character-
1599 ization of the release trajectory. Following probe release and once the CRSC
1600 tracking period is over, the CRSC is deflected from the planet-impact trajec-
1601 tory required for probe targeting to a trajectory that will properly position the
1602 CRSC for receiving the probe descent telecommunications. During coast, the
1603 probe will periodically transmit health status reports to the CRSC. Addition-
1604 ally, the CRSC will conduct a planet-imaging campaign to characterize the time

1605 evolution of the atmosphere, weather, and clouds at the probe entry site, as well
1606 as to provide global context of the entry site.

1607 Prior to the initiation of the probe descent sequence, the CRSC will rotate
1608 to the attitude required for the probe relay receive antenna to view the probe
1609 entry/descent location and will prepare to receive both channels of the probe
1610 science telecommunications. The CRSC relay-receive antenna could either be a
1611 dedicated relay antenna similar to that used on the Galileo orbiter, or the CRSC
1612 could use the spacecraft high gain antenna similar to the Cassini-Huygens relay
1613 telecommunications configuration. To account for changes in the CRSC antenna
1614 pointing due to the trajectory of the CRSC, the rotation of the planet, and the
1615 possible effect of winds on the probe descent location, the option for periodic
1616 repointing of the CRSC relay receive antenna must be accommodated.

1617 Following receipt of the probe transmission, multiple copies of the entire
1618 probe science data set are stored in CRSC memory prior to Earth downlink.
1619 It is expected that the memory storage requirements are easily met with a few
1620 hundred Mbit of storage capacity. Once the probe mission is completed and
1621 all probe data have been relayed to the CRSC, the CRSC will rotate to point
1622 the HGA at Earth and, to ensure complete transfer of the entire data set, the
1623 CRSC will initiate the first of multiple downlinks of the probe data set.

1624 *4.4. NASA/ESA Collaboration*

1625 The participation of and contributions from NASA are essential for an ESA-
1626 led entry probe. The ESA Uranus/Neptune probe mission will begin its flight
1627 phase as an element of a NASA Uranus or Neptune mission (likely a NASA
1628 Flagship mission) launch to place both the NASA spacecraft, which functions
1629 also as the probe's CRSC, and the probe on a transfer trajectory to Uranus or
1630 Neptune. The thermal protection necessary to protect the probe during high
1631 speed entry is still to be determined, but it is likely to be the HEEET (Heat
1632 Shield for Extreme Entry Environment Technology) material currently being
1633 developed by NASA. Additionally, NASA may contribute both instruments with
1634 Pioneer, Galileo, and Huygens heritage, as well as provide the participation of

1635 significant expertise from many engineers and scientists with experience with
1636 previous solar system entry probe missions.

1637 5. Possible Probe Model Payload

1638 Table 4 presents a suite of scientific instruments that can address the scien-
1639 tific requirements discussed in previous sections. This list of instruments should
1640 be considered as an example of scientific payload that we might wish to see on-
1641 board. Ultimately, the payload of a Uranus or Neptune probe would be defined
1642 from a detailed mass, power and design trades, but should seek to address the
1643 majority of the scientific goals outlined in Sections 2 and 3.

1644 5.1. Mass Spectrometry

1645 The chemical and isotopic composition of Uranus' and Neptune's atmo-
1646 spheres, and their variabilities, will be measured by mass spectrometry. The
1647 scientific objectives relevant to the planets' formation and the origin of the
1648 solar system requires *in situ* measurements of the chemical composition and iso-
1649 tope abundances in the atmosphere, such as H, C, N, S, P, Ge, As, noble gases
1650 He, Ne, Ar, Kr, and Xe, and the isotopes D/H, $^{13}\text{C}/^{12}\text{C}$, $^{15}\text{N}/^{14}\text{N}$, $^{17}\text{O}/^{16}\text{O}$,
1651 $^{18}\text{O}/^{16}\text{O}$, $^3\text{He}/^4\text{He}$, $^{20}\text{Ne}/^{22}\text{Ne}$, $^{38}\text{Ar}/^{36}\text{Ar}$, $^{36}\text{Ar}/^{40}\text{Ar}$, and those of Kr and Xe,
1652 of which very little is known at present (see Sections 2 and 3). At Jupiter, the
1653 Galileo Probe Mass Spectrometer (GPMS) experiment (Niemann et al., 1992)
1654 was designed to measure the chemical and isotopic composition of Jupiter's at-
1655 mosphere in the pressure range from 0.15 to 20 bar by *in situ* sampling of the
1656 ambient atmospheric gas. The GPMS consisted of a gas-sampling system that
1657 was connected to a quadrupole mass spectrometer. The gas sampling system
1658 also had two sample enrichment cells, one for enrichments of hydrocarbons by
1659 a factor 100–500, and one for noble gas analysis cell with an enrichment factor
1660 of about 10. The abundance of the minor noble gases Ne, Ar, Kr, and Xe were
1661 measured by using the enrichment cell on the Galileo mission, but the sensitiv-
1662 ity was too low to derive isotope abundances with good accuracy (Niemann et

1663 al., 1996). From GPMS measurements the Jupiter He/H₂ ratio was determined
1664 as 0.1567 ± 0.006 . To improve the accuracy of the measurement of the He/H₂
1665 ratio and isotopic ratios by mass spectrometry the use of reference gases will
1666 be necessary. The ROSINA experiment on the Rosetta mission carried a gas
1667 calibration unit for each mass spectrometer (Balsiger et al., 2007). Similarly,
1668 the SAM experiment on the Curiosity rover can use either a gas sample from
1669 its on-board calibration cell or utilise one of the six individual metal calibration
1670 cups on the sample manipulation system (Mahaffy et al., 2012).

1671 A major consideration for the mass-spectrometric analysis is how to dis-
1672 tinguish between different molecular species with the same nominal mass, e.g.,
1673 N₂, CO, and C₂H₄, which all have nominal mass 28, but differ in their actual
1674 mass by about 0.01 amu. There are two ways to address this problem, one
1675 is high-resolution mass spectrometry with sufficient mass resolution to resolve
1676 these isobaric interferences for the molecules of interest (i.e., $m/\Delta m = 3,000$ for
1677 the given example), and the other way is chemical pre-separation of the sample
1678 followed by lower resolution mass spectrometry.

1679 5.1.1. High-Resolution Mass Spectrometry

1680 High-resolution mass spectrometry is defined by the capability of the mass
1681 spectrometer to resolve isobaric interferences. Usually that means mass resolu-
1682 tion of 10,000 and larger, depending on the nature of the isobaric interference.
1683 Probably the first high-resolution mass spectrometer in space is the ROSINA ex-
1684 periment on the Rosetta mission (Balsiger et al., 2007). ROSINA has a Double-
1685 Focussing Mass Spectrometer (DFMS), see Figure 7, with a mass resolution of
1686 about $m/\Delta m = 9,000$ at 50 percent peak height (corresponding to $m/\Delta m =$
1687 $3,000$ at 1% peak height), Reflectron-Time-of-flight (RTOF) instrument with a
1688 mass resolution of about $m/\Delta m = 5,000$ at 50% peak height (Scherer et al.,
1689 2006), and a pressure gauge. Determination of isotope ratios with an accuracy
1690 at the percent-level has been accomplished for gases in the cometary coma for
1691 H/D (Altwegg et al., 2015), for ¹²C/¹³C and ¹⁶O/¹⁸O (Hässig et al., 2017), for
1692 ³⁵Cl/³⁷Cl and ⁷⁹Br/⁸¹Br (Dhooghe et al., 2017), for the silicon isotopes (Rubin

1693 et al., 2017), $^{36}\text{Ar}/^{38}\text{Ar}$ (Balsiger et al., 2015), and Xe isotopes (Marty et al.,
1694 2017).

1695 A time-of-flight instrument with even more mass resolution has been devel-
1696 oped for possible application in Europa's atmosphere, which uses a multi-pass
1697 time-of flight configuration (Brockwell et al., 2016). Accomplished mass resolu-
1698 tions are $m/\Delta m = 40,000$ at 50% peak height and 20,000 at 10% peak height.
1699 An alternative multi-pass time-of-flight instrument has been developed by Oku-
1700 mura et al. (2004), which uses electric sectors instead of ion mirrors for time
1701 and space focussing, which allows for high mass resolution in a compact design.
1702 Mass resolutions up to $m/\Delta m = 350,000$ have been reported (Toyoda et al.,
1703 2003). Later, a more compact version of this instrument has been developed
1704 (Shimma et al., 2010, Nagao et al., 2014).

1705 Recently, a new type of mass spectrometer, the Orbitrap mass spectrometer,
1706 was introduced (Makarov, 2000, Hu et al., 2005), which uses ion confinement
1707 in a harmonic electrostatic potential. The Orbitrap mass spectrometer is a
1708 Fourier-Transform type mass spectrometer, and it allows for very high mass
1709 resolutions in a compact package. Resolving powers above 1,000,000 have been
1710 accomplished with laboratory instruments (Denisov et al., 2012). For example,
1711 using an Orbitrap mass spectrometer for laboratory studies of chemical pro-
1712 cesses in Titan's atmosphere, mass resolutions of $m/\Delta m = 100,000$ have been
1713 accomplished up to $m/z = 400$ (Hörst et al., 2012), and $m/\Delta m = 190,000$ at
1714 50% peak height and $m/z = 56$ in a prototype instrument for the JUICE mission
1715 (Briois et al., 2013, 2016).

1716 5.1.2. Low-Resolution Mass Spectrometry with Chemical Pre-processing

1717 The alternative approach to high-resolution mass spectrometry, is to use a
1718 simpler low-resolution mass spectrometer together with a chemical processing of
1719 the sample to separate or eliminate isobaric interferences. One established way
1720 used in space instrumentation is to use chromatographic columns with dedicated
1721 chemical specificity for a separation of chemical substances. Also enrichments
1722 cells to selectively collect a group of chemical species have been used.

1723 The Gas-Chromatograph Mass Spectrometer (GCMS) of the Huygens probe
1724 is a good example of such an instrument (Niemann et al., 2002, 2005, 2010).
1725 The Huygens probe GCMS has three chromatographic columns, one column
1726 for separation of CO and N₂ and other stable gases, the second column for
1727 separation of nitriles and other organics with up to three carbon atoms, and the
1728 third column for the separation of C₃ through C₈ saturated and unsaturated
1729 hydrocarbons and nitriles of up to C₄. The GCMS was also equipped with a
1730 chemical scrubber cell for noble gas analysis and a sample enrichment cell for
1731 selective measurement of high boiling point carbon containing constituents. A
1732 quadrupole mass spectrometer was used for mass analysis with a mass range
1733 from 2 to 141 u/e, which is able to measure isotope ratios with an accuracy of
1734 1%.

1735 Examples of newer GCMS instrumentation are the Ptolemy instrument on
1736 the Rosetta lander for the measurement of stable isotopes of key elements
1737 (Wright et al., 2007), which uses an ion trap mass spectrometer, the COSAC
1738 instrument also on the Rosetta lander for the characterisation of surface and
1739 subsurface samples (Goesmann et al., 2007), which uses a time-of-flight mass
1740 spectrometer, the GCMS instrument for the Luna-Resource lander (Hofer et
1741 al., 2015), which also uses a time-of-flight mass spectrometer, and the SAM
1742 experiment on the Curiosity rover (Mahaffy et al., 2012), which uses a classical
1743 quadrupole mass spectrometer.

1744 To increase the sensitivity for a range of chemical compounds (e.g. hydrocar-
1745 bons) dedicated enrichment cells were used, as discussed above for the GPMS
1746 experiment. A novel and promising enrichment cell uses the cryotrapping tech-
1747 nique, which has a long history in the laboratory. The use of cryotrapping
1748 increases the instruments sensitivity by up to 10,000 times the ambient perfor-
1749 mance (Brockwell et al., 2016), and would allow for the detection of noble gases
1750 at abundances as low as 0.02 ppb (Waite et al., 2014).

1751 *5.1.3. Summary of Mass Spectrometry*

1752 So far in most space missions the chemical pre-separation was the technique
1753 used to overcome isobaric interferences in the mass spectra, with the exception
1754 of the mass spectrometer experiment ROSINA on the Rosetta orbiter. Chemi-
1755 cal pre-separation works well, but by choosing chromatographic columns with a
1756 certain chemical specificity one makes a pre-selection of the species to be inves-
1757 tigated in detail. This is a limitation when exploring an object of which little
1758 is known. Also, gas chromatographic systems with several columns are rather
1759 complex systems, both to build and to operate (see the SAM instrument as a
1760 state-of-the art example of this technique; [Mahaffy et al. \(2012\)](#)).

1761 In recent years there has been a significant development of compact mass
1762 spectrometers that offer high mass resolution. Thus, solving the problem of
1763 isobaric interferences in the mass spectra by mass resolution can be addressed by
1764 mass spectrometry alone and one should seriously consider using high-resolution
1765 mass spectrometry for a future mission to probe planetary atmospheres. After
1766 all, no a priori knowledge of the chemical composition has to be assumed in this
1767 case. In addition, with modern time-of-flight mass spectrometers mass ranges
1768 beyond 1000 u/e are not a problem at all, which, for example, would have been
1769 useful to investigate Titan's atmosphere. Nevertheless, enrichments of certain
1770 chemical groups (e.g., hydrocarbons or noble gases) should still be considered
1771 even in combination with high-resolution mass spectrometry to maximise the
1772 science return.

1773 *5.1.4. Tunable Laser System*

1774 A Tunable Laser Spectrometer (TLS) ([Durry et al., 2002](#)) can be employed
1775 as part of a Gas-Chromatograph system to measure the isotopic ratios to a high
1776 accuracy of specific molecules, e.g. H₂O, NH₃, CH₄, CO₂ and others. TLS
1777 employs ultra-high spectral resolution (0.0005 cm⁻¹) tunable laser absorption
1778 spectroscopy in the near infra-red (IR) to mid-IR spectral region. TLS is a
1779 simple technique that for small mass and volume can produce remarkable sen-
1780 sitivities at the sub-ppb level for gas detection. Species abundances can be

1781 measured with accuracies of a few %. With a TLS system one can derive iso-
1782 tope abundances with accuracies of about 0.1% for the isotopic ratios of D/H,
1783 $^{13}\text{C}/^{12}\text{C}$, $^{18}\text{O}/^{16}\text{O}$, and $^{17}\text{O}/^{16}\text{O}$.

1784 For example, TLS was developed for application in the Mars atmosphere
1785 (Le Barbu et al., 2004), within the ExoMars mission; a recent implementation
1786 of a TLS system was for the Phobos Grunt mission (Durry et al., 2010), and
1787 another TLS is part of the SAM instrument on the Curiosity Rover (Webster
1788 and Mahaffy, 2011), which was used to measure the isotopic ratios of D/H and
1789 of $^{18}\text{O}/^{16}\text{O}$ in water and $^{13}\text{C}/^{12}\text{C}$, $^{18}\text{O}/^{16}\text{O}$, $^{17}\text{O}/^{16}\text{O}$, and $^{13}\text{C}^{18}\text{O}/^{12}\text{C}^{16}\text{O}$ in
1790 carbon dioxide in the Martian atmosphere (Webster et al., 2013).

1791 5.2. Helium Abundance Detector

1792 The Helium Abundance Detector (HAD), as it was used on the Galileo mis-
1793 sion (von Zahn and Hunten, 1992), measures the refractive index of the atmo-
1794 sphere in the pressure range of 2–10 bar. The refractive index is a function of
1795 the composition of the sampled gas, and since the jovian atmosphere consists
1796 of mostly of H_2 and He, to more than 99.5%, the refractive index is a direct
1797 measure of the He/ H_2 ratio. The refractive index can be measured by any two-
1798 beam interferometer, where one beam passes through a reference gas and the
1799 other beam through atmospheric gas. The difference in the optical path gives
1800 the difference in refractive index between the reference and atmospheric gas.
1801 For the Galileo mission, a Jamin-Mascart interferometer was used, because of
1802 its simple and compact design, with an expected accuracy of the He/ H_2 ratio of
1803 ± 0.0015 . The accomplished measurement of the He mole fraction gave $0.1350 \pm$
1804 0.0027 (von Zahn et al., 1998), with a somewhat lower accuracy than expected,
1805 but still better than is possible by a mass spectrometric measurement.

1806 5.3. Atmospheric Structure Instrument

1807 The Atmospheric Structure Instrument (ASI) of the entry probe will make *in*
1808 *situ* measurements during the entry and descent into the atmosphere of Uranus
1809 and Neptune in order to investigate the atmospheric structure, dynamics and

1810 electricity. The scientific objectives for ASI are to determine the atmospheric
1811 profiles of density, pressure and temperature along the probe trajectory and the
1812 investigation of the atmospheric electricity (e.g. lightning) by *in situ* measure-
1813 ments. The ASI will use the mean molecular weight as measured by the mass
1814 spectrometer to calculate the profile of atmospheric density.

1815 The ASI benefits from the strong heritage of the Huygens ASI experiment of
1816 the Cassini/Huygens mission (Fulchignoni et al., 2002) and Galileo, and Pioneer
1817 Venus ASI instruments (Seiff and Knight, 1992, Seiff et al., 1980). The key *in*
1818 *situ* measurements will be entry accelerations from which the density of the up-
1819 per atmosphere (above parachute deployment) can be found, and from this the
1820 pressure and temperature profiles can be retrieved. During parachute descent,
1821 the ASI will perform direct temperature and pressure sampling (Fulchignoni et
1822 al., 2005, Seiff et al., 1998). Once the probe heat shield is jettisoned, direct mea-
1823 surements of pressure, temperature and electrical properties will be performed.
1824 During descent, the pressure, temperature, and and electric property sensors
1825 will be placed beyond the probe boundary layer to have unimpeded access to
1826 the atmospheric flow.

1827 *In situ* measurements are essential for the investigation of the atmospheric
1828 structure and dynamics. The data provided by the ASI will help constrain
1829 and validate models of atmospheric thermal, electrical, and dynamical struc-
1830 ture. The ASI measurement of the atmospheric pressure and temperature will
1831 constrain the stability of the atmosphere, providing an important context for
1832 understanding the atmospheric dynamics and mixing and the energy and cloud
1833 structure of the atmosphere. The determination of the lapse rate can help iden-
1834 tify locations of condensation and eventually clouds, and to distinguish between
1835 saturated and unsaturated, stable and conditionally stable regions. The possi-
1836 ble variations atmospheric stability and detection of atmospheric stratification
1837 are strongly correlated with the presence of winds, thermal tides, waves, and
1838 turbulence within the atmosphere.

1839 The ASI will measure properties of Uranus and Neptune's atmospheric elec-
1840 tricity by determining the conductivity profile of the troposphere, and detecting

1841 the atmospheric DC electric field. These measurements provide indirect infor-
1842 mation about galactic cosmic ray ionization, aerosol charging inside and outside
1843 of clouds, properties of potential Schumann resonances, and allow for detection
1844 of possible electrical discharges (i.e. lightning). ASI could measure the unknown
1845 lightning spectra in the frequency range of ~ 1 –200 kHz below the ionosphere,
1846 and will obtain burst waveforms with different temporal resolutions and dura-
1847 tions in order to detect and characterize lightning activity in ice giants. Refining
1848 the location of lightning flashes, whether determined optically from an orbiter
1849 or *in situ* from a probe, and correlating the detected lightning with the obser-
1850 vations of weather systems may provide powerful constraints on the location of
1851 deep storms and weather systems and the depth, location, and density of clouds.

1852 5.4. Doppler-Wind Experiment

1853 The probe Uranus/Neptune Radio Science Experiment (RSE) will include
1854 a Doppler Wind Experiment (DWE) dedicated to the measurement of the ver-
1855 tical profile of the zonal (east-west) winds along the probe descent path, and
1856 a measurement of the integrated atmospheric microwave absorption measure-
1857 ments along the probe-relay atmospheric raypath. The absorption measurement
1858 will indirectly provide a measurement of atmospheric abundance of ammonia.
1859 This technique was used by the Galileo probe to constrain the Jovian atmo-
1860 spheric NH_3 profile, strongly complementing measurements of the atmospheric
1861 composition by the probe Mass Spectrometer (Folkner et al., 1998).

1862 The primary objectives of the probe Doppler Wind Experiment is to use
1863 the probe-CRSC radio subsystem (with elements mounted on both the probe
1864 and the Carrier) to measure the altitude profile of zonal winds along the probe
1865 descent path under the assumption that the probe in terminal descent beneath
1866 the parachute will accurately trace the zonal wind profile. In addition to the
1867 vertical profile of the zonal winds, the DWE will also be sensitive to atmospheric
1868 turbulence, aerodynamic buffeting, and atmospheric convection and waves that
1869 disrupt the probe descent speed. Key to the Doppler wind measurement is an
1870 accurate knowledge of the reconstructed probe location at the beginning of de-

1871 scent, the reconstructed probe descent speed with respect to time/altitude, and
1872 the reconstructed Carrier position and velocity throughout the period of the
1873 relay link. The probe entry trajectory reconstruction from the entry interface
1874 point to the location of parachute deployment depends on measured accelera-
1875 tions during entry, and the descent profile is reconstructed from measurements
1876 of pressure and temperature by the Atmospheric Structure Instrument. From
1877 the known positions and velocities of the descent probe and Carrier, a profile
1878 of the expected relay link frequency can be created, and when differenced with
1879 the measured frequencies, a profile of Doppler residuals results. Inversion of the
1880 Doppler residual profile using an algorithm similar to the Galileo probe Doppler
1881 Wind measurement (Atkinson et al., 1997, 1998). To generate the stable probe
1882 relay signal, the probe will carry a quartz crystal ultrastable oscillator (USO)
1883 within the relay transmitter, with an identical USO in the relay receiver on the
1884 Carrier spacecraft.

1885 Secondary objectives of the DWE include the analysis of Doppler modula-
1886 tions and frequency residuals to detect, locate, and characterize regions of at-
1887 mospheric turbulence, convection, wind shear, and to provide evidence for and
1888 characterize atmospheric waves. Analysis of the relay link signal strength mea-
1889 surements be used to study the effect of refractive-index fluctuations in Uranus's
1890 atmosphere including scintillations and atmospheric turbulence (Atkinson et al.,
1891 1998, Folkner et al., 1998).

1892 5.5. Nephelometer

1893 A nephelometer will be used to characterize the atmospheric clouds, aerosols
1894 and condensates. Measurement of scattered visible light within the atmosphere
1895 is a powerful tool to retrieve number density and size distribution of liquid and
1896 solid particles, related to their formation process, and to understand the over-
1897 all character of the atmospheric aerosols based on their refractive index (liquid
1898 particles, iced particles, solid particles from transparent to strongly absorbing,
1899 etc.). In general, counting instruments are performing their measurements at a
1900 given scattering angle, typically around 90° , considering the scattering prop-

1901 erties of the particles that cross a laser beam. The particle concentrations are
1902 retrieved in several size classes typically between few tenths of μm to several
1903 tens of μm (Grimm et al., 2009). The scattered light is dependent both on the
1904 size of the particles and the complex refractive index. To accurately retrieve
1905 the size distribution, **the nephelometer must be calibrated, assuming the**
1906 **nature of particles is known.** Typically, carbonaceous particles could be tens
1907 of times less luminous than liquid droplets. On the other hand, measurements at
1908 small scattering angle below 20° are less dependent on the refractive index and
1909 can be used for the determining number densities of the aerosols independent
1910 of their nature (Renard et al., 2010, Lurton et al., 2014).

1911 The retrieval of the full scattering function by a nephelometer that simul-
1912 taneously records scattered light at different angles by all the particles in the
1913 field of view can provide a good estimate of the nature of the particles, particu-
1914 larly refractive index. The size distribution (expected to be monomodal) can be
1915 retrieved using Mie scattering theory or more sophisticated models for regular
1916 particles having symmetries (Verhaege et al., 2009). Ray tracing method can
1917 also be used for large particles as ice crystal (Shcherbakov et al., 2006). It is
1918 also possible to distinguish between liquid droplets and iced particles, as done
1919 in the Earth atmosphere (Gayet et al., 1997). In the case of irregular shaped
1920 particles, the observed scattering function can be compared to reference mea-
1921 surements obtained in laboratory (Renard et al., 2002, Volten et al., 2006) to
1922 identify their nature; the laboratory scattering functions were obtained for a
1923 cloud of levitating particles with well-known size distribution.

1924 Due to the low temperature, ice particles of methane and other hydrocarbons
1925 are present in the atmospheres of Uranus and Neptune (Sánchez-Lavega et al.,
1926 2004, Sánchez-Lavega, 2011). It is then necessary to be able to distinguish be-
1927 tween solid and liquid particles when performing light-scattering measurements
1928 inside these atmospheres. It is proposed to use the “LOAC (Light Optical
1929 Aerosol Counter)” concept, already used in routine for *in situ* measurements
1930 inside the Earth atmosphere (Renard et al., 2016a,b), to retrieve both the size
1931 distribution in 20 size classes and the scattering function to identify the nature

1932 of the particles. At present, LOAC performs measurement at two scattering
1933 angles, around 15° and 60° . Scattering at the smaller angle is used to re-
1934 trieve the size distribution, and scattering at the larger angle combined with
1935 smaller angle scattering provides an estimate of the main nature of the aerosols,
1936 whether liquid droplets, mineral particles, carbonaceous particles, ice particles,
1937 etc. The nature estimate is based on a comparison with laboratory data of the
1938 size evolution of the 60° -angle measurements. To be able to estimate more
1939 accurately the nature of the particles for all the size classes in the $0.1\text{--}100\ \mu\text{m}$
1940 size range, measurement must be conducted simultaneously by a ring of 10 to
1941 15 detectors in the $10^\circ\text{--}170^\circ$ scattering angle range. These measurements can
1942 be compared to theoretical calculation for droplets and ices, but also to labo-
1943 ratory measurements in case of more complex particles both in shape and in
1944 composition.

1945 LOAC used in Earth atmosphere has a pump to inject the particles inside
1946 the optical chamber and the laser beam. In case of an atmospheric descent
1947 probe, a collecting inlet can be mounted in front of the pump, to inject directly
1948 the particles inside the chamber without the pumping system. A dedicated fast
1949 electronic will be developed to be able to record accurately the light pulse
1950 when particles will cross one by one a thin laser beam at a speed of several tens
1951 of m/s, and to be able to detect up to 1000 particles per cm^3 .

1952 *5.6. Net Energy Flux Radiometer*

1953 *5.6.1. Scientific Impetus*

1954 Ice giant meteorology regimes depend on internal heat flux levels. Down-
1955 welling solar insolation and upwelling thermal energy from the planetary inte-
1956 rior can have altitude and location dependent variations. Such radiative-energy
1957 differences cause atmospheric heating and cooling, and result in buoyancy differ-
1958 ences that are the primary driving force for Uranus and Neptune's atmospheric
1959 motions (Allison et al., 1991, Bishop et al., 1995). The three-dimensional,
1960 planetary-scale circulation pattern, as well as smaller-scale storms and con-
1961 vection, are the primary mechanisms for energy and mass transport in the ice

1962 giant atmospheres, and are important for understanding planetary structure and
 1963 evolution (Lissauer, 2005, Dodson-Robinson and Bodenheimer, 2010, Turrini et
 1964 al., 2014). These processes couple different vertical regions of the atmosphere,
 1965 and must be understood to infer properties of the deeper atmosphere and cloud
 1966 decks (see Figure 5). It is not known in detail how the energy inputs to the at-
 1967 mosphere interact to create the planetary-scale patterns seen on these ice giants
 1968 (Hofstadter et al., 2017). Knowledge of net vertical energy fluxes would supply
 1969 critical information to improve our understanding of atmospheric dynamics.

1970 A Net Flux Radiometer (NFR) will contribute to this understanding by
 1971 measuring the up- and down-welling radiation flux, F , as a function of altitude.
 1972 The net flux, the difference between upward and downward radiative power
 1973 per unit area crossing a horizontal surface per unit area is directly related to
 1974 the radiative heating or cooling of the local atmosphere. At any point in the
 1975 atmosphere, radiative power absorbed per unit volume is given by the vertical
 1976 derivative of net flux (dF/dz) in the plane-parallel approximation where the flux
 1977 is horizontally uniform; the corresponding heating rate is then $(dF/dz)/(\rho C_p)$,
 1978 where ρ is the local atmospheric density and C_p is the local atmospheric specific
 1979 heat at constant pressure.

1980 5.6.2. Measuring Net Energy Flux

1981 Three NFR instruments have flown to planets in the past, namely the large
 1982 probe infrared radiometer (Boese et al., 1980) on Pioneer-Venus large probe,
 1983 small probe NFR on Pioneer-Venus small probe (Colin and Hunten, 1977), and
 1984 the NFR on the jovian Galileo probe (Sromovsky et al., 1992) for *in situ* mea-
 1985 surements within the venusian and jovian atmospheres, respectively. These
 1986 instruments were designed to measure the downward and upward radiation flux
 1987 within their respective atmospheres as the probe descended by parachute. The
 1988 Galileo NFR encountered rapid temperature excursions during the drop (Sro-
 1989 movsky et al., 1998), a fact that influences the design of the next-generation
 1990 NFR. The Galileo NFR also measured the vertical profile of upward and down-
 1991 ward radiation fluxes on Jupiter from about 0.44 to 14 bars (Sromovsky et al.,

1992 1998). Radiation was measured in five broad spectral bands, 0.3–3.5 μm (total
 1993 solar radiation), 0.6–3.5 μm (total solar radiation weighted to the methane ab-
 1994 sorption region), 3–500 μm (deposition and loss of thermal radiation), 3.5–5.8
 1995 μm (window region with low gas phase absorption), and 14–35 μm (hydro-
 1996 gen dominated). Galileo NFR data provided signatures of ammonia (NH_3) ice
 1997 clouds and ammonium hydrosulfide (NH_4SH) clouds (Sromovsky et al., 1998).
 1998 The water fraction was found to be much lower than solar and no water clouds
 1999 were identified.

2000 **For Uranus and Neptune, NFR measurements should elucidate the**
 2001 **thermal structure from ~ 0.1 bar (near the tropopause which coincides**
 2002 **with the temperature minimum) to well beyond 10 bar, ideally to at**
 2003 **least 50 bar (see Figure 5), the uppermost cloud layer at ~ 1 bar level is made**
 2004 **up of CH_4 ice (revealed by Voyager-2 radio occultation observations). The base**
 2005 **of the water-ice cloud for solar O/H is expected to be at ~ 200 – 300 -**
 2006 **bar level, whereas NH_4SH and NH_3 clouds form at pressures lower**
 2007 **than ~ 50 bar (Atreya and Wong, 2004).** So far, only an upper limit is
 2008 known for Uranus’ heat flow based on Voyager 2 (Pearl et al., 1990). *In situ*
 2009 probe measurements will help to define sources and sinks of planetary radia-
 2010 tion, regions of solar energy deposition, and provide constraints on atmospheric
 2011 composition and cloud layers. Ultimately, an NFR in concert with a suite of
 2012 additional science instruments (mass spectrometer, atmospheric structure suite,
 2013 nephelometer, radio science /Doppler wind instrument, *etc.*) will constrain the
 2014 processes responsible for the formation of these ice giants.

2015 5.6.3. Basic Design Considerations

2016 Since the days of the Galileo probe NFR, there have been substantial ad-
 2017 vancements in optical windows and filters, uncooled thermal detectors, and ra-
 2018 diation hard electronic readout technologies that have enabled the development
 2019 of a more capable NFR. The Saturn probe prototype NFR (see Table 6 and
 2020 Figures 8 and 9) developed at NASA Goddard Space Flight Center (Aslam et
 2021 al., 2015) is designed to measure radiation flux in a 5° field-of-view based on the

2022 planetary scale height, in two spectral channels (i.e., a solar channel between
2023 0.25 to 5 μm and a thermal channel between 4 to 50 μm). The radiometer is
2024 capable of viewing five distinct look angles ($\pm 80^\circ$, $\pm 45^\circ$, and 0°) into the at-
2025 mosphere during the probe descent. Non-imaging Winston cones with window
2026 and bandpass filter combinations define the spectral channels with a 5° Field-
2027 Of-View (FOV); if necessary and appropriate relaxing the FOV to $>5^\circ$ is easily
2028 implemented, with the added benefit of a smaller focal plane package due to
2029 smaller Winston cones. Uncooled single-pixel thermopile detectors are used in
2030 each spectral channel and are read out using a custom designed Multi-Channel
2031 Digitizer (MCD) Application Specific Integrated Circuit (ASIC) (Aslam et al.,
2032 2012, Quilligan et al., 2015, 2014).

2033 For applications to Uranus or Neptune, the solar channel would be essentially
2034 preserved, and the thermal channel range extended to capture the majority of
2035 the thermal radiation, as the planetary Planck function peak moves to longer
2036 wavelengths with colder temperatures and addition of several judiciously cho-
2037 sen and optimized spectral channels (up to seven, with hexagonal close packing
2038 of Winston cones, see Sec. 5.6.4) to capture radiation flux of gases and par-
2039 ticulates and thus provide important independent constraints of atmospheric
2040 composition, cloud structure, and scattering processes.

2041 5.6.4. *Optimal Filter Channels*

2042 Voyager-2 radio occultation data (Lindal et al., 1987) from Uranus for exam-
2043 ple shows that C is enhanced by more than an order of magnitude with respect
2044 to solar abundance. If the mixing ratios of O, S, N, and C are in relative solar
2045 abundance then thermochemical equilibrium models (Atreya and Wong, 2004,
2046 West et al., 1990), predict that a water cloud will form at deep levels (>100
2047 bar), an NH_4SH cloud will form at a few tens of bars pressure, NH_3 ice will
2048 condense near the 10-bar level, and CH_4 ice will condense near the 1 bar level.
2049 To date the gross features of the upper atmosphere as predicted by these models
2050 remain valid but fundamental questions still remain i.e., what levels of solubil-
2051 ity of NH_3 and CH_4 will lead to appreciable depletions in the mixing ratios

2052 of these constituents above the water cloud? Also it is not clear that the rel-
2053 ative mixing ratios of O, S, N and C are close to solar ratios (Cavalié et al.,
2054 2017), since almost all of the enhanced abundances of these elements are due
2055 to preferential accumulation of planetesimals (as opposed to gas) by the giant
2056 planets and to the partial dissolution of these solid bodies in the forming plan-
2057 ets' gaseous envelopes (Pollack et al., 1986). An enhancement of the S to N
2058 ratio could deplete NH_3 in the upper atmosphere by promoting NH_4SH to the
2059 point where no NH_3 clouds form, but rather an H_2S ice cloud may form near
2060 the 100 K temperature level where the pressure is about 2 bar. To address these
2061 important science questions, contribution functions have been calculated (i.e.,
2062 the altitude sensitivity of the planet's emergent radiance) for specific infrared
2063 channels to demonstrate that an optimal set of filters will be able to probe the
2064 methane cloud opacity and tropospheric temperatures from the cloud tops to
2065 the tropopause. Seven NFR baseline spectral filter channels, (see Table 5), have
2066 been identified, suitable for both Uranus and Neptune, to probe tropospheric
2067 aerosol opacity in the cloud-forming region using dedicated channels near 5 and
2068 $8.6 \mu\text{m}$, plus far-infrared channels long ward of $50 \mu\text{m}$ and in the visible.

2069 NFR measurements in concert with mass spectrometry of a host of chemi-
2070 cal species from cloud-forming volatiles and disequilibrium species tracing tro-
2071 pospheric dynamics will ultimately aid in understanding middle atmospheric
2072 chemistry and circulation and cloud-condensation microphysics of the cloud
2073 decks.

2074 6. Conclusions

2075 The next great planetary exploration mission may well be a flagship mission
2076 to one of the ice giant planets, possibly Uranus with its unique obliquity and
2077 correspondingly extreme planetary seasons, its unusual dearth of cloud features
2078 and radiated internal energy, a tenuous ring system and multitude of small
2079 moons, or to the Neptune system, with its enormous winds, system of ring arcs,
2080 sporadic atmospheric features, and large retrograde moon Triton, possibly a

2081 captured dwarf planet. **The ice giant planets represent the last unex-**
2082 **plored class of planets in the solar system and the most frequently**
2083 **observed type of exoplanets.** Extended studies of one or both ice giants,
2084 including *in situ* with an entry probe, are necessary to further constrain mod-
2085 els of solar system formation and chemical, thermal, and dynamical evolution,
2086 the atmospheric formation, evolution, and processes, and to provide additional
2087 groundtruth for improved understanding of extrasolar planetary systems. The
2088 giant planets, gas and ice giants together, additionally offer a laboratory for
2089 studying the dynamics, chemistry, and processes of Earth's atmosphere. Only
2090 *in situ* exploration by a descent probe (or probes) can unlock the secrets of the
2091 deep, well-mixed atmospheres where pristine materials from the epoch of solar
2092 system formation can be found. Particularly important are the noble gases,
2093 undetectable by any means other than direct sampling, that carry many of the
2094 secrets of giant planet origin and evolution. Both absolute as well as relative
2095 abundances of the noble gases are needed to understand the properties of the
2096 interplanetary medium at the location and epoch of solar system formation, the
2097 delivery of heavy elements to the ice giant atmospheres, and to help decipher
2098 evidence of possible giant planet migration. A key result from a Uranus or Nep-
2099 tune entry probe would be the indication as to whether the enhancement of the
2100 heavier noble gases found by the Galileo probe at Jupiter (and hopefully con-
2101 firmed by a future Saturn probe) is a feature common to all the giant planets,
2102 or is limited only to the gas giants.

2103 The primary goal of an ice-giant entry-probe mission is to measure the well-
2104 mixed abundances of the noble gases He, Ne, Ar, Kr, Xe and their isotopes,
2105 the heavier elements C, N, S, and P, key isotope ratios $^{15}\text{N}/^{14}\text{N}$, $^{13}\text{C}/^{12}\text{C}$,
2106 $^{17}\text{O}/^{16}\text{O}$ and $^{18}\text{O}/^{16}\text{O}$, and D/H, and disequilibrium species CO and PH₃ which
2107 act as tracers of internal processes, and can be achieved by an ice-giant probe
2108 reaching 10 bars. In addition to measurements of the noble gas, chemical,
2109 and isotopic abundances in the atmosphere, a probe would measure many of
2110 the chemical and dynamical processes within the upper atmosphere, providing
2111 an improved context for understanding the ice giants, the entire family of giant

2112 planets (gas giants and ice giants), and the solar system, and to provide ground-
2113 truth measurement to improve understanding of extrasolar planets. A descent
2114 probe would sample atmospheric regions far below those accessible to remote
2115 sensing, well into the cloud forming regions of the troposphere to depths where
2116 many cosmogenically important and abundant species are expected to be well-
2117 mixed. Along the probe descent, the probe would provide direct tracking of the
2118 planet's atmospheric dynamics including zonal winds, waves, convection and
2119 turbulence, measurements of the thermal profile and stability of the atmosphere,
2120 and the location, density, and composition of the upper cloud layers.

2121 Results obtained from an ice-giant probe are necessary to improve our un-
2122 derstanding of the processes by which the ice giants formed, including the com-
2123 position and properties of the local solar nebula at the time and location of ice
2124 giant formation. By extending the legacy of the Galileo probe mission and pos-
2125 sibly a future Saturn entry probe mission, Uranus and Neptune probe(s) would
2126 further discriminate between and refine theories addressing the formation, and
2127 chemical, dynamical, and thermal evolution of the giant planets, the entire solar
2128 system including Earth and the other terrestrial planets, and the formation of
2129 other planetary systems.

2130 **Acknowledgements**

2131 We wish to acknowledge Leslie Young for her very constructive comments
2132 and corrections. The work contributed by O.M., B.B. and T.R. was carried out
2133 thanks to the support of the A*MIDEX project (n° ANR-11-IDEX-0001-02)
2134 funded by the “Investissements d’Avenir” French Government program, man-
2135 aged by the French National Research Agency (ANR). We acknowledge support
2136 from the “Institut National des Sciences de l’Univers” (INSU), the “Centre
2137 National de la Recherche Scientifique” (CNRS) and “Centre National d’Etude
2138 Spatiale” (CNES). Parts of this research were carried out at the Jet Propul-
2139 sion Laboratory, California Institute of Technology, under a contract with the
2140 National Aeronautics and Space Administration. D.H.A, M.D.H., G.S.O., K.R.

2141 and C.S. were supported by NASA funds to the Jet Propulsion Laboratory,
2142 California Institute of Technology. L.N.F was supported by a Royal Society
2143 Research Fellowship and European Research Council Grant at the University
2144 of Leicester. R.H. and A.S.L. were supported by the Spanish MINECO project
2145 AYA2015-65041-P (MINECO/FEDER, UE) and Grupos Gobierno Vasco IT-
2146 765-13. P.W. acknowledges support from the Swiss National Science Founda-
2147 tion. J.H.W. acknowledges the support of Southwest Research Institute.

2148 Achterberg, R. K., Schinder, P. J., Flasar, F. M. 2016. Saturn's Helium Abun-
2149 dance from Cassini CIRS and RSS Data. AAS/Division for Planetary Sciences
2150 Meeting Abstracts 48, 508.01.

2151 Alexander, R. D., Armitage, P. J. 2009. Giant Planet Migration, Disk Evolution,
2152 and the Origin of Transitional Disks. *The Astrophysical Journal* 704, 989-
2153 1001.

2154 Ali-Dib, M., Mousis, O., Petit, J.-M., Lunine, J. I. 2014. The Measured Com-
2155 positions of Uranus and Neptune from their Formation on the CO Ice Line.
2156 *The Astrophysical Journal* 793, 9.

2157 Alibert, Y., Mousis, O., Mordasini, C., Benz, W. 2005b. New Jupiter and Saturn
2158 Formation Models Meet Observations. *The Astrophysical Journal* 626, L57-
2159 L60.

2160 Alibert, Y., Mousis, O., Benz, W. 2005a. On the Volatile Enrichments and
2161 Composition of Jupiter. *The Astrophysical Journal* 622, L145-L148.

2162 Alibert, Y., Mordasini, C., Benz, W. 2004. Migration and giant planet forma-
2163 tion. *Astronomy and Astrophysics* 417, L25-L28.

2164 Allison, M., Beebe, R. F., Conrath, B. J., Hinson, D. P., Ingersoll, A. P. 1991.
2165 Uranus atmospheric dynamics and circulation. *Uranus* 253-295.

2166 Altwegg, K., and 31 colleagues 2015. 67P/Churyumov-Gerasimenko, a Jupiter
2167 family comet with a high D/H ratio. *Science* 347, 1261952.

- 2168 Aplin, K. L., Harrison, R. G. 2016. Determining solar effects in Neptune's at-
2169 mosphere. *Nature Communications* 7, 11976.
- 2170 Arridge, C. S., and 113 colleagues 2014. The science case for an orbital mission
2171 to Uranus: Exploring the origins and evolution of ice giant planets. *Planetary
2172 and Space Science* 104, 122-140.
- 2173 Arridge, C. S., and 78 colleagues 2012. Uranus Pathfinder: exploring the origins
2174 and evolution of Ice Giant planets. *Experimental Astronomy* 33, 753-791.
- 2175 Aslam, S., and 11 colleagues 2015. Net Flux Radiometer for a Saturn probe.
2176 European Planetary Science Congress 2015, held 27 September - 2 October,
2177 2015 in Nantes, France.
- 2178 Aslam, S., Akturk, A., Quilligan, G. 2012. A Radiation Hard Multi-Channel
2179 Digitizer ASIC for Operation in the Harsh Jovian Environment, In *Extreme
2180 Environment Electronics*, Ed. J. D. Cressler, H. A. Mantooth, CRC Press,
2181 Boca Raton, FL, Nov. 2012, ISBN: 978-1-4398-7430-1.
- 2182 Asplund, M., Grevesse, N., Sauval, A. J., Scott, P. 2009. The Chemical Compo-
2183 sition of the Sun. *Annual Review of Astronomy and Astrophysics* 47, 481-522.
- 2184 Atkinson, D. H., and 17 colleagues 2016. Exploring Saturn - The Saturn PRobe
2185 Interior and aTmosphere Explorer (SPRITE) Mission. AAS/Division for
2186 Planetary Sciences Meeting Abstracts 48, 123.29.
- 2187 Atkinson, D. H., and 16 colleagues 2014. In Situ Probe Science at Saturn. 11th
2188 International Planetary Probe Workshop 1795, 8005.
- 2189 Atkinson, D. H., and 11 colleagues 2013. Science from Shallow Saturn Entry
2190 Probes. European Planetary Science Congress 2013, held 8-13 September in
2191 London, UK.
- 2192 Atkinson, D. H., and 11 colleagues 2012. A Shallow Entry Probe Mission to
2193 Saturn. EGU General Assembly Conference Abstracts 14, 3172.

- 2194 Atkinson, D. H., Pollack, J. B., Seiff, A. 1998. The Galileo probe Doppler wind
2195 experiment: Measurement of the deep zonal winds on Jupiter. *Journal of*
2196 *Geophysical Research* 103, 22911-22928.
- 2197 Atkinson, D. H., Ingersoll, A. P., Seiff, A. 1997. Deep winds on Jupiter as
2198 measured by the Galileo probe. *Nature* 388, 649-650.
- 2199 Atreya, S. K., Crida, A., Guillot, T., Lunine, J. I., Madhusudhan, N., Mousis,
2200 O. 2016. The Origin and Evolution of Saturn, with Exoplanet Perspective.
2201 ArXiv e-prints arXiv:1606.04510.
- 2202 Atreya, S. K., Wong, A.-S. 2005. Coupled Clouds and Chemistry of the Giant
2203 Planets – A Case for Multiprobes. *Space Science Reviews* 116, 121-136.
- 2204 Atreya, S. K., Wong, A. S. 2004. Clouds of Neptune and Uranus. *Proceedings,*
2205 *International Planetary probe Workshop, NASA Ames, 2004, NASA CP-*
2206 *2004-213456.*
- 2207 Atreya, S. K., Mahaffy, P. R., Niemann, H. B., Wong, M. H., Owen, T. C.
2208 2003. Composition and origin of the atmosphere of Jupiter - an update, and
2209 implications for the extrasolar giant planets. *Planetary and Space Science* 51,
2210 105-112.
- 2211 Atreya, S. K., Wong, M. H., Owen, T. C., et al. 1999, *Planetary and Space*
2212 *Science* 47, 1243
- 2213 Atreya, S. K., Sandel, B. R., Romani, P. N. 1991. Photochemistry and vertical
2214 mixing. *Uranus* 110-146.
- 2215 Atreya, S. K., Donahue, T. M., Nagy, A. F., Waite, J. H., Jr., McConnell,
2216 J. C. 1984. Theory, measurements, and models of the upper atmosphere and
2217 ionosphere of Saturn. *Saturn* 239-277.
- 2218 Atreya, S. K., Ponthieu, J. J. 1983. Photolysis of methane and the ionosphere
2219 of Uranus. *Planetary and Space Science* 31, 939-944.

- 2220 Aurnou, J., Heimpel, M., Wicht, J. 2007. The effects of vigorous mixing in a
2221 convective model of zonal flow on the ice giants. *Icarus* 190, 110-126.
- 2222 Baines, K. H., Mickelson, M. E., Larson, L. E., Ferguson, D. W. 1995. The
2223 abundances of methane and ortho/para hydrogen on Uranus and Neptune:
2224 Implications of New Laboratory 4-0 H₂ quadrupole line parameters. *Icarus*
2225 114, 328-340.
- 2226 Baines, K. H., Hammel, H. B. 1994. Clouds, hazes, and the stratospheric
2227 methane abundance in Neptune. *Icarus* 109, 20-39.
- 2228 Balsiger, H., and 30 colleagues 2015. Detection of argon in the coma of
2229 comet 67P/Churyumov-Gerasimenko, *Science Advances* 1:e1500377 1–4, DOI:
2230 10.1126/sciadv.1500377.
- 2231 Balsiger, H., and 49 colleagues 2007. Rosina Rosetta Orbiter Spectrometer for
2232 Ion and Neutral Analysis. *Space Science Reviews* 128, 745-801.
- 2233 Batygin, K., Brown, M. E., Betts, H. 2012. Instability-driven Dynamical Evo-
2234 lution Model of a Primordially Five-planet Outer Solar System. *The Astro-*
2235 *physical Journal* 744, L3.
- 2236 Batygin, K., Brown, M. E. 2010. Early Dynamical Evolution of the Solar System:
2237 Pinning Down the Initial Conditions of the Nice Model. *The Astrophysical*
2238 *Journal* 716, 1323-1331.
- 2239 Bar-Nun, A., Natesco, G., Owen, T. 2007. Trapping of N₂, CO and Ar in
2240 amorphous ice – Application to comets. *Icarus* 190, 655-659.
- 2241 Bar-Nun, A., Kleinfeld, I., Kochavi, E. 1988. Trapping of gas mixtures by amor-
2242 phous water ice. *Physical Review B* 38, 7749-7754.
- 2243 Benz, W., Slattery, W. L., Cameron, A. G. W. 1989. Tilting Uranus in a giant
2244 impact. *Meteoritics* 24, 251.

- 2245 Bézard, B., Lellouch, E., Strobel, D., Maillard, J.-P., Drossart, P. 2002. Carbon
2246 Monoxide on Jupiter: Evidence for Both Internal and External Sources. *Icarus*
2247 159, 95-111.
- 2248 Bézard, B., Romani, P. N., Feuchtgruber, H., Encrenaz, T. 1999. Detection of
2249 the Methyl Radical on Neptune. *The Astrophysical Journal* 515, 868-872.
- 2250 Bézard, B., Romani, P. N., Conrath, B. J., Maguire, W. C. 1991. Hydrocar-
2251 bons in Neptune's stratosphere from Voyager infrared observations. *Journal*
2252 *of Geophysical Research* 96, 18.
- 2253 Bishop, J., Atreya S. K., Romani P. N., Orton G. S., Sandel B. R., Yelle, R.
2254 V. 1995. Book Chapter in *Neptune and Triton* by D. P. Cruikshank, Mil-
2255 dred Shapley Matthews, A. M. Schumann. ISBN-10: 0816515255. ISBN-
2256 13:9780816515257. Pub. Date: 11/01/1995. *Neptune and Triton*, p. 427,
2257 Cruikshank, D. P., ed., University of Arizona Press.
- 2258 Bishop, J., Atreya, S. K., Romani, P. N., Sandel, B. R., Herbert, F. 1992.
2259 Voyager 2 ultraviolet spectrometer solar occultations at Neptune - Constraints
2260 on the abundance of methane in the stratosphere. *Journal of Geophysical*
2261 *Research* 97, 11.
- 2262 Bishop, J., Atreya, S. K., Herbert, F., Romani, P. 1990. Reanalysis of Voyager
2263 2 UVS occultations at Uranus - Hydrocarbon mixing ratios in the equatorial
2264 stratosphere. *Icarus* 88, 448-464.
- 2265 Bockelée-Morvan, D., and 21 colleagues 2012. Herschel measurements of the
2266 D/H and $^{16}\text{O}/^{18}\text{O}$ ratios in water in the Oort-cloud comet C/2009 P1 (Gar-
2267 radd). *Astronomy and Astrophysics* 544, L15.
- 2268 Bockelée-Morvan, D., Crovisier, J., Mumma, M. J., Weaver, H. A. 2004. The
2269 composition of cometary volatiles. *Comets II* 391-423.
- 2270 Boese, R. W., Twarowski, R. J., Gilland, J., Hassig, R. E., Brown, F. G. 1980.
2271 The infrared radiometer on the sounder probe of the Pioneer Venus mission.
2272 *IEEE Transactions on Geoscience and Remote Sensing* 18, 97-100.

- 2273 Bolton, S. J., and 42 colleagues 2017. Jupiter's interior and deep atmosphere:
2274 The initial pole-to-pole passes with the Juno spacecraft. *Science* 356, 821-825.
- 2275 Boss, A. P., Wetherill, G. W., Haghhighipour, N. 2002. NOTE: Rapid Formation
2276 of Ice Giant Planets. *Icarus* 156, 291-295.
- 2277 Boss, A. P. 1997. Giant planet formation by gravitational instability. *Science*
2278 276, 1836-1839.
- 2279 Briggs, F. H., Sackett, P. D. 1989. Radio observations of Saturn as a probe of
2280 its atmosphere and cloud structure. *Icarus* 80, 77-103.
- 2281 Bright, L.E. 1984. Galileo Probe-Orbiter Relay Link Integration Report. 1625,
2282 145, Rev. A (internal document), Jet Propulsion Laboratory, California In-
2283 stitute of Technology, Pasadena, California.
- 2284 Briois, C., and 20 colleagues 2016. Orbitrap mass analyser for in situ charac-
2285 terisation of planetary environments: Performance evaluation of a laboratory
2286 prototype. *Planetary and Space Science* 131, 33-45.
- 2287 Briois, C., and 22 colleagues 2013. DOTS: A High Resolution Orbitrap Mass
2288 Spectrometer for In Situ Analysis of the surface samples of Airless Planetary
2289 Bodies. EGU General Assembly Conference Abstracts 15, 14225.
- 2290 Brockwell T., Meech, K. J., Pickens, K., Waite, J. H., Miller, G., Roberts,
2291 J., Lunine, J. I., Wilson, P., 2016, The MAss Spectrometer for Planetary
2292 EXploration (MASPEX), IEEE, 1-17, DOI: 10.1109/AERO.2016.7500777.
- 2293 Burgdorf, M., Orton, G., van Cleve, J., Meadows, V., Houck, J. 2006. Detection
2294 of new hydrocarbons in Uranus' atmosphere by infrared spectroscopy. *Icarus*
2295 184, 634-637.
- 2296 Burgdorf, M., Orton, G. S., Davis, G. R., Sidher, S. D., Feuchtgruber, H.,
2297 Griffin, M. J., Swinyard, B. M. 2003. Neptune's far-infrared spectrum from
2298 the ISO long-wavelength and short-wavelength spectrometers. *Icarus* 164, 244-
2299 253.

- 2300 Cavalié, T., Venot, O., Selsis, F., Hersant, F., Hartogh, P., Leconte, J. 2017.
2301 Thermochemistry and vertical mixing in the tropospheres of Uranus and Nep-
2302 tune: How convection inhibition can affect the derivation of deep oxygen
2303 abundances. *Icarus* 291, 1-16.
- 2304 Cavalié, T., and 10 colleagues 2014. The first submillimeter observation of CO
2305 in the stratosphere of Uranus. *Astronomy and Astrophysics* 562, A33.
- 2306 Clausen, K. C., Hassan, H., Verdant, M., Couzin, P., Huttin, G., Brisson, M.,
2307 Sollazzo, C., Lebreton, J.-P. 2002. The Huygens Probe System Design. *Space*
2308 *Science Reviews* 104, 155-189.
- 2309 Colin, L., Hunten, D. M. 1977. 11. Pioneer venus experiment descriptions. *Space*
2310 *Science Reviews* 20, 451-525.
- 2311 Conrath, B. J., Gautier, D. 2000. Saturn Helium Abundance: A Reanalysis of
2312 Voyager Measurements. *Icarus* 144, 124-134.
- 2313 Conrath, B. J., Gierasch, P. J., Ustinov, E. A. 1998. Thermal Structure and Para
2314 Hydrogen Fraction on the Outer Planets from Voyager IRIS Measurements.
2315 *Icarus* 135, 501-517.
- 2316 Conrath, B. J., Gautier, D., Owen, T. C., Samuelson, R. E. 1993. Constraints
2317 on N₂ in Neptune's atmosphere from Voyager measurements. *Icarus* 101, 168-
2318 171.
- 2319 Conrath, B. J., Flasar, F. M., Gierasch, P. J. 1991. Thermal structure and
2320 dynamics of Neptune's atmosphere from Voyager measurements. *Journal of*
2321 *Geophysical Research* 96, 18.
- 2322 Conrath, B., Hanel, R., Gautier, D., Marten, A., Lindal, G. 1987. The helium
2323 abundance of Uranus from Voyager measurements. *Journal of Geophysical*
2324 *Research* 92, 15003-15010.
- 2325 Conrath, B. J., Gautier, D., Hanel, R. A., Hornstein, J. S. 1984. The helium
2326 abundance of Saturn from Voyager measurements. *The Astrophysical Journal*
2327 282, 807-815.

- 2328 Courtin, R., Swinyard, B. M., Moreno, R., Fulton, T., Lellouch, E., Rengel,
2329 M., Hartogh, P. 2011. First results of Herschel-SPIRE observations of Titan.
2330 *Astronomy and Astrophysics* 536, L2.
- 2331 Courtin, R., Gautier, D., Marten, A., Bezard, B., Hanel, R. 1984. The compo-
2332 sition of Saturn's atmosphere at northern temperate latitudes from Voyager
2333 IRIS spectra - NH_3 , PH_3 , C_2H_2 , C_2H_6 , CH_3D , CH_4 , and the Saturnian D/H
2334 isotopic ratio. *The Astrophysical Journal* 287, 899-916.
- 2335 Cyr, K. E., Sears, W. D., Lunine, J. I. 1998. Distribution and Evolution of Water
2336 Ice in the Solar Nebula: Implications for Solar System Body Formation. *Icarus*
2337 135, 537-548.
- 2338 Davis, G. R., and 26 colleagues 1996. ISO LWS measurement of the far-infrared
2339 spectrum of Saturn. *Astronomy and Astrophysics* 315, L393-L396.
- 2340 de Graauw, T., and 18 colleagues 1997. First results of ISO-SWS observations of
2341 Saturn: detection of CO_2 , $\text{CH}_3\text{C}_2\text{H}$, C_4H_2 and tropospheric H_2O .
2342 *Astronomy and Astrophysics* 321, L13-L16.
- 2343 de Kleer, K., Luszcz-Cook, S., de Pater, I., Ádámkóvics, M., Hammel,
2344 H. B. 2015. Clouds and aerosols on Uranus: Radiative transfer modeling
2345 of spatially-resolved near-infrared Keck spectra. *Icarus* 256, 120-137.
- 2346 de Pater, I., Sromovsky, L. A., Fry, P. M., Hammel, H. B., Baranec, C.,
2347 Sayanagi, K. M. 2015. Record-breaking storm activity on Uranus in 2014.
2348 *Icarus* 252, 121-128.
- 2349 de Pater, I., Fletcher, L. N., Luszcz-Cook, S., DeBoer, D., Butler, B., Hammel,
2350 H. B., Sitko, M. L., Orton, G., Marcus, P. S. 2014. Neptune's global circulation
2351 deduced from multi-wavelength observations. *Icarus* 237, 211-238.
- 2352 de Pater, I., Sromovsky, L. A., Hammel, H. B., Fry, P. M., LeBeau, R. P.,
2353 Rages, K., Showalter, M., Matthews, K. 2011. Post-equinox observations of
2354 Uranus: Berg's evolution, vertical structure, and track towards the equator.
2355 *Icarus* 215, 332-345.

- 2356 de Pater, I., Romani, P. N., Atreya, S. K. 1991. Possible microwave absorption
2357 by H₂S gas in Uranus' and Neptune's atmospheres. *Icarus* 91, 220-233.
- 2358 de Pater, I., Romani, P. N., Atreya, S. K. 1989. Uranus deep atmosphere re-
2359 vealed. *Icarus* 82, 288-313.
- 2360 de Pater, I., Massie, S. T. 1985. Models of the millimeter-centimeter spectra of
2361 the giant planets. *Icarus* 62, 143-171.
- 2362 DeBoer, D. R., Steffes, P. G. 1996. Estimates of the Tropospheric Vertical Struc-
2363 ture of Neptune Based on Microwave Radiative Transfer Studies. *Icarus* 123,
2364 324-335.
- 2365 DeBoer, D. R., Steffes, P. G. 1994. Laboratory measurements of the microwave
2366 properties of H₂S under simulated Jovian conditions with an application to
2367 Neptune. *Icarus* 109, 352-366.
- 2368 Del Genio, A. D., Achterberg, R. K., Baines, K. H., Flasar, F. M., Read, P. L.,
2369 Sanchez-Lavega, A., Showman, A. P. 2009. Saturn Atmospheric Structure
2370 and Dynamics. *Saturn from Cassini-Huygens* 113.
- 2371 Denisov, E., Damoc, E., Lange, O., Makarov, A. 2012. Orbitrap mass spectrom-
2372 etry with resolving powers above 1,000,000. *International Journal of Mass*
2373 *Spectrometry* 325, 80-85.
- 2374 Dhooghe, F., and 27 colleagues 2017, *Mon. Not. Roy. Aca. Sc.*, submitted.
- 2375 Dobrijevic, M., Loison, J. C. 2017. The photochemical fractionation of nitrogen
2376 isotopologues in Titan's atmosphere. *Icarus*, submitted.
- 2377 Dobrijevic, M., Cavalié, T., Hébrard, E., Billebaud, F., Hersant, F., Selsis,
2378 F. 2010. Key reactions in the photochemistry of hydrocarbons in Neptune's
2379 stratosphere. *Planetary and Space Science* 58, 1555-1566.
- 2380 Dodson-Robinson, S. E., Bodenheimer, P. 2010. The formation of Uranus and
2381 Neptune in solid-rich feeding zones: Connecting chemistry and dynamics.
2382 *Icarus* 207, 491-498.

- 2383 Durry, G., and 12 colleagues 2010. Near infrared diode laser spectroscopy of
2384 C_2H_2 , H_2O , CO_2 and their isotopologues and the application to TDLAS, a
2385 tunable diode laser spectrometer for the martian PHOBOS-GRUNT space
2386 mission. *Applied Physics B: Lasers and Optics* 99, 339-351.
- 2387 Durry, G., Hauchecorne, A., Ovarlez, J., Ovarlez, H., Pouchet, I., Zeninari, V.,
2388 Parvitte, B., 2002. In situ measurement of H_2O and CH_4 with telecommuni-
2389 cation laser diodes in the lower stratosphere: dehydration and indication of a
2390 tropical air intrusion at mid-latitudes. *J. Atmos. Chem.* 43 (3), 175–194.
- 2391 Edgar, R. G. 2007. Giant Planet Migration in Viscous Power-Law Disks. *The*
2392 *Astrophysical Journal* 663, 1325-1334.
- 2393 Ellerby, D., and 12 colleagues 2016. Heatshield for Extreme Entry Environ-
2394 ment Technology (HEEET) Development Status. 13th International Plane-
2395 tary Probe Workshop, Laurel, Maryland, USA.
- 2396 Elliott, J., and 29 colleagues 2017. Ice Giants. Pre-Decadal Survey Mission Study
2397 Report, JPL D-100520.
- 2398 Encrenaz, T., Lellouch, E., Drossart, P., Feuchtgruber, H., Orton, G. S., Atreya,
2399 S. K. 2004. First detection of CO in Uranus. *Astronomy and Astrophysics* 413,
2400 L5-L9.
- 2401 Encrenaz, T., Schulz, B., Drossart, P., Lellouch, E., Feuchtgruber, H., Atreya,
2402 S. K. 2000. The ISO spectra of Uranus and Neptune between 2.5 and 4.2
2403 μm : constraints on albedos and H_3^+ . *Astronomy and Astrophysics* 358,
2404 L83-L87.
- 2405 Encrenaz, T., Feuchtgruber, H., Atreya, S. K., Bezard, B., Lellouch, E., Bishop,
2406 J., Edgington, S., Degraauw, T., Griffin, M., Kessler, M. F. 1998. ISO ob-
2407 servations of Uranus: The stratospheric distribution of C_2H_2 and the eddy
2408 diffusion coefficient. *Astronomy and Astrophysics* 333, L43-L46.

- 2409 Fegley, B., Prinn, R. G. 1988. Chemical constraints on the water and total
2410 oxygen abundances in the deep atmosphere of Jupiter. *The Astrophysical*
2411 *Journal* 324, 621-625.
- 2412 Fegley, B., Prinn, R. G. 1985. Predicted chemistry of the deep atmosphere of
2413 Uranus before the Voyager 2 encounter. *Nature* 318, 48-50.
- 2414 Feuchtgruber, H., and 11 colleagues 2013. The D/H ratio in the atmospheres
2415 of Uranus and Neptune from Herschel-PACS observations. *Astronomy and*
2416 *Astrophysics* 551, A126.
- 2417 Feuchtgruber, H., Lellouch, E., de Graauw, T., Bézard, B., Encrenaz, T., Griffin,
2418 M. 1997. External supply of oxygen to the atmospheres of the giant planets.
2419 *Nature* 389, 159-162.
- 2420 Flasar, F. M., Conrath, B. J., Pirraglia, J. A., Gierasch, P. J. 1987. Voyager in-
2421 frared observations of Uranus' atmosphere - Thermal structure and dynamics.
2422 *Journal of Geophysical Research* 92, 15011-15018.
- 2423 Fletcher, L. N., Greathouse, T. K., Moses, J. I., Guerlet, S., West, R. A. 2015.
2424 Saturn's Seasonally Changing Atmosphere: Thermal Structure, Composition
2425 and Aerosols. ArXiv e-prints arXiv:1510.05690.
- 2426 Fletcher, L. N., Greathouse, T. K., Orton, G. S., Irwin, P. G. J., Mousis, O.,
2427 Sinclair, J. A., Giles, R. S. 2014b. The origin of nitrogen on Jupiter and
2428 Saturn from the $^{15}\text{N}/^{14}\text{N}$ ratio. *Icarus* 238, 170-190.
- 2429 Fletcher, L. N., de Pater, I., Orton, G. S., Hammel, H. B., Sitko, M. L., Irwin,
2430 P. G. J. 2014a. Neptune at summer solstice: Zonal mean temperatures from
2431 ground-based observations, 2003-2007. *Icarus* 231, 146-167.
- 2432 Fletcher, L. N., Baines, K. H., Momary, T. W., Showman, A. P., Irwin, P. G. J.,
2433 Orton, G. S., Roos-Serote, M., Merlet, C. 2011. Saturn's tropospheric com-
2434 position and clouds from Cassini/VIMS 4.6-5.1 μm nightside spectroscopy.
2435 *Icarus* 214, 510-533.

- 2436 Fletcher, L. N., Drossart, P., Burgdorf, M., Orton, G. S., Encrenaz, T. 2010.
2437 Neptune's atmospheric composition from AKARI infrared spectroscopy. *As-*
2438 *tronomy and Astrophysics* 514, A17.
- 2439 Fletcher, L. N., Orton, G. S., Teanby, N. A., Irwin, P. G. J. 2009b. Phosphine
2440 on Jupiter and Saturn from Cassini/CIRS. *Icarus* 202, 543-564.
- 2441 Fletcher, L. N., Orton, G. S., Teanby, N. A., Irwin, P. G. J., Bjoraker, G. L.
2442 2009a. Methane and its isotopologues on Saturn from Cassini/CIRS observa-
2443 tions. *Icarus* 199, 351-367.
- 2444 Fletcher, L. N., Irwin, P. G. J., Teanby, N. A., Orton, G. S., Parrish, P. D.,
2445 Calcutt, S. B., Bowles, N., de Kok, R., Howett, C., Taylor, F. W. 2007.
2446 The meridional phosphine distribution in Saturn's upper troposphere from
2447 Cassini/CIRS observations. *Icarus* 188, 72-88.
- 2448 Folkner, W. M., Woo, R., Nandi, S. 1998. Ammonia abundance in Jupiter's
2449 atmosphere derived from the attenuation of the Galileo probe's radio signal.
2450 *Journal of Geophysical Research* 103, 22847-22856.
- 2451 Fortney, J. J., Nettelmann, N. 2010. The Interior Structure, Composition, and
2452 Evolution of Giant Planets. *Space Science Reviews* 152, 423-447.
- 2453 Fouchet, T., Lellouch, E., Feuchtgruber, H. 2003. The hydrogen ortho-to-para
2454 ratio in the stratospheres of the giant planets. *Icarus* 161, 127-143.
- 2455 Fouchet, T., Lellouch, E., Bézard, B., Encrenaz, T., Drossart, P., Feuchtgruber,
2456 H., de Graauw, T. 2000. ISO-SWS Observations of Jupiter: Measurement of
2457 the Ammonia Tropospheric Profile and of the $^{15}\text{N}/^{14}\text{N}$ Isotopic Ratio. *Icarus*
2458 143, 223-243.
- 2459 French, R. G., McGhee, C. A., Sicardy, B. 1998. Neptune's Stratospheric Winds
2460 from Three Central Flash Occultations. *Icarus* 136, 27-49.
- 2461 Fry, P. M., Sromovsky, L. A., de Pater, I., Hammel, H. B., Rages, K. A. 2012.
2462 Detection and Tracking of Subtle Cloud Features on Uranus. *The Astronom-*
2463 *ical Journal* 143, 150.

- 2464 Fulchignoni, M., and 42 colleagues 2005. In situ measurements of the physical
2465 characteristics of Titan's environment. *Nature* 438, 785-791.
- 2466 Fulchignoni, M., et al., 2002, The Characterisation of Titan's Atmospheric Phys-
2467 ical Properties by the Huygens Atmospheric Structure Instrument (HASI),
2468 *Space Science Reviews*, 104(1), 397-434
- 2469 Gautier, D., Hersant, F. 2005. Formation and Composition of Planetesimals.
2470 *Space Science Reviews* 116, 25-52.
- 2471 Gautier, D., Hersant, F., Mousis, O., Lunine, J. I. 2001. Enrichments in Volatiles
2472 in Jupiter: A New Interpretation of the Galileo Measurements. *The Astro-*
2473 *physical Journal* 550, L227-L230.
- 2474 Gayet, J. F., Crépel, O., Fournol, J. F., Oshchepkov, S. 1997. A new airborne
2475 polar Nephelometer for the measurements of optical and microphysical cloud
2476 properties. Part I: Theoretical design. *Annales Geophysicae* 15, 451-459.
- 2477 Geiss, J., Gloeckler, G. 1998. Abundances of Deuterium and Helium-3 in the
2478 Protosolar Cloud. *Space Science Reviews* 84, 239-250.
- 2479 Gierasch, P. J., Conrath, B. J. 1987. Vertical temperature gradients on Uranus
2480 - Implications for layered convection. *Journal of Geophysical Research* 92,
2481 15019-15029.
- 2482 Goesmann, F., Rosenbauer, H., Roll, R., Szopa, C., Raulin, F., Sternberg, R.,
2483 Israel, G., Meierhenrich, U., Thiemann, W., Munoz-Caro, G. 2007. Cosac,
2484 The Cometary Sampling and Composition Experiment on Philae. *Space Sci-*
2485 *ence Reviews* 128, 257-280.
- 2486 Gomes, R., Levison, H. F., Tsiganis, K., Morbidelli, A. 2005. Origin of the cat-
2487 aclysmic Late Heavy Bombardment period of the terrestrial planets. *Nature*
2488 435, 466-469.
- 2489 Greathouse, T. K., Richter, M., Lacy, J., Moses, J., Orton, G., Encrenaz, T.,
2490 Hammel, H. B., Jaffe, D. 2011. A spatially resolved high spectral resolution
2491 study of Neptune's stratosphere. *Icarus* 214, 606-621.

- 2492 Greve, A., Steppe, H., Graham, D., Schalinski, C. J. 1994. Disk brightness
2493 temperature of the planets at 43 GHz (and 43 GHz flux densities of some
2494 continuum sources). *Astronomy and Astrophysics* 286, 654-658.
- 2495 Grimm, H., Eatough, D. J. 2009. Aerosol measurement: the use of optical
2496 light scattering for the determination of particulate size distribution, and
2497 particulate mass, including the semi-volatile fraction, *Journal of the Air &*
2498 *Waste Management Association*, 59, 101–107.
- 2499 Guillot, T., Hueso, R. 2006. The composition of Jupiter: sign of a (relatively)
2500 late formation in a chemically evolved protosolar disc. *Monthly Notices of the*
2501 *Royal Astronomical Society* 367, L47-L51.
- 2502 Guillot, T. 2005. The interiors of giant planets: Models and Outstanding Ques-
2503 tions. *Annual Review of Earth and Planetary Sciences* 33, 493-530.
- 2504 Guillot, T. 1995. Condensation of Methane, Ammonia, and Water and the In-
2505 hibition of Convection in Giant Planets. *Science* 269, 1697-1699.
- 2506 Guilloteau, S., Dutrey, A., Marten, A., Gautier, D. 1993. CO in the troposphere
2507 of Neptune: Detection of the $J = 1-0$ line in absorption. *Astronomy and*
2508 *Astrophysics* 279, 661-667.
- 2509 Gurnett, D. A., Kurth, W. S., Cairns, I. H., Granroth, L. J. 1990. Whistlers
2510 in Neptune's magnetosphere - Evidence of atmospheric lightning. *Journal of*
2511 *Geophysical Research* 95, 20967-20976.
- 2512 Hammel, H. B., Sromovsky, L. A., Fry, P. M., Rages, K., Showalter, M., de
2513 Pater, I., van Dam, M. A., LeBeau, R. P., Deng, X. 2009. The Dark Spot
2514 in the atmosphere of Uranus in 2006: Discovery, description, and dynamical
2515 simulations. *Icarus* 201, 257-271.
- 2516 Hammel, H. B., Lynch, D. K., Russell, R. W., Sitko, M. L., Bernstein, L. S.,
2517 Hewagama, T. 2006. Mid-Infrared Ethane Emission on Neptune and Uranus.
2518 *The Astrophysical Journal* 644, 1326-1333.

- 2519 Hammel, H. B., de Pater, I., Gibbard, S., Lockwood, G. W., Rages, K. 2005.
2520 Uranus in 2003: Zonal winds, banded structure, and discrete features. *Icarus*
2521 175, 534-545.
- 2522 Hammel, H. B., Rages, K., Lockwood, G. W., Karkoschka, E., de Pater, I. 2001.
2523 New Measurements of the Winds of Uranus. *Icarus* 153, 229-235.
- 2524 Hammel, H. B., Baines, K. H., Bergstralh, J. T. 1989. Vertical aerosol structure
2525 of Neptune - Constraints from center-to-limb profiles. *Icarus* 80, 416-438.
- 2526 Hässig, M., and 17 colleagues 2017. Isotopic composition of CO₂ in the coma
2527 of 67P/Churyumov-Gerasimenko measured with ROSINA/DFMS, *Astronom.*
2528 *Astrophys*, submitted.
- 2529 Helled, R., Guillot, T. 2017. Internal Structure of Giant and Icy Planets: Im-
2530 portance of Heavy Elements and Mixing. ArXiv e-prints arXiv:1705.09320.
- 2531 Helled, R., Lunine, J. 2014. Measuring Jupiter's water abundance by Juno: the
2532 link between interior and formation models. *Monthly Notices of the Royal*
2533 *Astronomical Society* 441, 2273-2279.
- 2534 Helled, R., Bodenheimer, P. 2014. The Formation of Uranus and Neptune: Chal-
2535 lenges and Implications for Intermediate-mass Exoplanets. *The Astrophysical*
2536 *Journal* 789, 69.
- 2537 Helled, R., Anderson, J. D., Podolak, M., Schubert, G. 2011. Interior Models of
2538 Uranus and Neptune. *The Astrophysical Journal* 726, 15.
- 2539 Helled, R., Podolak, M., Kovetz, A. 2006. Planetesimal capture in the disk
2540 instability model. *Icarus* 185, 64-71.
- 2541 Herbert, F., Sandel, B. R., Yelle, R. V., Holberg, J. B., Broadfoot, A. L.,
2542 Shemansky, D. E., Atreya, S. K., Romani, P. N. 1987. The upper atmosphere
2543 of Uranus - EUV occultations observed by Voyager 2. *Journal of Geophysical*
2544 *Research* 92, 15093-15109.

- 2545 Hersant, F., Gautier, D., Lunine, J. I. 2004. Enrichment in volatiles in the giant
2546 planets of the Solar System. *Planetary and Space Science* 52, 623-641.
- 2547 Hersant, F., Gautier, D., Huré, J.-M. 2001. A Two-dimensional Model for the
2548 Primordial Nebula Constrained by D/H Measurements in the Solar System:
2549 Implications for the Formation of Giant Planets. *The Astrophysical Journal*
2550 554, 391-407.
- 2551 Hesman, B. E., Davis, G. R., Matthews, H. E., Orton, G. S. 2007. The abun-
2552 dance profile of CO in Neptune's atmosphere. *Icarus* 186, 342-353.
- 2553 Hofer, L., and 10 colleagues 2015. Prototype of the gas chromatograph-mass
2554 spectrometer to investigate volatile species in the lunar soil for the Luna-
2555 Resurs mission. *Planetary and Space Science* 111, 126-133.
- 2556 Hofstadter, M., and 29 colleagues 2017. Ice Giants Pre-Decadal Survey Mission
2557 Study Report, JPL D-100520.
- 2558 Hofstadter, M. D., Butler, B. J. 2003. Seasonal change in the deep atmosphere
2559 of Uranus. *Icarus* 165, 168-180.
- 2560 Hörst, S. M., and 12 colleagues 2012. Formation of Amino Acids and Nucleotide
2561 Bases in a Titan Atmosphere Simulation Experiment. *Astrobiology* 12, 809-
2562 817.
- 2563 Hu, Q., Noll, R.J., Li, H., Makarov, A., Hardman, M., Cooks, R.G., 2005. The
2564 orbitrap: a new mass spectrometer. *J. Mass Spectrom.* 40 (4), 430-443.
- 2565 Hubbard, W. B., Podolak, M., Stevenson, D. J. 1995. The interior of Neptune.
2566 In: Cruikshank (Ed.), *Neptune and Triton*. University of Arizona, Tucson,
2567 109-138.
- 2568 Hubickyj, O., Bodenheimer, P., Lissauer, J. J. 2005. Accretion of the gaseous
2569 envelope of Jupiter around a 5-10 Earth-mass core. *Icarus* 179, 415-431.
- 2570 Hueso, R., and 34 colleagues 2017. Neptune long-lived atmospheric features in
2571 2013-2015 from small (28-cm) to large (10-m) telescopes. *Icarus* 295, 89-109.

- 2572 Irwin, P. G. J., Wong, M. H., Simon, A. A., Orton, G. S., Toledo, D. 2017.
2573 HST/WFC3 observations of Uranus' 2014 storm clouds and comparison with
2574 VLT/SINFONI and IRTF/Spex observations. *Icarus* 288, 99-119.
- 2575 Irwin, P. G. J., Fletcher, L. N., Tice, D., Owen, S. J., Orton, G. S., Teanby,
2576 N. A., Davis, G. R. 2016b. Time variability of Neptune's horizontal and verti-
2577 cal cloud structure revealed by VLT/SINFONI and Gemini/NIFS from 2009
2578 to 2013. *Icarus* 271, 418-437.
- 2579 Irwin, P. G. J., Fletcher, L. N., Read, P. L., Tice, D., de Pater, I., Orton, G. S.,
2580 Teanby, N. A., Davis, G. R. 2016a. Spectral analysis of Uranus' 2014 bright
2581 storm with VLT/SINFONI. *Icarus* 264, 72-89.
- 2582 Irwin, P. G. J. 2009. *Giant Planets of Our Solar System. Giant Planets of Our*
2583 *Solar System: Atmospheres, Composition, and Structure*, Springer Praxis
2584 Books. ISBN 978-3-540-85157-8. Springer Berlin Heidelberg, 2009 .
- 2585 Kaiser, M. L., Desch, M. D., Farrell, W. M., Zarka, P. 1991. Restrictions on the
2586 characteristics of Neptunian lightning. *Journal of Geophysical Research* 96,
2587 19.
- 2588 Karkoschka, E. 2015. Uranus' southern circulation revealed by Voyager 2:
2589 Unique characteristics. *Icarus* 250, 294-307.
- 2590 Karkoschka, E. 2011. Neptune's rotational period suggested by the extraordi-
2591 nary stability of two features. *Icarus* 215, 439-448.
- 2592 Karkoschka, E., Tomasko, M. G. 2011. The haze and methane distributions on
2593 Neptune from HST-STIS spectroscopy. *Icarus* 211, 780-797.
- 2594 Karkoschka, E., Tomasko, M. 2009. The haze and methane distributions on
2595 Uranus from HST-STIS spectroscopy. *Icarus* 202, 287-309.
- 2596 Karkoschka, E. 1998. Clouds of High Contrast on Uranus. *Science* 280, 570.

- 2597 Kaspi, Y., Showman, A. P., Hubbard, W. B., Aharonson, O., Helled, R. 2013.
2598 Atmospheric confinement of jet streams on Uranus and Neptune. *Nature* 497,
2599 344-347.
- 2600 Kaye, J. A., Strobel, D. F. 1984. Phosphine photochemistry in the atmosphere
2601 of Saturn. *Icarus* 59, 314-335.
- 2602 Lambrechts, M., Johansen, A. 2012. Rapid growth of gas-giant cores by pebble
2603 accretion. *Astronomy and Astrophysics* 544, A32.
- 2604 Le Barbu, T., Vinogradov, I., Durry, G., Korablev, O., Chassefière, E., Bertaux,
2605 J.-L. 2004. Tdlas, a diode laser sensor for the in situ monitoring of H₂O and
2606 CO₂ isotopes. 35th COSPAR Scientific Assembly 35, 2115.
- 2607 LeBeau, R. P., Dowling, T. E. 1998. EPIC Simulations of Time-Dependent,
2608 Three-Dimensional Vortices with Application to Neptune's Great Dark
2609 SPOT. *Icarus* 132, 239-265.
- 2610 Leconte, J., Selsis, F., Hersant, F., Guillot, T. 2017. Condensation-inhibited
2611 convection in hydrogen-rich atmospheres . Stability against double-diffusive
2612 processes and thermal profiles for Jupiter, Saturn, Uranus, and Neptune.
2613 *Astronomy and Astrophysics* 598, A98.
- 2614 Leconte, J., Chabrier, G. 2012. A new vision of giant planet interiors: Impact
2615 of double diffusive convection. *Astronomy and Astrophysics* 540, A20.
- 2616 Lellouch, E., Moreno, R., Orton, G. S., Feuchtgruber, H., Cavalié, T., Moses,
2617 J. I., Hartogh, P., Jarchow, C., Sagawa, H. 2015. New constraints on the CH₄
2618 vertical profile in Uranus and Neptune from Herschel observations. *Astronomy*
2619 *and Astrophysics* 579, A121.
- 2620 Lellouch, E., and 53 colleagues 2010. First results of Herschel-PACS observations
2621 of Neptune. *Astronomy and Astrophysics* 518, L152.
- 2622 Lellouch, E., Moreno, R., Paubert, G. 2005. A dual origin for Neptune's carbon
2623 monoxide? *Astronomy and Astrophysics* 430, L37-L40.

- 2624 Lellouch, E., Bézard, B., Fouchet, T., Feuchtgruber, H., Encrenaz, T., de
2625 Graauw, T. 2001. The deuterium abundance in Jupiter and Saturn from ISO-
2626 SWS observations. *Astronomy and Astrophysics* 370, 610-622.
- 2627 Lellouch, E., Romani, P. N., Rosenqvist, J. 1994. The vertical Distribution and
2628 Origin of HCN in Neptune's Atmosphere. *Icarus* 108, 112-136.
- 2629 Le Roy, L., and 17 colleagues 2015. Inventory of the volatiles on comet
2630 67P/Churyumov-Gerasimenko from Rosetta/ROSINA. *Astronomy and As-
2631 trophysics* 583, A1.
- 2632 Levison, H. F., Kretke, K. A., Duncan, M. J. 2015. Growing the gas-giant
2633 planets by the gradual accumulation of pebbles. *Nature* 524, 322-324.
- 2634 Levison, H. F., Morbidelli, A., Tsiganis, K., Nesvorný, D., Gomes, R. 2011.
2635 Late Orbital Instabilities in the Outer Planets Induced by Interaction with a
2636 Self-gravitating Planetesimal Disk. *The Astronomical Journal* 142, 152.
- 2637 Levison, H. F., Thommes, E., Duncan, M. J. 2010. Modeling the Formation of
2638 Giant Planet Cores. I. Evaluating Key Processes. *The Astronomical Journal*
2639 139, 1297-1314.
- 2640 Levison, H. F., Morbidelli, A., Van Laerhoven, C., Gomes, R., Tsiganis, K. 2008.
2641 Origin of the structure of the Kuiper belt during a dynamical instability in
2642 the orbits of Uranus and Neptune. *Icarus* 196, 258-273.
- 2643 Levison, H. F., Stewart, G. R. 2001. Remarks on Modeling the Formation of
2644 Uranus and Neptune. *Icarus* 153, 224-228.
- 2645 Lian, Y., Showman, A. P. 2010. Generation of equatorial jets by large-scale
2646 latent heating on the giant planets. *Icarus* 207, 373-393.
- 2647 Limaye, S. S., Sromovsky, L. A. 1991. Winds of Neptune - Voyager observations
2648 of cloud motions. *Journal of Geophysical Research* 96, 18924-18930.
- 2649 Lindal, G. F. 1992. The atmosphere of Neptune - an analysis of radio occultation
2650 data acquired with Voyager 2. *The Astronomical Journal* 103, 967-982.

- 2651 Lindal, G. F., Lyons, J. R., Sweetnam, D. N., Eshleman, V. R., Hinson, D. P.
2652 1990. The atmosphere of Neptune - Results of radio occultation measurements
2653 with the Voyager 2 spacecraft. *Geophysical Research Letters* 17, 1733-1736.
- 2654 Lindal, G. F., Lyons, J. R., Sweetnam, D. N., Eshleman, V. R., Hinson, D. P.
2655 1987. The atmosphere of Uranus - Results of radio occultation measurements
2656 with Voyager 2. *Journal of Geophysical Research* 92, 14987-15001.
- 2657 Lissauer, J. J. 2005. Formation of the Outer Planets. *Space Science Reviews*
2658 116, 11-24.
- 2659 Lodders, K., Palme, H., Gail, H.-P. 2009. Abundances of the Elements in the
2660 Solar System. *Landolt Börnstein* .
- 2661 Lodders, K., Fegley, B., Jr. 1994. The origin of carbon monoxide in Neptune's
2662 atmosphere. *Icarus* 112, 368-375.
- 2663 Loison, J. C., Dobrijevic, M., Hickson, K. M., Heays, A. N. 2017. The photo-
2664 chemical fractionation of oxygen isotopologues in Titan's atmosphere. *Icarus*
2665 291, 17-30.
- 2666 Lunine, J. I., Stevenson, D. J. 1985. Thermodynamics of clathrate hydrate at
2667 low and high pressures with application to the outer solar system. *The As-
2668 trophysical Journal Supplement Series* 58, 493-531.
- 2669 Lurton, T., Renard, J.-B., Vignelles, D., Jeannot, M., Akiki, R., Mineau, J.-L.,
2670 Tonnelier, T. 2014. Light scattering at small angles by atmospheric irregular
2671 particles: modelling and laboratory measurements. *Atmospheric Measure-
2672 ment Techniques* 7, 931-939.
- 2673 Luszcz-Cook, S. H., de Pater, I., Wright, M. 2013. Spatially-resolved millimeter-
2674 wavelength maps of Neptune. *Icarus* 226, 437-454.
- 2675 Luszcz-Cook, S. H., de Pater, I. 2013. Constraining the origins of Neptune's car-
2676 bon monoxide abundance with CARMA millimeter-wave observations. *Icarus*
2677 222, 379-400.

- 2678 Mahaffy, P. R., and 84 colleagues 2012. The Sample Analysis at Mars Investi-
2679 gation and Instrument Suite. *Space Science Reviews* 170, 401-478.
- 2680 Mahaffy, P. R., Niemann, H. B., Alpert, A., Atreya, S. K., Demick, J., Donahue,
2681 T. M., Harpold, D. N., Owen, T. C. 2000. Noble gas abundance and isotope
2682 ratios in the atmosphere of Jupiter from the Galileo Probe Mass Spectrometer.
2683 *Journal of Geophysical Research* 105, 15061-15072.
- 2684 Mahaffy, P. R., Donahue, T. M., Atreya, S. K., Owen, T. C., Niemann, H. B.
2685 1998. Galileo Probe Measurements of D/H and $3\text{He}/4\text{He}$ in Jupiter's Atmo-
2686 sphere. *Space Science Reviews* 84, 251-263.
- 2687 Makarov, A., 2000. Electrostatic axially harmonic orbital trapping: a high-
2688 performance technique of mass analysis. *Anal. Chem.* 72, 1156-1162.
- 2689 Manfroid, J., Jehin, E., Hutsemékers, D., Cochran, A., Zucconi, J.-M., Arpigny,
2690 C., Schulz, R., Stüwe, J. A., Ilyin, I. 2009. The CN isotopic ratios in comets.
2691 *Astronomy and Astrophysics* 503, 613-624.
- 2692 Marten, A., Matthews, H. E., Owen, T., Moreno, R., Hidayat, T., Biraud,
2693 Y. 2005. Improved constraints on Neptune's atmosphere from submillimetre-
2694 wavelength observations. *Astronomy and Astrophysics* 429, 1097-1105.
- 2695 Marten, A., Gautier, D., Owen, T., Sanders, D. B., Matthews, H. E., Atreya,
2696 S. K., Tilanus, R. P. J., Deane, J. R. 1993. First observations of CO and HCN
2697 on Neptune and Uranus at millimeter wavelengths and the implications for
2698 atmospheric chemistry. *The Astrophysical Journal* 406, 285-297.
- 2699 Martin, S. C., de Pater, I., Marcus, P. 2012. Neptune's zonal winds from near-IR
2700 Keck adaptive optics imaging in August 2001. *Astrophysics and Space Science*
2701 337, 65-78.
- 2702 Marty, B., and 29 colleagues 2017. Xenon isotopes in 67P/Churyumov-
2703 Gerasimenko show that comets contributed to Earth's atmosphere. *Science*
2704 356, 1069-1072.

- 2705 Marty, B., Chaussidon, M., Wiens, R. C., Jurewicz, A. J. G., Burnett, D. S.
2706 2011. A ^{15}N -Poor Isotopic Composition for the Solar System As Shown by
2707 Genesis Solar Wind Samples. *Science* 332, 1533.
- 2708 Matousek, S. 2007. The Juno New Frontiers mission. *Acta Astronautica* 61,
2709 932-939.
- 2710 Matthews, M.S., Bergstrahl, J.T., Miner, E.D. 1991. *Uranus*. University of Ari-
2711 zona Press, Tucson, ISBN: 978-0-8165-1208-9.
- 2712 Mayer, L., Quinn, T., Wadsley, J., Stadel, J. 2002. Formation of Giant Planets
2713 by Fragmentation of Protoplanetary Disks. *Science* 298, 1756-1759.
- 2714 Meadows, V. S., Orton, G., Line, M., Liang, M.-C., Yung, Y. L., Van Cleve,
2715 J., Burgdorf, M. J. 2008. First Spitzer observations of Neptune: Detection of
2716 new hydrocarbons. *Icarus* 197, 585-589.
- 2717 Milos, F. S., Chen, Y.-K., Mahzari, M. 2017. Arcjet Tests and Thermal
2718 Response Analysis for Dual-Layer Woven Carbon Phenolic. 47th AIAA
2719 Thermophysics Conference, AIAA AVIATION Forum, (AIAA 2017-3353)
2720 <https://doi.org/10.2514/6.2017-3353>.
- 2721 Mizuno, H. 1980. Formation of the Giant Planets. *Progress of Theoretical*
2722 *Physics* 64, 544-557.
- 2723 Morbidelli, A., Tsiganis, K., Crida, A., Levison, H. F., Gomes, R. 2007. Dynam-
2724 ics of the Giant Planets of the Solar System in the Gaseous Protoplanetary
2725 Disk and Their Relationship to the Current Orbital Architecture. *The Astro-*
2726 *nomical Journal* 134, 1790-1798.
- 2727 Morbidelli, A., Levison, H. F., Tsiganis, K., Gomes, R. 2005. Chaotic capture
2728 of Jupiter's Trojan asteroids in the early Solar System. *Nature* 435, 462-465.
- 2729 Moreno, R., Marten, A., Lellouch, E. 2009. Search for PH_3 in the Atmospheres of
2730 Uranus and Neptune at Millimeter Wavelength. AAS/Division for Planetary
2731 Sciences Meeting Abstracts #41 41, 28.02.

- 2732 Moses, J.I., Poppe, A.R., 2017. Dust Ablation on the Giant Planets: Conse-
2733 quences for Stratospheric Photochemistry. *Icarus*, submitted.
- 2734 Moses, J. I. 2014. Chemical kinetics on extrasolar planets. *Philosophical Trans-*
2735 *actions of the Royal Society of London Series A* 372, 20130073-20130073.
- 2736 Moses, J. I., and 10 colleagues 2011. Disequilibrium Carbon, Oxygen, and Ni-
2737 trogen Chemistry in the Atmospheres of HD 189733b and HD 209458b. *The*
2738 *Astrophysical Journal* 737, 15.
- 2739 Moses, J. I., Fouchet, T., Bézard, B., Gladstone, G. R., Lellouch, E., Feuchtgru-
2740 ber, H. 2005. Photochemistry and diffusion in Jupiter's stratosphere: Con-
2741 straints from ISO observations and comparisons with other giant planets.
2742 *Journal of Geophysical Research (Planets)* 110, E08001.
- 2743 Moses, J. I., Rages, K., Pollack, J. B. 1995. An analysis of Neptune's strato-
2744 spheric haze using high-phase-angle voyager images. *Icarus* 113, 232-266.
- 2745 Moses, J. I., Allen, M., Yung, Y. L. 1992. Hydrocarbon nucleation and aerosol
2746 formation in Neptune's atmosphere. *Icarus* 99, 318-346.
- 2747 Mousis, O., and 43 colleagues 2016. The Hera Saturn entry probe mission. *Plan-*
2748 *etary and Space Science* 130, 80-103.
- 2749 Mousis, O., Lunine, J. I., Fletcher, L. N., Mandt, K. E., Ali-Dib, M., Gautier,
2750 D., Atreya, S. 2014b. New Insights on Saturn's Formation from its Nitrogen
2751 Isotopic Composition. *The Astrophysical Journal* 796, L28.
- 2752 Mousis, O., and 50 colleagues 2014a. Scientific rationale for Saturn's in situ
2753 exploration. *Planetary and Space Science* 104, 29-47.
- 2754 Mousis, O., Lunine, J. I., Madhusudhan, N., Johnson, T. V. 2012. Nebular
2755 Water Depletion as the Cause of Jupiter's Low Oxygen Abundance. *The As-*
2756 *trophysical Journal* 751, L7.

- 2757 Mousis, O., Lunine, J. I., Picaud, S., Cordier, D. 2010. Volatile inventories in
2758 clathrate hydrates formed in the primordial nebula. *Faraday Discussions* 147,
2759 509.
- 2760 Mousis, O., Alibert, Y., Benz, W. 2006. Saturn's internal structure and carbon
2761 enrichment. *Astronomy and Astrophysics* 449, 411-415.
- 2762 Nagao, H., S. Miki, and M. Toyoda, Development of a miniaturized multi-turn
2763 time-of-flight mass spectrometer with a pulsed fast atom bombardment ion
2764 source 2014. *Europ. J. Mass spec.* 20(3), 215–220.
- 2765 Nesvorný, D. 2011. Young Solar System's Fifth Giant Planet?. *The Astrophys-*
2766 *ical Journal* 742, L22.
- 2767 Nettelmann, N., Helled, R., Fortney, J. J., Redmer, R. 2013. New indication
2768 for a dichotomy in the interior structure of Uranus and Neptune from the
2769 application of modified shape and rotation data. *Planetary and Space Science*
2770 77, 143-151.
- 2771 Niemann, H. B., Atreya, S. K., Demick, J. E., Gautier, D., Haberman, J. A.,
2772 Harpold, D. N., Kasprzak, W. T., Lunine, J. I., Owen, T. C., Raulin, F. 2010.
2773 Composition of Titan's lower atmosphere and simple surface volatiles as mea-
2774 sured by the Cassini-Huygens probe gas chromatograph mass spectrometer
2775 experiment. *Journal of Geophysical Research (Planets)* 115, E12006.
- 2776 Niemann, H. B., and 17 colleagues 2005. The abundances of constituents of
2777 Titan's atmosphere from the GCMS instrument on the Huygens probe. *Nature*
2778 438, 779-784.
- 2779 Niemann, H. B., and 18 colleagues 2002. The Gas Chromatograph Mass Spec-
2780 trometer for the Huygens probe. *Space Science Reviews* 104, 551-590.
- 2781 Niemann, H. B., and 11 colleagues 1998. The composition of the Jovian at-
2782 mosphere as determined by the Galileo probe mass spectrometer. *Journal of*
2783 *Geophysical Research* 103, 22831-22846.

- 2784 Niemann, H. B., and 12 colleagues 1996. The Galileo probe Mass Spectrometer:
2785 Composition of Jupiter's Atmosphere. *Science* 272, 846-849.
- 2786 Niemann, H. B., Harpold, D. N., Atreya, S. K., Carignan, G. R., Hunten,
2787 D. M., Owen, T. C. 1992. Galileo probe Mass Spectrometer experiment. *Space*
2788 *Science Reviews* 60, 111-142.
- 2789 Noll, K. S., Geballe, T. R., Knacke, R. F. 1995. Detection of H₂¹⁸O in Jupiter.
2790 *The Astrophysical Journal* 453, L49.
- 2791 Öberg, K. I., Bergin, E. A. 2016. Excess C/O and C/H in Outer Protoplanetary
2792 Disk Gas. *The Astrophysical Journal* 831, L19.
- 2793 Öberg, K. I., Murray-Clay, R., Bergin, E. A. 2011. The Effects of Snowlines on
2794 C/O in Planetary Atmospheres. *The Astrophysical Journal* 743, L16.
- 2795 Okumura, D., Toyoda, M., Ishihara, M., Katakuse, I. 2004. A compact sector-
2796 type multi-turn time-of-flight mass spectrometer 'MULTUM II'. *Nuclear In-*
2797 *struments and Methods in Physics Research A* 519, 331-337.
- 2798 Orton, G. S., Fletcher, L. N., Encrenaz, T., Leyrat, C., Roe, H. G., Fujiyoshi,
2799 T., Pantin, E. 2015. Thermal imaging of Uranus: Upper-tropospheric tem-
2800 peratures one season after Voyager. *Icarus* 260, 94-102.
- 2801 Orton, G. S., Fletcher, L. N., Moses, J. I., Mainzer, A. K., Hines, D., Hammel,
2802 H. B., Martin-Torres, F. J., Burgdorf, M., Merlet, C., Line, M. R. 2014a.
2803 Mid-infrared spectroscopy of Uranus from the Spitzer Infrared Spectrometer:
2804 1. Determination of the mean temperature structure of the upper troposphere
2805 and stratosphere. *Icarus* 243, 494-513.
- 2806 Orton, G. S., Moses, J. I., Fletcher, L. N., Mainzer, A. K., Hines, D., Hammel,
2807 H. B., Martin-Torres, J., Burgdorf, M., Merlet, C., Line, M. R. 2014b. Mid-
2808 infrared spectroscopy of Uranus from the Spitzer infrared spectrometer: 2.
2809 Determination of the mean composition of the upper troposphere and strato-
2810 sphere. *Icarus* 243, 471-493.

- 2811 Orton, G. S., Encrenaz, T., Leyrat, C., Puetter, R., Friedson, A. J. 2007. Ev-
2812 idence for methane escape and strong seasonal and dynamical perturbations
2813 of Neptune's atmospheric temperatures. *Astronomy and Astrophysics* 473,
2814 L5-L8.
- 2815 Orton, G. S., and 16 colleagues 1998. Characteristics of the Galileo probe entry
2816 site from Earth-based remote sensing observations. *Journal of Geophysical*
2817 *Research* 103, 22791-22814.
- 2818 Owen, T., Encrenaz, T. 2006. Compositional constraints on giant planet forma-
2819 tion. *Planetary and Space Science* 54, 1188-1196.
- 2820 Owen, T., Encrenaz, T. 2003. Element Abundances and Isotope Ratios in the
2821 Giant Planets and Titan. *Space Science Reviews* 106, 121-138.
- 2822 Owen, T., Mahaffy, P. R., Niemann, H. B., Atreya, S., Wong, M. 2001. Proto-
2823 solar Nitrogen. *The Astrophysical Journal* 553, L77-L79.
- 2824 Owen, T., Mahaffy, P., Niemann, H. B., Atreya, S., Donahue, T., Bar-Nun, A.,
2825 de Pater, I. 1999. A low-temperature origin for the planetesimals that formed
2826 Jupiter. *Nature* 402, 269-270.
- 2827 Pearl, J. C., Conrath, B. J. 1991. The albedo, effective temperature, and energy
2828 balance of Neptune, as determined from Voyager data. *Journal of Geophysical*
2829 *Research* 96, 18.
- 2830 Pearl, J. C., Conrath, B. J., Hanel, R. A., Pirraglia, J. A. 1990. The albedo,
2831 effective temperature, and energy balance of Uranus, as determined from
2832 Voyager IRIS data. *Icarus* 84, 12-28.
- 2833 Pollack, J. B., Hubickyj, O., Bodenheimer, P., Lissauer, J. J., Podolak, M.,
2834 Greenzweig, Y. 1996. Formation of the Giant Planets by Concurrent Accretion
2835 of Solids and Gas. *Icarus* 124, 62-85.
- 2836 Pollack, J. B., Podolak, M., Bodenheimer, P., Christofferson, B. 1986. Plan-
2837 etesimal dissolution in the envelopes of the forming, giant planets. *Icarus* 67,
2838 409-443.

- 2839 Poppe, A. R. 2016. An improved model for interplanetary dust fluxes in the
2840 outer Solar System. *Icarus* 264, 369-386.
- 2841 Prinn, R. G., Barshay, S. S. 1977. Carbon monoxide on Jupiter and implications
2842 for atmospheric convection. *Science* 198, 1031-1034.
- 2843 Quilligan, G., DuMonthier, J., Aslam, S., Lakew, B., Kleyner, I., Katz, R. 2015.
2844 Thermal Radiometer Signal Processing using Radiation Hard CMOS Appli-
2845 cation Specific Integrated Circuits for use in Harsh Planetary Environments.
2846 European Planetary Science Congress 2015, held 27 September - 2 October,
2847 2015 in Nantes, France.
- 2848 Quilligan, G., Aslam, S., Lakew, B., DuMonthier, J., Katz, R., and Kleyner,
2849 I. 2014. A $0.18\mu\text{m}$ CMOS Thermopile Readout ASIC Immune to 50 Mrad
2850 Total Ionizing Dose (Si) and Single Event Latchup to $174\text{ MeV}\cdot\text{cm}^2/\text{mg}$.
2851 International Workshop on Instrumentation for Planetary Missions (IPM-
2852 2014), November 2014, Greenbelt, MD 20771.
- 2853 Ragent, B., Colburn, D. S., Rages, K. A., Knight, T. C. D., Avrin, P., Orton,
2854 G. S., Yanamandra-Fisher, P. A., Grams, G. W. 1998. The clouds of Jupiter:
2855 Results of the Galileo Jupiter mission probe nephelometer experiment. *Jour-
2856 nal of Geophysical Research* 103, 22891-22910.
- 2857 Renard, J.-B., and 33 colleagues 2016b. LOAC: a small aerosol optical
2858 counter/sizer for ground-based and balloon measurements of the size distribu-
2859 tion and nature of atmospheric particles - Part 2: First results from balloon
2860 and unmanned aerial vehicle flights. *Atmospheric Measurement Techniques*
2861 9, 3673-3686.
- 2862 Renard, J.-B., and 33 colleagues 2016a. LOAC: a small aerosol optical
2863 counter/sizer for ground-based and balloon measurements of the size distribu-
2864 tion and nature of atmospheric particles - Part 1: Principle of measurements
2865 and instrument evaluation. *Atmospheric Measurement Techniques* 9, 1721-
2866 1742.

- 2867 Renard, J.-B., Thaury, C., Mineau, J.-L. and Gaubicher, B. 2010. Small-
2868 angle light scattering by airborne particulates: Environnement-S.A. con-
2869 tinuous particulate monitor, *Measurement Science Technology*, 21, 931-939,
2870 doi:10.1088/0957-0233/21/8/085901.
- 2871 Renard, J.-B., Worms, J.-C., Lemaire, T., Hadamcik, E., Huret, N. 2002. Light
2872 scattering by dust particles in microgravity: polarization and brightness imag-
2873 ing with the new version of the PROGRA2 instrument. *Applied Optics* 41,
2874 609-618.
- 2875 Romani, P. N., Bishop, J., Bezard, B., Atreya, S. 1993. Methane photochemistry
2876 on Neptune - Ethane and acetylene mixing ratios and haze production. *Icarus*
2877 106, 442.
- 2878 Romani, P. N., Atreya, S. K. 1989. Stratospheric aerosols from CH₄ photochem-
2879 istry on Neptune. *Geophysical Research Letters* 16, 941-944.
- 2880 Romani, P. N., Atreya, S. K. 1988. Methane photochemistry and methane pro-
2881 duction on Neptune. *Icarus* 74, 424-445.
- 2882 Rousselot, P., and 11 colleagues 2014. Toward a Unique Nitrogen Isotopic Ratio
2883 in Cometary Ices. *The Astrophysical Journal* 780, L17.
- 2884 Rubin, M., and 19 colleagues 2017. Evidence for depletion of heavy silicon iso-
2885 topes at comet 67P/Churyumov-Gerasimenko. *Astronomy and Astrophysics*
2886 601, A123.
- 2887 Rubin, M., and 31 colleagues 2015. Molecular nitrogen in comet
2888 67P/Churyumov-Gerasimenko indicates a low formation temperature. *Sci-*
2889 *ence* 348, 232-235.
- 2890 Sanchez-Lavega, A., 2017. Gas giants, In: *Zonal jets, occurrence, genesis, sci-*
2891 *ence*. Cambridge Univ. Press.
- 2892 Sanchez-Lavega, A.: *An Introduction to Planetary Atmospheres*, CRC press,
2893 Taylor & Francis group, 2011.

- 2894 Sánchez-Lavega, A., Pérez-Hoyos, S., Hueso, R. 2004. Clouds in planetary atmo-
2895 spheres: A useful application of the Clausius-Clapeyron equation. *American*
2896 *Journal of Physics* 72, 767-774.
- 2897 Schneider, J., Dedieu, C., Le Sidaner, P., Savalle, R., Zolotukhin, I. 2011. Defin-
2898 ing and cataloging exoplanets: the exoplanet.eu database. *Astronomy and*
2899 *Astrophysics* 532, A79.
- 2900 Scherer, S., Altwegg, K., Balsiger, H., Fischer, J., Jäckel, A., Korth, A., Mild-
2901 ner, M., Piazza, D., Reme, H., Wurz, P. 2006. A novel principle for an ion
2902 mirror design in time-of-flight mass spectrometry. *International Journal of*
2903 *Mass Spectrometry* 251, 73-81.
- 2904 Shcherbakov, V., Gayet, J.-F., Baker, B., Lawson, P. 2006. Light Scattering by
2905 Single Natural Ice Crystals. *Journal of Atmospheric Sciences* 63, 1513-1525.
- 2906 Schulz, B., Encrenaz, T., Bézard, B., Romani, P. N., Lellouch, E., Atreya,
2907 S. K. 1999. Detection of C₂H₄ in Neptune from ISO/PHT-S observations.
2908 *Astronomy and Astrophysics* 350, L13-L17.
- 2909 Seiff, A., Kirk, D. B., Knight, T. C. D., Young, R. E., Mihalov, J. D., Young,
2910 L. A., Milos, F. S., Schubert, G., Blanchard, R. C., Atkinson, D. 1998. Ther-
2911 mal structure of Jupiter's atmosphere near the edge of a 5- μ m hot spot in the
2912 north equatorial belt. *Journal of Geophysical Research* 103, 22857-22890.
- 2913 Seiff, A., Knight, T. C. D. 1992. The Galileo probe Atmosphere Structure In-
2914 strument. *Space Science Reviews* 60, 203-232.
- 2915 Seiff, A., Kirk, D. B., Young, R. E., Blanchard, R. C., Findlay, J. T., Kelly,
2916 G. M., Sommer, S. C. 1980. Measurements of thermal structure and thermal
2917 contrasts in the atmosphere of Venus and related dynamical observations -
2918 Results from the four Pioneer Venus probes. *Journal of Geophysical Research*
2919 85, 7903-7933.

- 2920 Serigano, J., Nixon, C. A., Cordiner, M. A., Irwin, P. G. J., Teanby, N. A.,
2921 Charnley, S. B., Lindberg, J. E. 2016. Isotopic Ratios of Carbon and Oxygen
2922 in Titan's CO using ALMA. *The Astrophysical Journal* 821, L8.
- 2923 Shimma, S. H. Nagao, J. Aoki, K. Takahashi, S. Miki, and M. Toyoda, Miniatur-
2924 ized High-Resolution Time-of-flight Mass Spectrometer MULTUM-S II with
2925 an Infinite flight Path, (2010), *Anal. Chem.* 82, 8456–8463.
- 2926 Simon, A. A., and 11 colleagues 2016. Neptune's Dynamic Atmosphere from
2927 Kepler K2 Observations: Implications for Brown Dwarf Light Curve Analyses.
2928 *The Astrophysical Journal* 817, 162.
- 2929 Smith, B. A., and 64 colleagues 1989. Voyager 2 at Neptune: Imaging Science
2930 Results. *Science* 246, 1422-1449.
- 2931 Smith, B. A., and 10 colleagues 1986. Voyager 2 in the Uranian system - Imaging
2932 science results. *Science* 233, 43-64.
- 2933 Smith, M. D., Gierasch, P. J. 1995. Convection in the outer planet atmospheres
2934 including ortho-para hydrogen conversion. *Icarus* 116, 159-179.
- 2935 Spilker, T. R., Atreya, S. K., Atkinson, D. H., Colaprete, A., Coustenis, A. 2012.
2936 Science investigation options with a NASA New Frontiers Program Saturn
2937 entry probe mission. *European Planetary Science Congress 2012 EPSC2012-*
2938 *300.*
- 2939 Spilker, T. R., Atkinson, D. H., Atreya, S. K., Colaprete, A., Spilker, L. J.
2940 2011. Significant Science from a Saturn Atmospheric Entry Probe Mission.
2941 *AGU Fall Meeting Abstracts .*
- 2942 Stromovsky, L. A., de Pater, I., Fry, P. M., Hammel, H. B., Marcus, P. 2015.
2943 High S/N Keck and Gemini AO imaging of Uranus during 2012-2014: New
2944 cloud patterns, increasing activity, and improved wind measurements. *Icarus*
2945 258, 192-223.

- 2946 Sromovsky, L. A., Karkoschka, E., Fry, P. M., Hammel, H. B., de Pater, I.,
2947 Rages, K. 2014. Methane depletion in both polar regions of Uranus inferred
2948 from HST/STIS and Keck/NIRC2 observations. *Icarus* 238, 137-155.
- 2949 Sromovsky, L. A., Fry, P. M., Kim, J. H. 2011. Methane on Uranus: The case
2950 for a compact CH₄ cloud layer at low latitudes and a severe CH₄ depletion
2951 at high-latitudes based on re-analysis of Voyager occultation measurements
2952 and STIS spectroscopy. *Icarus* 215, 292-312.
- 2953 Sromovsky, L. A., Fry, P. M., Hammel, H. B., Ahue, W. M., de Pater, I., Rages,
2954 K. A., Showalter, M. R., van Dam, M. A. 2009. Uranus at equinox: Cloud
2955 morphology and dynamics. *Icarus* 203, 265-286.
- 2956 Sromovsky, L. A. 2005. Accurate and approximate calculations of Raman scat-
2957 tering in the atmosphere of Neptune. *Icarus* 173, 254-283.
- 2958 Sromovsky, L. A., Fry, P. M., Dowling, T. E., Baines, K. H., Limaye, S. S.
2959 2001. Coordinated 1996 HST and IRTF Imaging of Neptune and Triton. III.
2960 Neptune's Atmospheric Circulation and Cloud Structure. *Icarus* 149, 459-488.
- 2961 Sromovsky, L. A., Collard, A. D., Fry, P. M., Orton, G. S., Lemmon, M. T.,
2962 Tomasko, M. G., Freedman, R. S. 1998. Galileo probe measurements of ther-
2963 mal and solar radiation fluxes in the Jovian atmosphere. *Journal of Geophys-*
2964 *ical Research* 103, 22929-22977.
- 2965 Sromovsky, L. A., Limaye, S. S., Fry, P. M. 1995. Clouds and circulation on
2966 Neptune: Implications of 1991 HST observations. *Icarus* 118, 25-38.
- 2967 Sromovsky, L. A., Limaye, S. S., Fry, P. M. 1993. Dynamics of Neptune's Major
2968 Cloud Features. *Icarus* 105, 110-141.
- 2969 Sromovsky, L. A., Best, F. A., Revercomb, H. E., Hayden, J. 1992. Galileo Net
2970 Flux Radiometer Experiment. *Space Science Reviews* 60, 233-262.
- 2971 Stauffer, J., and 11 colleagues 2016. Spitzer Space Telescope Mid-IR Light
2972 Curves of Neptune. *The Astronomical Journal* 152, 142.

- 2973 Stevenson, D. J., Lunine, J. I. 1988. Rapid formation of Jupiter by diffuse
2974 redistribution of water vapor in the solar nebula. *Icarus* 75, 146-155.
- 2975 Stoker, C. R., Toon, O. B. 1989. Moist convection on Neptune. *Geophysical*
2976 *Research Letters* 16, 929-932.
- 2977 Stone, E. C., Miner, E. D. 1989. The Voyager 2 encounter with the Neptunian
2978 system. *Science* 246, 1417-1421.
- 2979 Stratman, P. W., Showman, A. P., Dowling, T. E., Sromovsky, L. A. 2001.
2980 EPIC Simulations of Bright Companions to Neptune's Great Dark Spots.
2981 *Icarus* 151, 275-285.
- 2982 Summers, M. E., Strobel, D. F. 1989. Photochemistry of the atmosphere of
2983 Uranus. *The Astrophysical Journal* 346, 495-508.
- 2984 Suomi, V. E., Limaye, S. S., Johnson, D. R. 1991. High winds of Neptune - A
2985 possible mechanism. *Science* 251, 929-932.
- 2986 Taylor, F. W., Atreya, S. K., Encrenaz, T., Hunten, D. M., Irwin, P. G. J.,
2987 Owen, T. C. 2004. The composition of the atmosphere of Jupiter. *Jupiter. The*
2988 *Planet, Satellites and Magnetosphere* 1, 59-78.
- 2989 Tice, D. S., Irwin, P. G. J., Fletcher, L. N., Teanby, N. A., Hurley, J., Orton,
2990 G. S., Davis, G. R. 2013. Uranus' cloud particle properties and latitudinal
2991 methane variation from IRTF SpeX observations. *Icarus* 223, 684-698.
- 2992 Toyoda, M., Okumura, D., Ishihara, M., Katakuse, I., 2003. Multi-turn time-
2993 of-flight mass spectrometers with electrostatic sectors. *J. Mass Spectrom.* 38,
2994 1125-1142.
- 2995 Trilling, D. E., Benz, W., Guillot, T., Lunine, J. I., Hubbard, W. B., Burrows, A.
2996 1998. Orbital Evolution and Migration of Giant Planets: Modeling Extrasolar
2997 Planets. *The Astrophysical Journal* 500, 428-439.

- 2998 Tsiganis, K., Gomes, R., Morbidelli, A., Levison, H. F. 2005. Origin of the
2999 orbital architecture of the giant planets of the Solar System. *Nature* 435,
3000 459-461.
- 3001 Turrini, D., and 14 colleagues 2014. The comparative exploration of the ice
3002 giant planets with twin spacecraft: Unveiling the history of our Solar System.
3003 *Planetary and Space Science* 104, 93-107.
- 3004 Twarowski, A. 1995. Reduction of a phosphorus oxide and acid reaction set
3005 1995. *Combustion and Flame* 102, 41-54.
- 3006 Tyler, G. L., Eshleman, V. R., Hinson, D. P., Marouf, E. A., Simpson, R. A.,
3007 Sweetnam, D. N., Anderson, J. D., Campbell, J. K., Levy, G. S., Lindal, G. F.
3008 1986. Voyager 2 radio science observations of the Uranian system Atmosphere,
3009 rings, and satellites. *Science* 233, 79-84.
- 3010 Uckert, K., Chanover, N. J., Olkin, C. B., Young, L. A., Hammel, H. B., Miller,
3011 C., Bauer, J. M. 2014. An investigation of the temperature variations in
3012 Neptune's upper stratosphere including a July 2008 stellar occultation event.
3013 *Icarus* 232, 22-33.
- 3014 Venkatapathy, E., Ellerby, D., Prabhu, D., Martinez, E. 2012. Saturn Atmo-
3015 spheric Structure Investigation: An Assessment of and Challenges and Rec-
3016 ommendations for Extending the Galileo Approach to Future Probe Mis-
3017 sions. *International Workshop on Instrumentation for Planetary Missions*
3018 1683, 1129.
- 3019 Venot, O., Hébrard, E., Agúndez, M., Dobrijevic, M., Selsis, F., Hersant, F.,
3020 Iro, N., Bounaceur, R. 2012. A chemical model for the atmosphere of hot
3021 Jupiters. *Astronomy and Astrophysics* 546, A43.
- 3022 Verhaege, C., Shcherbakov, V., Personne, P. 2009. Retrieval of complex refrac-
3023 tive index and size distribution of spherical particles from Dual-Polarization
3024 Polar Nephelometer data. *Journal of Quantitative Spectroscopy and Radia-
3025 tive Transfer* 110, 1690-1697.

- 3026 Visscher, C., Sperier, A. D., Moses, J. I., Keane, T. C. 2009. Phosphine and Am-
3027 monia Photochemistry in Jupiter's Troposphere. Lunar and Planetary Science
3028 Conference 40, 1201.
- 3029 Visscher, C., Fegley, B., Jr. 2005. Chemical Constraints on the Water and Total
3030 Oxygen Abundances in the Deep Atmosphere of Saturn. The Astrophysical
3031 Journal 623, 1221-1227.
- 3032 Volten, H., Muñoz, O., Hovenier, J. W., Waters, L. B. F. M. 2006. An up-
3033 date of the Amsterdam Light Scattering Database. Journal of Quantitative
3034 Spectroscopy and Radiative Transfer 100, 437-443.
- 3035 von Zahn, U., Hunten, D. M., Lehmacher, G. 1998. Helium in Jupiter's at-
3036 mosphere: Results from the Galileo probe helium interferometer experiment.
3037 Journal of Geophysical Research 103, 22815-22830.
- 3038 von Zahn, U., Hunten, D. M. 1992. The Jupiter Helium Interferometer experi-
3039 ment on the Galileo entry probe. Space Science Reviews 60, 263-281.
- 3040 Waite Jr., H., et al., 2014. A neutral gas investigation of origins (ANGIO),
3041 NASA AO NNH12ZDA006O-JUICE, Jupiter Icy Moons Explorer Instrument,
3042 submitted for publication.
- 3043 Wang, D., Lunine, J. I., Mousis, O. 2016. Modeling the disequilibrium species
3044 for Jupiter and Saturn: Implications for Juno and Saturn entry probe. Icarus
3045 276, 21-38.
- 3046 Wang, D., Gierasch, P. J., Lunine, J. I., Mousis, O. 2015. New insights on
3047 Jupiter's deep water abundance from disequilibrium species. Icarus 250, 154-
3048 164.
- 3049 Webster, C. R., and 452 colleagues 2013. Low Upper Limit to Methane Abun-
3050 dance on Mars. Science 342, 355-357.
- 3051 Webster, C. R., Mahaffy, P. R. 2011. Determining the local abundance of Mar-
3052 tian methane and its $^{13}\text{C}/^{12}\text{C}$ and D/H isotopic ratios for comparison with

- 3053 related gas and soil analysis on the 2011 Mars Science Laboratory (MSL)
3054 mission. *Planetary and Space Science* 59, 271-283.
- 3055 Weiland, J. L., and 21 colleagues 2011. Seven-year Wilkinson Microwave
3056 Anisotropy Probe (WMAP) Observations: Planets and Celestial Calibration
3057 Sources. *The Astrophysical Journal Supplement Series* 192, 19.
- 3058 West, R. A., Baines, K. H., Pollack, J. B. 1990. Clouds and aerosols in the
3059 Uranian Atmosphere, Chapter in *Uranus (Planet)*, p. 204, Bergstralh J. T.,
3060 Miner, E. D., and Mathews, M. D., editors University of Arizona Press.
- 3061 Wong, M. H., Mahaffy, P. R., Atreya, S. K., Niemann, H. B., Owen, T. C. 2004.
3062 Updated Galileo probe mass spectrometer measurements of carbon, oxygen,
3063 nitrogen, and sulfur on Jupiter. *Icarus* 171, 153-170.
- 3064 Wright, I. P., and 19 colleagues 2007. Ptolemy an Instrument to Measure Sta-
3065 ble Isotopic Ratios of Key Volatiles on a Cometary Nucleus. *Space Science*
3066 *Reviews* 128, 363-381.
- 3067 Yelle, R. V., McConnell, J. C., Strobel, D. F. 1989. The far ultraviolet reflection
3068 spectrum of Uranus - Results from the Voyager encounter. *Icarus* 77, 439-456.
- 3069 Young, L. A., Bosh, A. S., Buie, M., Elliot, J. L., Wasserman, L. H. 2001.
3070 Uranus after Solstice: Results from the 1998 November 6 Occultation. *Icarus*
3071 153, 236-247.
- 3072 Young, R. E. 1998. The Galileo probe mission to Jupiter: Science overview.
3073 *Journal of Geophysical Research* 103, 22775-22790.
- 3074 Young, L. A., Yelle, R. V., Young, R., Seiff, A., Kirk, D. B. 1997. Gravity waves
3075 in Jupiter's thermosphere. *Science* 276, 108-111.
- 3076 Zarka, P., Pedersen, B. M. 1986. Radio detection of Uranian lightning by Voy-
3077 ager 2. *Nature* 323, 605-608.

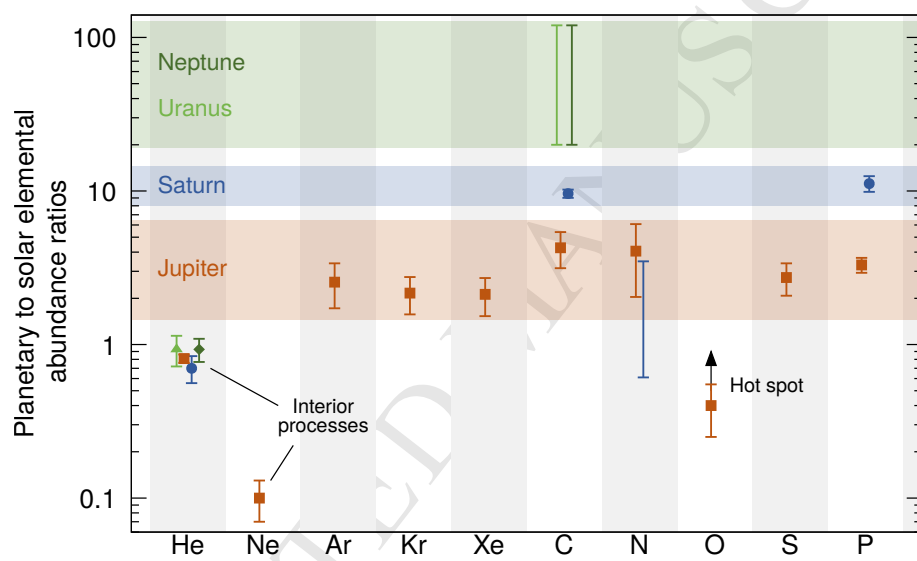


Figure 1: Enrichment factors (with respect to the solar value) of noble gases and heavy elements in the giant planets. See text for references.

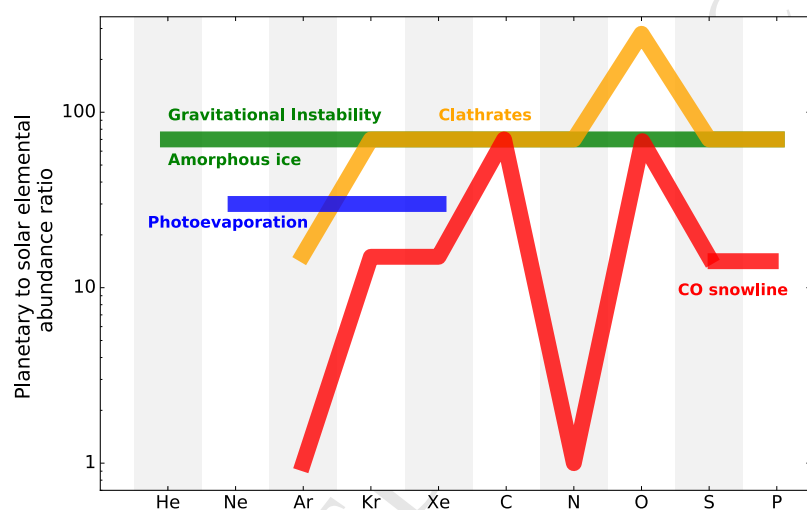


Figure 2: Qualitative differences between the enrichments in volatiles predicted in Uranus and Neptune predicted by the different formation scenarios (calibrations based on the carbon determination). The resulting enrichments for the different volatiles are shown in green (disk instability model and amorphous ice), orange (clathrates), blue (photoevaporation) and red (CO snowline). In their photoevaporation model, [Guillot and Hueso \(2006\)](#) predict that heavy elements other than noble gases follow the amorphous ice or clathrate predictions.

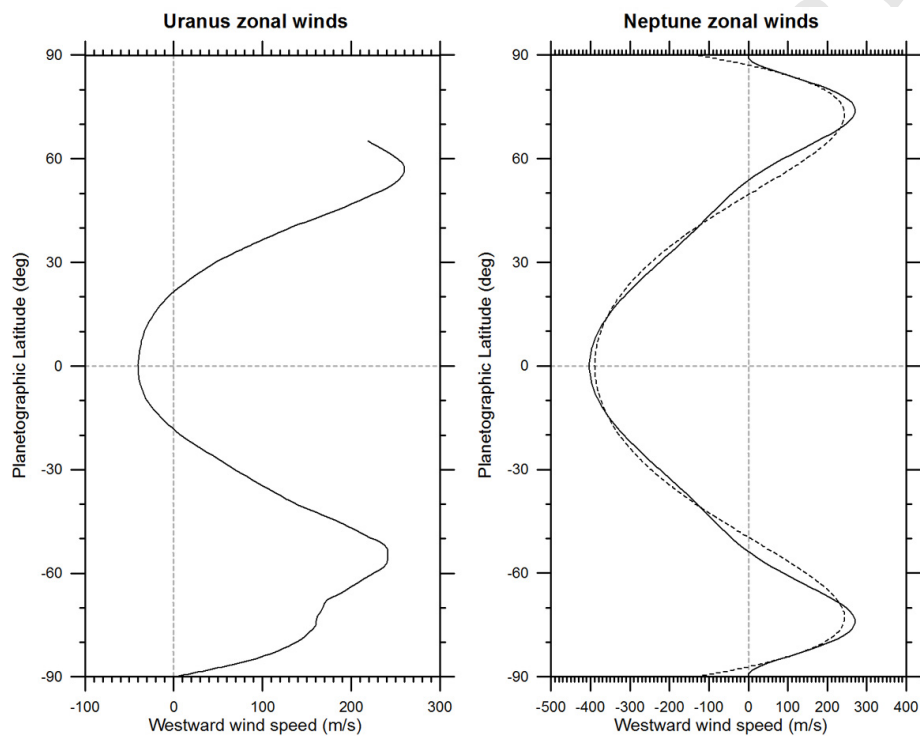


Figure 3: Uranus and Neptune zonal winds. Uranus winds (left panel) combining Keck results from 2012-2014 and a reanalysis of 1986 Voyager images by [Karkoschka \(2015\)](#) and adopted from [Sromovsky et al. \(2015\)](#). Neptune wind (right panel) from Voyager measurements showing different fits to Voyager wind speeds ([Sromovsky et al., 1993](#)) and given in [Sánchez-Lavega \(2017\)](#).

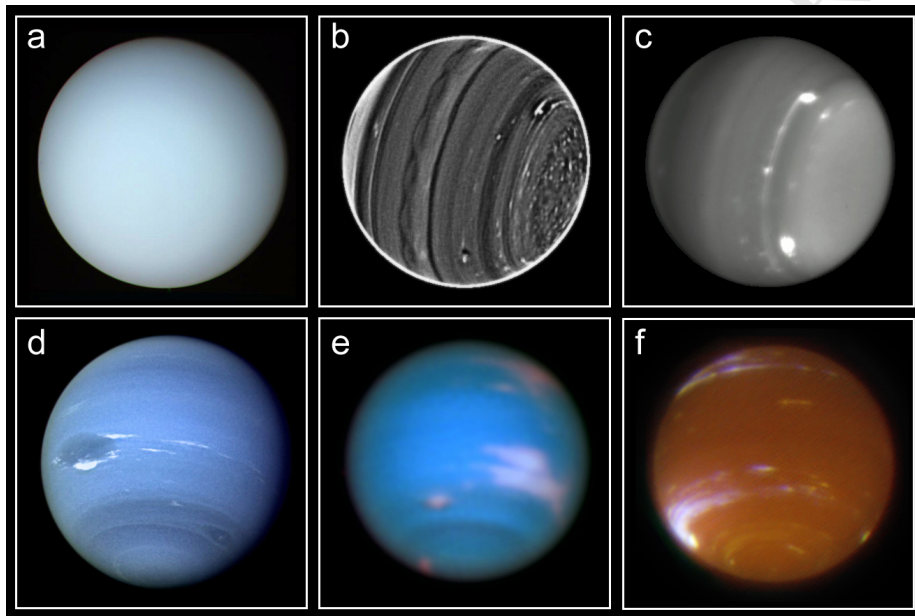


Figure 4: Global views of Uranus and Neptune. Upper row Uranus images in: (a) visible wavelengths from Voyager 2; (b) Near IR with extreme processing of cloud features from [Fry et al. \(2012\)](#); (c) Near IR of bright features from [de Pater et al. \(2014\)](#). Bottom row Neptune images in: (d) visible wavelengths from Voyager 2; (e) Visible wavelengths from HST (image credits: NASA, ESA, and M.H. Wong and J. Tollefson from UC Berkeley); (f) near IR (observations courtesy of I. de Pater).

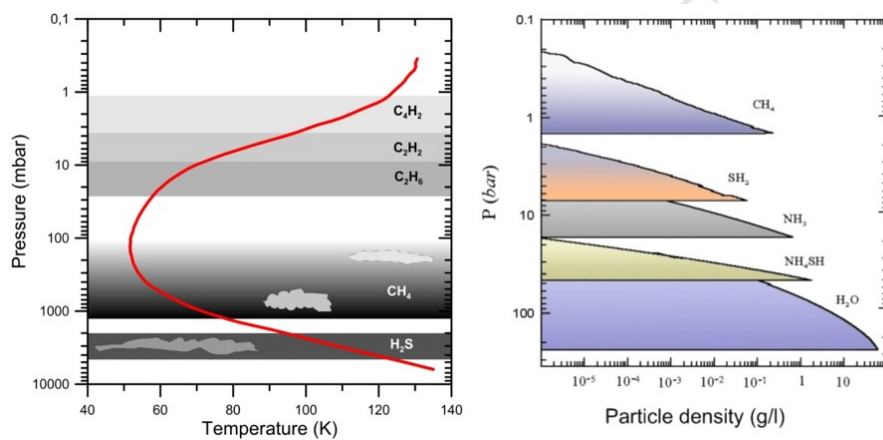


Figure 5: Neptune clouds and hazes. Left: Scheme of the hazes and upper cloud structure accessible to remote sensing, based on those published by [Baines and Hammel \(1994\)](#), [Baines et al. \(1995\)](#), [Irwin \(2009\)](#), [Irwin et al. \(2017\)](#), with temperatures from [Lindal \(1992\)](#). Right: Thermochemical model of the main cloud layers in Neptune for the compounds abundances given in the text (following [Atreya and Wong, 2005](#)). A similar scheme is valid for Uranus.

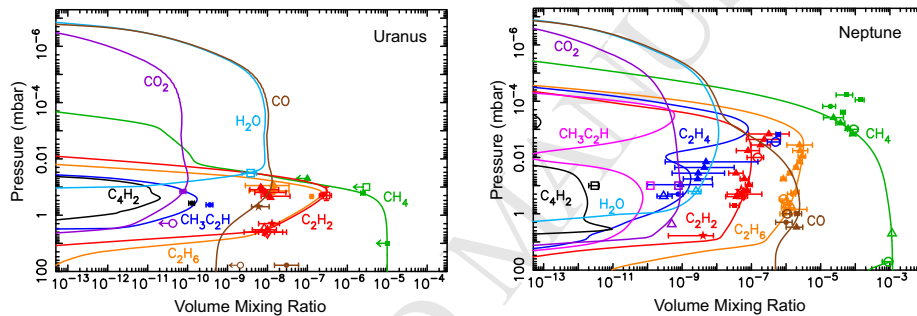


Figure 6: Comparison of the vertical distributions of hydrocarbons and oxygen compounds in the stratospheres of Uranus (left) and Neptune (right), following [Moses and Poppe \(2017\)](#). Points with error bars are measurements from a wide variety of literature sources – see [Moses and Poppe \(2017\)](#) for full details. The difference in homopause altitudes, driven by the different efficiencies of vertical mixing, cause significant differences in the stratospheric chemistry.

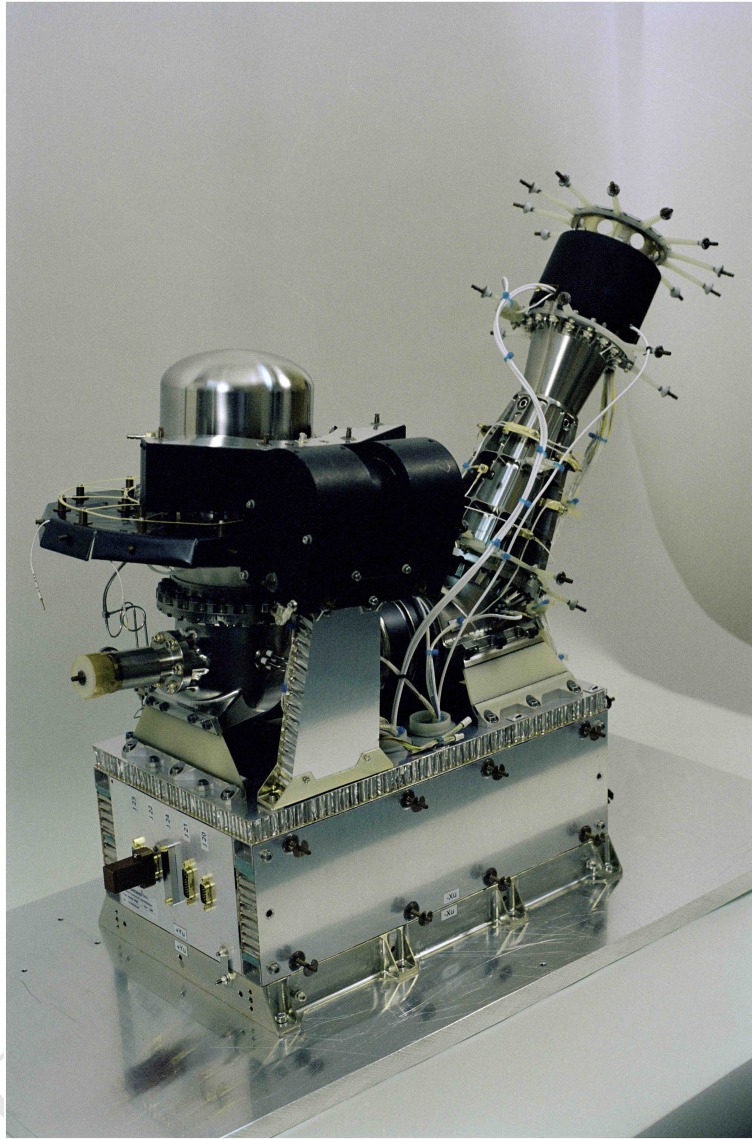


Figure 7: Flight model of DFMS/ROSINA instrument without thermal hardware.

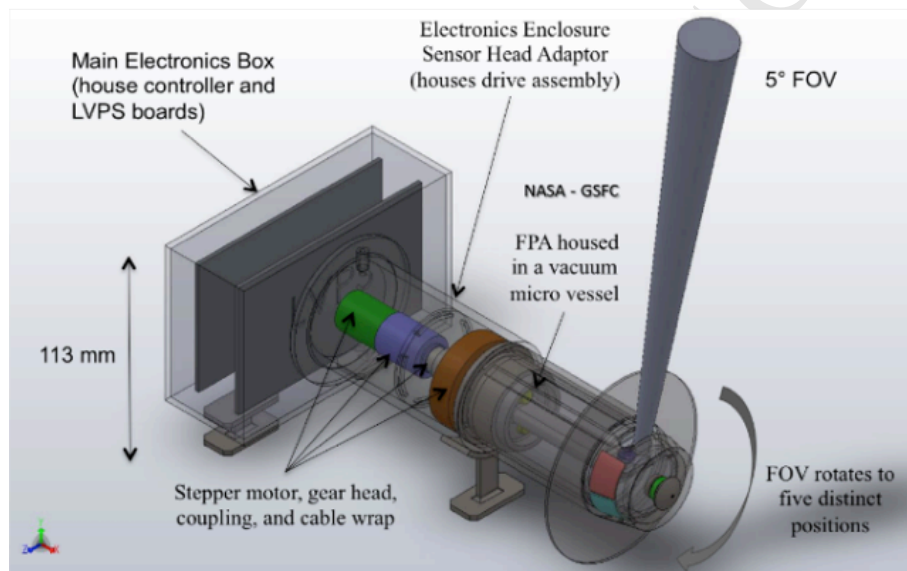


Figure 8: NASA/GSFC NFR instrument concept showing a 5° field-of-view that can be rotated by a stepper motor into five distinct look angles.



Figure 9: Saturn probe prototype NFR vacuum micro-vessel with sapphire and diamond windows; this houses a focal plane assembly that accommodates Winston cones with a 5° field-of-view acceptance angle.

Table 1: Elemental abundances in Jupiter, Saturn, Uranus and Neptune, as derived from upper tropospheric composition

Elements	Jupiter	Saturn	Uranus	Neptune
He/H ⁽¹⁾	$(7.85 \pm 0.16) \times 10^{-2}$	$(6.75 \pm 1.25) \times 10^{-2}$	$(8.88 \pm 2.00) \times 10^{-2}$	$(8.96 \pm 1.46) \times 10^{-2}$
Ne/H ⁽²⁾	$(1.240 \pm 0.014) \times 10^{-5}$	–	–	–
Ar/H ⁽³⁾	$(9.10 \pm 1.80) \times 10^{-6}$	–	–	–
Kr/H ⁽⁴⁾	$(4.65 \pm 0.85) \times 10^{-9}$	–	–	–
Xe/H ⁽⁵⁾	$(4.45 \pm 0.85) \times 10^{-10}$	–	–	–
C/H ⁽⁶⁾	$(1.19 \pm 0.29) \times 10^{-3}$	$(2.65 \pm 0.10) \times 10^{-3}$	$(0.6 - 3.2) \times 10^{-2}$	$(0.6 - 3.2) \times 10^{-2}$
N/H ⁽⁷⁾	$(3.32 \pm 1.27) \times 10^{-4}$	$(0.50 - 2.85) \times 10^{-4}$	–	–
O/H ⁽⁸⁾	$(2.45 \pm 0.80) \times 10^{-4}$	–	–	–
S/H ⁽⁹⁾	$(4.45 \pm 1.05) \times 10^{-5}$	–	–	–
P/H ⁽¹⁰⁾	$(1.08 \pm 0.06) \times 10^{-6}$	$(3.64 \pm 0.24) \times 10^{-6}$	–	–

⁽¹⁾ von Zahn et al. (1998) and Niemann et al. (1998) for Jupiter, Conrath and Gautier (2000) and Atreya et al. (2016) for Saturn, Conrath et al. (1987) for Uranus and Burgdorf et al. (2003) for Neptune. We only consider the higher value of the uncertainty on He in the case of Neptune. ^(2–5) Mahaffy et al. (2000) for Jupiter. ⁽⁶⁾ Wong et al. (2004) for Jupiter, Fletcher et al. (2009a) for Saturn, Lindal et al. (1987), Baines et al. (1995), Karkoschka and Tomasko (2009), and Sromovsky et al. (2014) for Uranus, Lindal et al. (1990), Baines et al. (1995), and Karkoschka (2011) for Neptune. ⁽⁷⁾ Wong et al. (2004) for Jupiter, Fletcher et al. (2011) for Saturn (our N/H range is derived from the observed range of 90–500 ppm of NH₃). ⁽⁸⁾ Wong et al. (2004) for Jupiter (probably a lower limit, not representative of the bulk O/H). de Graauw et al. (1997) has detected H₂O at 5 μm with ISO in Saturn, but the measurement at 1–3 bars is not representative of the bulk O/H. ⁽⁹⁾ Wong et al. (2004) for Jupiter. ⁽¹⁰⁾ Fletcher et al. (2009b) for Jupiter and Saturn.

Table 2: Ratios to protosolar values in the upper tropospheres of Jupiter, Saturn, Uranus and Neptune

Elements	Jupiter/Protosolar ⁽¹⁾	Saturn/Protosolar ⁽¹⁾	Uranus/Protosolar ⁽¹⁾	Neptune/Protosolar ⁽¹⁾
He/H	0.81 ± 0.05	0.70 ± 0.14	0.93 ± 0.21	0.93 ± 0.16
Ne/H	0.10 ± 0.03	–	–	–
Ar/H	2.55 ± 0.83	–	–	–
Kr/H	2.16 ± 0.59	–	–	–
Xe/H	2.12 ± 0.59	–	–	–
C/H	4.27 ± 1.13	9.61 ± 0.59	~20 – 120	~20 – 120
N/H	4.06 ± 2.02	0.61 – 3.48	–	–
O/H	0.40 ± 0.15 (hotspot)	–	–	–
S/H	2.73 ± 0.65	–	–	–
P/H	3.30 ± 0.37	11.17 ± 1.31	–	–

Error is defined as $(\Delta E/E)^2 = (\Delta X/X_{\text{planet}})^2 + (\Delta X/X_{\text{Protosun}})^2$. ⁽¹⁾ [Lodders et al. \(2009\)](#).

Caveat: These ratios only refer to the levels where abundance measurements have been performed, i.e. in the upper tropospheres. Thus, they are not automatically representative of deep interior enrichments. This is especially true if the deep interior contain a significant fraction of another element (e.g. oxygen in Uranus and Neptune, according to models). Moreover, the Helium value was computed for pure H₂/He mixtures (i.e. the upper tropospheric CH₄ has not been accounted for), because CH₄ is condensed at 1 bar where He is measured.

Table 3: Isotopic ratios measured in Jupiter, Saturn, Uranus and Neptune

Isotopic ratio	Jupiter	Saturn	Uranus	Neptune
D/H (in H ₂) ⁽¹⁾	$(2.60 \pm 0.7) \times 10^{-5}$	$1.70^{+0.75}_{-0.45} \times 10^{-5}$	$(4.4 \pm 0.4) \times 10^{-5}$	$(4.1 \pm 0.4) \times 10^{-5}$
³ He/ ⁴ He ⁽²⁾	$(1.66 \pm 0.05) \times 10^{-4}$	–	–	–
¹² C/ ¹³ C (in CH ₄) ⁽³⁾	$92.6^{+4.5}_{-4.1}$	$91.8^{+8.4}_{-7.8}$	–	–
¹⁴ N/ ¹⁵ N (in NH ₃) ⁽⁴⁾	434.8^{+65}_{-50}	> 357	–	–
²⁰ Ne/ ²² Ne ⁽⁵⁾	13 ± 2	–	–	–
³⁶ Ar/ ³⁸ Ar ⁽⁶⁾	5.6 ± 0.25	–	–	–
¹³⁶ Xe/total Xe ⁽⁷⁾	0.076 ± 0.009	–	–	–
¹³⁴ Xe/total Xe ⁽⁸⁾	0.091 ± 0.007	–	–	–
¹³² Xe/total Xe ⁽⁹⁾	0.290 ± 0.020	–	–	–
¹³¹ Xe/total Xe ⁽¹⁰⁾	0.203 ± 0.018	–	–	–
¹³⁰ Xe/total Xe ⁽¹¹⁾	0.038 ± 0.005	–	–	–
¹²⁹ Xe/total Xe ⁽¹²⁾	0.285 ± 0.021	–	–	–
¹²⁸ Xe/total Xe ⁽¹³⁾	0.018 ± 0.002	–	–	–

⁽¹⁾ Mahaffy et al. (1998) for Jupiter, Lellouch et al. (2001) for Saturn, Feuchtgruber et al. (2013) for Uranus and Neptune. ⁽²⁾ Mahaffy et al. (1998) for Jupiter. ⁽³⁾ Niemann et al. (1998) for Jupiter, Fletcher et al. (2009a) for Saturn. ⁽⁴⁾ Wong et al. (2004) for Jupiter, Fletcher et al. (2014b) for Saturn. ^(5–13) Mahaffy et al. (2000) for Jupiter.

Table 4: Measurement requirements

Instrument	Measurement
Mass spectrometer	Elemental and chemical composition Isotopic composition High molecular mass organics
Helium Abundance Detector	Helium abundance
Atmospheric Structure Instrument	Pressure, temperature, density, molecular weight profile
Doppler Wind Experiment	Measure winds, speed and direction
Nephelometer	Cloud structure Solid/liquid particles
Net-flux radiometer	Thermal/solar energy

Table 5: Seven baseline NFR spectral filter channels and objectives, for maximizing science return from both Uranus and Neptune’s atmospheres.

Ch#	Wavelength (μm)	Objectives
1	2.5–300	Deposition/loss of thermal radiation
2	50–100	Ammonia humidity at > 1 bar
3	14–35	Water vapor
4	8.5–8.8	cloud opacity; implanted sulphur species (SO_2 , H_2S , etc.)
5	3.5–5.8	Water vapor and cloud structure
6	0.6–3.5	Solar deposition of methane absorption; cloud particles
7	0.2–3.5	Total deposition of solar radiation and hot spot detection